Communauté
UNIVERSITÉ Grenoble Alpes

PUCPR

THÈSE

Pour obtenir le grade de

DOCTEUR DE LA COMMUNAUTE UNIVERSITE GRENOBLE ALPES

préparée dans le cadre d'une cotutelle *entre la Communauté Université Grenoble Alpes* et *Pontificia Universidade Católica do Paraná*

Spécialité : **Génie Civil et Sciences de l'Habitat (UDG) et Génie Mécanique (PUCPR)**

Arrêté ministériel : le 6 janvier 2005 - 7 août 2006

Présentée par

Lorena FREITAS DUTRA

Thèse dirigée par **Anne-Cécile GRILLET, Monika WOLOSZYN et Nathan MENDES**

préparée au sein des **Laboratoires LOCIE UMR CNRS 5271 et LST**

dans **les Écoles Doctorales SISEO et Escola Politécnica**

Development of an innovative material of high hygrothermal performance

Développement d'un matériau innovant de haute performance hygroscopique

Thèse soutenue le **30 novembre**, devant le jury composé de :

M. Celso PERES FERNANDES
Maître de Conférences, Universidade Federal de Santa Catarina, examinateur
M. José Antônio BELLINI DA CUNHA NETO
Professeur, Universidade Federal de Santa Catarina, Rapporteur
M. Joseph VIRGONE
Professeur, Université Claude-Bernard Lyon 1, Examinateur
M. Paulo César PHILIPPI
Professeur, Pontificia Universidade Católica do Paraná, Examinateur
M. Rafik BELARBI
Professeur, Université de La Rochelle, Rapporteur
Mme Anne-Cécile GRILLET
Maître de Conférences, Université Savoie Mont Blanc, Directrice de thèse
Mme Monika WOLOSZYN
Professeure, Université Savoie Mont Blanc, Directrice de thèse
M. Nathan MENDES
Professeur, Pontificia Universidade Católica do Paraná, Directeur de thèse

SIGILLUM UNIVERSITATIS GRATIANOPOLITANAE 1339

"Pensate al futuro che vi aspetta,
pensate a quello che potete fare,
e non temete niente."

"Think of the future that awaits you,
think about what you can do
and do not fear anything."

(Rita Levi Montalcini)

Abstract

Freitas Dutra, Lorena **Development of an innovative material of high hygrothermal performance**. 194 p. Ph.D. Thesis – Polytechnic School, Pontifical Catholic University of Parana and Engineering School, University of Grenoble, 2017.

Highly moisture buffering materials can be a powerful alternative to counteract moisture excess problems, to reduce the dependency of air conditioning systems and to sustainably regulate relative humidity in the built environment. Therefore, the objective of this work is to improve materials capacity to adsorb/desorb moisture by changing their porous structure. Initially, the influence of sintering temperature on the porous structure of the materials was tested as well as the effect of different compositions on this porous structure. To achieve this goal, porous materials were selected and mixed in different ratios. Then the various mix were submitted to sintering cycles under different temperatures. Finally, a physical, hygrothermal, morphological and chemical characterization of these assembled materials was done to verify their buffering performance. Results showed that the improved clay-based materials can successfully attenuate relative humidity amplitudes, thus improving hygrothermal comfort and energy savings on the control of relative humidity.

Keywords: Moisture buffering capacity. Hygrothermal characterization. Hygrothermal performance. Microstructural characterization. Absorbent materials.

Résumé

Freitas Dutra, Lorena **Développement d'un matériau innovant de haute performance hygrothermique**. 194 p. Doctorat – École polytechnique, Université Pontificale Catholique du Paraná et École d'ingénieurs, Université de Grenoble, 2017.

Les matériaux hautement absorbants peuvent être un moyen puissant de contrôler l'humidité dans les environnements intérieurs. Par conséquent, l'objectif de ce travail est d'améliorer la capacité d'adsorber / désorber l'humidité en modifiant la structure poreuse de ces matériaux. Initialement, l'influence de la température de frittage sur la structure poreuse des matériaux a été testée ainsi que l'effet de différentes compositions sur cette structure poreuse. Pour atteindre cet objectif, de matériaux poreux ont été sélectionnés et mélangés selon des rapports différents. Ensuite, les différents mélanges ont été soumis à un cycle de frittage à différentes températures. Enfin, une caractérisation physique, morphologique et chimique de plusieurs mélanges a été réalisée afin de vérifier leur performance hygrothermique. Les résultats ont montré que les matériaux améliorés à base d'argile peuvent atténuer avec succès les amplitudes d'humidité relative, améliorant ainsi le confort hygrothermique et les économies d'énergie sur le contrôle de l'humidité relative..

Mots-clés: Capacité tampon d'humidité. Caractérisation hygrothermique. Performance hygrothermique. Caractérisation microstructurelle. Matériaux absorbants.

List of Figures

Figure 1.1 (a) Evolution of the regulatory requirements for energy consumption of new buildings in France. The dotted green line represents the predictable evolution without the adoption of the Grenelle Environment and the straight green line indicates the dynamics of reduction driven by the Grenelle Environment program. Consumption is in $kWh_{EP}/(m^2.year)$ [ADEME 2011]; (b) Brazilian energy efficiency label of a residential building [CBIE 2014]. 9

Figure 1.2 (a) Mould growth (b) Cracking caused by moisture excess on bricks. From Ransom [2002]. 10

Figure 1.3 Moisture buffer effect of materials on indoor relative humidity: (a) wood based material [Simonson *et al.* 2002] (b) hemp and rape-straw concretes [Rahim *et al.* 2016]. 12

Figure 1.4 Vapour release in kitchen: (a) neglecting sorption capacity of furnitures; (b) with sorption. From Plathner and Woloszyn [2002]. 12

Figure 1.5 Versatility of clay-based materials in buildings [Wienerberger 2017]. . . 14

Figure 1.6 Porous roof mechanism illustrated by (a) Vardoulakis *et al.* [2011b] (b) Wanphen and Nagano [2009]. 15

Figure 1.7 Representation of a porous medium. 16

Figure 1.8 Water sorption isotherm regions for a porous material. 18

Figure 1.9 (a) Sorption isotherms and (b) hysteresis classification according IUPAC [Thommes *et al.* 2015]. 20

Figure 1.10 Water vapor permeability evolution with relative humidity. Adapted from Tveit [1966]. 22

Figure 1.11 Thermal conductivity evolution with moisture content (vol-%) and temperature for aerated concrete with a density of 540 kg/m^3. Adapted from Hagemann [1981]. 25
Figure 1.12 $MBV_{practical}$ classes according NORDTEST [Rode 2005] 28
Figure 1.13 Impact of sintering temperature on the porosity of clay-based ceramic [Nigay *et al.* 2017]. 36

Figure 2.1 General flow chart of clay brick/tile production. 41
Figure 2.2 Sintering process [*Breviary Technical Ceramics*]. 43
Figure 2.3 Petrological forms of perlite [Samar and Saxena 2016]. 45
Figure 2.4 Scanning electron microscopy image of expanded perlite [Wu *et al.* 2014]. 45
Figure 2.5 The crystal structure of montmorillonite projected on *ab* and *ac* axes, showing the position of the water entrance. 47
Figure 2.6 Scanning electron microscopy image of expanded vermiculite [Rashad 2016]. 48
Figure 2.7 (a) Transmission electron microscopy image of fibrous palygorskite (b) Schematic structure of palygorskite [Galan 1996]. 49
Figure 2.8 The crystalline structure of kaolinite. 51
Figure 2.9 The hydroxyl structure and the dehydration of diatomaceous silica (a) H-bounded silanols, (b) isolated silanols and (c) siloxane [Yuan *et al.* 2004]. 52
Figure 2.10 SEM images showing the diatomite structures: (a) at 900°C for 3 hours with clean opened pores, (b) at 900°C for 5 hours, smoother surface and collapsing of porous structure; (c) at 1000°C for 5 hours, the complete destroying of diatomite porous structure [Ibrahim and Selim 2012]. . . 53
Figure 2.11 Crystalline structure of zeolite [Lenntech 2017]. 53
Figure 2.12 Preparation of the mix of raw materials and clay. 54
Figure 2.13 Preparation of samples using silicon mold 54
Figure 2.14 Samples in the furnace. 55
Figure 2.15 (a) Sintering cycle. 55
Figure 2.16 Firing linear shrinkage in function of the percentage of additives in clay and firing temperature. Addition of: (a) vermiculite (b) perlite. 58

Figure 2.17 Firing linear shrinkage in function of the additives (20%) and firing temperature. 59

Figure 2.18 Loss on ignition in function of the percentage of additives in clay and firing temperature. Addition of: (a) vermiculite (b) perlite. 60

Figure 2.19 Loss on ignition in function of the additives (20%) in clay and firing temperature. 61

Figure 2.20 Open porosity in function of the percentage of additives in clay and firing temperature. Addition of: (a) vermiculite (b) perlite. 62

Figure 2.21 Open porosity in function of the additives (20%) in clay and firing temperature. 62

Figure 2.22 Water absorption in function of the percentage of additives in clay and firing temperature. Addition of: (a) vermiculite (b) perlite. 63

Figure 2.23 Water absorption in function of the additives (20%) in clay and firing temperature. 64

Figure 2.24 Bulk density in function of the percentage of additives in clay and firing temperature. Addition of: (a) vermiculite (b) perlite. 65

Figure 2.25 Bulk density in function of the additives (20%) in clay and firing temperature. 65

Figure 2.26 Bending strength in function of the percentage of additives in clay and firing temperature. Addition of: (a) vermiculite (b) perlite. 66

Figure 3.1 X-ray pattern to show the phase evolution of clay when firing temperature is increased. 76

Figure 3.2 X-ray pattern when attapulgite is added to clay showing the phase evolution with the increasing of firing temperature. 77

Figure 3.3 X-ray pattern when perlite is added to clay showing the phase evolution with the increasing of firing temperature. 78

Figure 3.4 Photomicrographs of the clay samples without addition of absorbents showing the main characteristics of the clayey base material fired at 800°C: (a) larger fragments of quartz crystals (Qtz) and feldspar (Kfs) supported by a clay matrix with small crystals of quartz and feldspar. (b) detail of a larger iron hydroxide crystal (FeOH) and (c) polarized light showing the occurrence of small muscovite crystals near the clay matrix. Samples fired at 1000°C:(d) darker clay matrix with fragments of rock (RxF) and quartz agglomerates (natural light). (e) aggregate of feldspar crystals supported by the clay matrix (crossed nicols) and (f) detail of the rock fragments occurring in the clay matrix. 80

Figure 3.5 Photomicrographs of clay samples containing attapulgite particles fired at 800°C: (a) general characteristic of the sample showing the different behavior of the attapulgite particles with the heating, generation of a secondary porosity around some particles and the presence of fractures in the particles of attapulgite and particles with darker central portion indicating initiation of a fusion process (natural light). (b) same photomicrography as (a) with crossed nicols showing that the darker portions become extinct indicating the fusion, and in the matrix, the high birefringence of muscovite evidences its presence and (c) detail of the restrict corona-shape porosity formation in attapulgite particles. Samples fired at 1000°C: (d) higher ratio and width of the coronas in the attapulgite (e) attapulgite particle fractured and fragmented by secondary porosity and (f) detail of the thicker coronas and that the firing process generated the fracture and fragmentation of some attapulgite particles and formation of channels to a lesser extent. 82

Figure 3.6 Photomicrographs with natural light, showing the main microstructures of the sample containing perlite fired at 800°C: (a) perlite particles with preserved internal structure and formation of secondary porosity in the form of channels. (b) small channels connecting the perlite particles and (c) channels observed in the cross section. Samples fired at 1000°C: (d) formation of channels in greater proportion and size, (e) detail of the interaction of channels with rock fragment and (f) iron oxide/hydroxide crystal with secondary porosity in the form of corona and channels. . . 84

Figure 3.7 Particules size distribution by Quantikov. (a) Clay fired at 800°C, (b) clay fired at 1000°C, (c) clay with attapulgite fired at 800°C, (d) clay with attapulgite fired at 1000°C, (e) clay with perlite fired at 800°C, (f) clay with perlite fired at 1000°C. 87

Figure 3.8 Examples of structures identification by the software Quantikov. (a) Clay fired at 800°C, (b) clay fired at 1000°C, (c) clay with attapulgite fired at 800°C, (d) clay with attapulgite fired at 1000°C, (e) clay with perlite fired at 800°C, (f) clay with perlite fired at 1000°C, (g) secondary porosity in clay with attapulgite fired at 800°C, (h) secondary porosity in clay with attapulgite fired at 1000°C, (i) channels at clay with perlite fired at 800°C and (j) channels at clay with perlite fired at 1000°C. . . 88

Figure 3.9 SEM images showing clay morphology at two different firing temperatures and magnifications (a) 800°C and 1500x; (b) 1000°C and 1500x; (c) 800°C and 4500x and (d) 1000°C and 4500x. 93

Figure 3.10 SEM images showing raw perlite grain morphology at different magnifications (a) 50x and (b) 1000x. 94

Figure 3.11 SEM images showing morphology of the composition with perlite addition at a magnification of 1000x for the two firing temperatures: (a) 800°C and (b) 1000°C. 94

Figure 3.12 SEM images showing raw attapulgite grain morphology at different magnifications (a) 200x and (b) 10000x. 95

Figure 3.13 SEM images showing morphology of the composition with attapulgite addition at different sintering temperatures at a magnification of 10000x (a) 800°C and (b) 1000°C. 95

Figure 3.14 Pore size distribution from nitrogen adsorption test: (a) samples sintered at 800°C and (b) samples sintered at 1000°C. 97

Figure 3.15 Pore size distribution from mercury intrusion test: (a) samples sintered at 800°C and (b) samples sintered at 1000°C. 98

Figure 3.16 Mean bending strength values for samples sintered at 800°C and at 1000°C. The error bars depict the standard deviation. 100

Figure 4.1 Photo of the climate chamber (RHBOX) at LOCIE: 1 - entrances of the RHBOX; 2 - gloves used to manipulate samples inside the chamber; 3- heat exchanger used to regulate internal temperature; 4 - ventilators that help to homogenize internal relative humidity; 5 - precision scales; 6 - channel that connects the two chambers; 7 - sample being wheighed inside the chamber; 8 - thermostatted bath. 107
Figure 4.2 Schematic drawing of the method used to measure sorption isotherms . 109
Figure 4.3 Cup method with silica gel (blue) 111
Figure 4.4 Experimental setup to measure water absorption coefficient. 112
Figure 4.5 Measured water vapor adsorption and desorption curves for samples sintered at 800°C and at 1000°C and their approximations using GAB model: (a) clay with montmorillonite; (b) clay with attapulgite; (c) clay with diatomite; (d) clay with sepiolite gravel; (e) clay with sepiolite sand; (f) clay with vermiculite; (g) clay with perlite; (h) fired clay; (i) clay with sepiolite ultra-fine; (j) clay with zeolite. 116
Figure 4.6 Dry cup water vapor permeability for samples sintered at 800°C and at 1000°C exposed to the relative humidity of: (a) 33% (b) 75% 118
Figure 4.7 Absorption parameters for samples sintered at 800°C and 1000°C: (a) Water absorption coefficient (A_c) (b) Initial rate of absorption (IR) (c) Amount of water absorbed (AW). 120
Figure 4.8 Kinetic of water absorption for: (a) samples sintered at 800°C and (b) samples sintered at 1000°C. 121
Figure 4.9 Water absorption/desorption cycling for three selected composition sintered at 800°C. 121
Figure 4.10 Thermal conductivity at 33% and 75% of relative humidity for: (a) samples sintered at 800°C and (b) samples sintered at 1000°C. 122
Figure 4.11 Thermal effusivity at 33% and 75% of relative humidity for: (a) samples sintered at 800°C and (b) samples sintered at 1000°C. 123

Figure 5.1 BESTEST building dimensions. 131
Figure 5.2 Schematic view of moisture perturbations. 131
Figure 5.3 Mass variations during MBV test for: (a) samples sintered at 800°C and (b) samples sintered at 1000°C. 132

Figure 5.4 Moisture buffer value calculated for samples sintered at 800°C and at 1000°C. 134
Figure 5.5 Relative humidity variation in the room when there is no hygric inertia (MBV=0) with vapor generation and ventilation (first case). Dots represent the analytical solution and straight line corresponds to SPARK simplified model results. 135
Figure 5.6 Influence of the adsorption/desorption effect on the internal relative humidity. 136
Figure 5.7 Indoor RH amplitude reduction for materials with different MBV. . . . 137

Figure A.1 EDS pattern for raw attapulgite. 174
Figure A.2 EDS pattern for raw perlite 174
Figure A.3 EDS pattern for CATT800 175
Figure A.4 EDS pattern for CATT1000 175
Figure A.5 EDS pattern for CPER800 175
Figure A.6 EDS pattern for CPER1000 176
Figure A.7 EDS map of elements for CATT sintered at 800°C. 176
Figure A.8 EDS map of elements for CATT sintered at 1000°C. 177
Figure A.9 EDS map of elements for CPER sintered at 800°C. 178
Figure A.10 EDS map of elements for CPER sintered at 1000°C. 179

Figure B.1 Nitrogen sorption isotherms for samples sintered at 800°C:(a) fired clay (b) clay with attapulgite and (c) clay with perlite. For samples sintered at 1000°C: (d) fired clay, (e) clay with attapulgite and (f) clay with perlite. 183
Figure B.2 Linear regression aiming to obtain the parameters S and B. This linear correlation is only valid in the range of $0.05 < p/p_o < 0.35$. Samples sintered at 800°C are: (a) fired clay (b) clay with attapulgite and (c) clay with perlite. Samples sintered at 1000°C: (d) fired clay, (e) clay with attapulgite and (f) clay with perlite. 184

Figure D.1 Statistical correlations for all samples: sintered at 800°C and 1000°C. . 189

Figure E.1 Coefficients adjustment using the Van Genuchten model. 193
Figure E.2 Coefficients adjustment using the Reznik model. 194

List of Tables

Table 1.1 Moisture buffer materials in literature. 29

Table 1.1 Moisture buffer materials in literature. 30

Table 1.1 Moisture buffer materials in literature. 31

Table 1.1 Moisture buffer materials in literature. 32

Table 2.1 Characteristics of raw materials. 44

Table 3.1 Quantification of the CLAY microstructural parameters. 89

Table 3.2 Quantification of the CATT microstructural parameters. 89

Table 3.2 Quantification of the CATT microstructural parameters. 90

Table 3.3 Quantification of the CPER microstructural parameters. 90

Table 3.4 Quantification of the CATT (corona) microstructural parameters. 91

Table 3.5 N_2 adsorption measurements for CATT, CPER and CLAY samples at different firing temperatures. 97

Table 4.1 Different compositions sintered both at 800°C and at 1000°C. 106

Table 4.2 Humidity levels generated by saturated salt solutions of sorption curves at 30°C. 108

Table 5.1 Heat, air, moisture models. Adapted from Woloszyn and Rode [2008]. . 129

Table 5.2 Simulation input data of BESTEST case. 131

Table A.1 EDS operation system characteristics. 173

Table B.1 Parameters obtained by linear regression for all composition. 182

Table C.1 Parameters obtained by GAB adjustment. 185
Table C.1 Parameters obtained by GAB adjustment. 186

Table D.1 Water absorption coefficients ($A_c[Kg/m^2s^{0.5}]$), initial rate of absorption (IR $[Kg/m^2.2min]$), the total amount of water absorbed (AW $[Kg/m^2]$), specific surface area (S_o $[m^2/g]$), open porosity (OP [%]) and pore mean diameter (PM [nm]) for samples sintered at T = 800°C and at 1000°C. . 188

Table E.1 Calculated coefficients using GAB, Van Genuchten and Reznik models for samples sintered at 800°C. 192

List of Symbols and Abbreviations

Abbreviations

BJH Barett, Joyner, and Halenda

BET Brunauer, Emmett, and Teller

CAC Cation Exchange Capacity

DFT Density Functional Theory

EDX Energy-Dispersive X-ray Spectroscopy

Kfs Feldspar

RxF Fragments of rock

GAB Guggenheim, Anderson, De Boer

HVAC Heating, Ventilation and Air-Conditioning

IEA International Energy Agency

IUPAC International Union of Pure and Applied Chemistry

LOCIE Laboratory for Optimization of Design and Environmental Engineering

MIP Mercury Intrusion Porosimetry

MS Mesoporous Silica

MTPS Modified Transient Plane Source

MBC Moisture Buffer Capacity

MBV Moisture Buffer Value

OM Optical Microscopy

PECW Passive Evaporative Cooling Wall

PSD Pore Size Distribution

Qtz Quartz crystals

SEM Scanning Electron Microscopy

SPARK Simulation Problem Analysis and Research Kernel

XRD X-ray Diffraction

Greek symbols

ρ Bulk density

α GAB constant

β GAB constant

γ GAB constant

η Porosity

φ Relative humidity

Φ Temperature

μ Vapour resistance

Δ Variation

θ Volumetric moisture content

δ_a Water diffusion in the air

δ_v Water vapour permeability

Roman symbols

A	Area
N	Avogadro's constant
C_s	Cross section of the adsorbing species
S	Degree of saturation
g	Density of water vapor flow rate
p	Equilibrium pressure
L	Length of the sample
LI	Loss of ignition
w	Mass per volume moisture content
u	Massic moisture content
m	Mass
V_m	Molar volume of the gas
M	Monolayer adsorbed gas quantity
OP	Open porosity
p_o	Saturation pressure
S_o	Specific surface area
d	Thickness of the specimen
t	Time
SH	Total shrinkage
V	Total volume
p_v	Vapour pressure in each side of the sample
V_{ads}	Volume of adsorbed nitrogen by the solid material surface
A_c	Water absorption coefficient

WA	Water absorption
G	Water vapor flow rate

Subscripts

d	After drying at $105°\mathrm{C}$
a	After firing
b	Before firing
0	Beginning of the weighing
dry	Dry
f	End of the weighing
l	Liquid
sat	Saturated
sus	Suspended
s	Voids
w	Water

Acknowledgments

The last four years has been quite a journey and I would like to express my sincere gratitude to many people who have shared this incredible adventure with me.

I'm highly indebted to my advisor, Prof. Nathan Mendes who was the mentor of this expedition and gave me independence in my research allowing me to explore new scientific fields. I really appreciated our countless technical, professional, and personal discussions. Thank you, Nathan, for believing in my potential from the first time we met!

I'm beholden to my French advisor Prof. Anne-Cécile Grillet, who has always been extremely supportive and guided me throughout the work. Her knowledge, experience and patience were crucial during experiments. I also deeply appreciated our scientific and personal exchanges.

I would like to thank my advisor Prof. Monika Woloszyn who gently welcomed at LOCIE, cheered and helped me to get here. I truly appreciated her contributions to the thesis and her enormous expertise.

I am honored to have Professors José Antônio Bellini Cunha Neto and Rafik Belarbi as «rapporteurs». I extend my gratitude to the other members of thesis committee: Professors Paulo Cesar Philippi, Celso Peres Fernandes and Joseph Virgone.

My sincere thanks also go to my fellow labmates in LST and LOCIE for the stimulating discussions, for the sleepless nights we were working together before deadlines, and for all the fun we have had in the last four years. Ana, Walter, Santiago, Marcos, Ayres, Clau, Su, Julien, Adrien, Dionatas, Lucas: muitíssimo obrigada! Nico, Ioannis, Ranime, Bastien, Nolween, Patricia, Jose, Teo, Thomas, Cedric, Jonathan, Guilian, Ankita: un grand merci! A very special thanks go to Mao who was the best lab partner I could ever had; to Thierry who made a huge effort to provide the best conditions for the work; Martine and Isabelle for their

support with administrative tasks; Janinha and Cícero for the invaluable help and affection.

I extend my acknowledgments to people from other laboratories which provided the support and equipment I have needed to produce and complete my thesis: Leticia Torres Guerra and Silvia Lopez from Ecomateriales Laboratory from UANL for nitrogen adsorption data; Laurent Clerc from École des Mines d'Alès for providing mercury intrusion test results; Fluid Inclusions and Metallogenesis Laboratory at CDTN for optical microscopy and X-ray diffraction equipments specially João Batista Barbosa for XRD identification; Lucio Pinto from CDTN for providing and adapting Quantikov software allowing the quantification of our materials microstructure; Luciane Sopchenski Santos, Carlos Laurindo and Paulo Soares from Materials Technology and Manufacturing Processes Laboratory at PUCPR for performing scanning electronic microscopy and X-ray spectroscopy; Mourad Rahim from Université Picardie for rich discussions about SPARK software.

I am also indebted to my homeland Brazil for always providing me grants during my academic path. Particular thanks to CNPq and CAPES for their financial support through scholarship in these four years.

During congresses and PhD schools, I had the privilege to meet people who built the foundation for the knowledge I have acquired today. Special thanks to Professors Carsten Rode, Lars Wadsö and Abdelkrim Trabelsi for the fruitful discussions.

My heartfelt thanks to my friends for all love and support: to my childhood friends Maried, Karen and Romão; to Charles, Renata and Érica; to my rommies Rê, Ben and Pierre; to Marx, Steph, Lamita and Mohammad; to the second mother that Curitiba has given me: Lu.

All my gratitude to France for always being so generous to me. I am veritably thankful for all the unforgettable moments I have lived in this country.

I also owe a lot of recognition to my Mexican family: Amín, Lupita, Bayil, Rober, tía Martha, abuelita Adelfa, mamaíta y toda la familia! Thank you for all affection and specially for giving me such a patient, loving and caring companion. Gracias por tanto, bonito !

Finally, any amount of acknowledgment would be insufficient for my family. My parents Goretti and Aloizio that stood by me unconditionally showing me that distances can separate bodies but not souls. My brother Alan, my grandmas Zélia and Terezinha, my uncles Tote, Dinho and Caco, aunt Wal and Ken, cousins Léo, Bela, Lê, Samuca and João you are all my force and inspiration. Uncle Paulo, grandpas Aloisio and Antonio, wherever you are I know you have helped me to get here.

Tia Mônica, I owe you this thesis, without you nothing would have been possible.

Contents

Abstract . . . . . **v**

Résumé . . . . . **vii**

List of Figures . . . . . **xv**

List of Tables . . . . . **xvii**

List of Symbols and Abbreviations . . . . . **xx**

Acknowledgments . . . . . **xxi**

Introduction **1**

1 Background **5**

1.1 Moisture in buildings 7

1.1.1 Energy context 7

1.1.2 Moisture problems 9

1.1.3 Moisture buffering materials 10

1.1.4 Fired clay in buildings 13

1.2 Theoretical aspects of hygroscopic materials 15

1.2.1 Porous media 15

1.2.2 Sorption isotherms 17

1.2.3 Water vapor permeability 20

1.2.4 Liquid uptake coefficient 22

1.2.5 Thermal conductivity 23
1.3 Literature review 25
1.3.1 Moisture buffer capacity 25
1.3.2 Improving fired clay hygroscopic capacity 33
1.4 Conclusion 36

2 Materials processing and physical characterization 39
2.1 Introduction 41
2.2 Elaboration of fired clay-based materials 41
2.3 Materials 43
2.4 Preparation steps 54
2.5 Physical characterization 55
2.6 Mechanical properties 57
2.7 Results 57
2.7.1 Physical properties 57
2.7.2 Mechanical properties 65
2.8 Conclusions 66

3 Microstructural characterization of fired clay-based ceramic composites . 69
3.1 Introduction 71
3.2 Sample characterization techniques 72
3.2.1 Pore size distribution 72
3.2.2 Optical microscopy 73
3.2.3 Scanning electron microscopy (SEM) 73
3.2.4 X-ray diffraction (XRD) 73
3.3 Results and discussion 74
3.3.1 Phase identification and high temperature behavior 74
3.3.2 Microstructure morphology 78
3.3.3 Microstructural evaluation 85
3.3.4 Morphology of pores 91
3.3.5 Pore quantification 96
3.3.6 Mechanical properties 99
3.4 Conclusions 100

4 Hygrothermal properties and characterization of fired clay-based ceramic composites . . . 103

4.1 Introduction . . . 105

4.2 Materials . . . 105

4.3 Sample characterization techniques . . . 106

4.3.1 Climate chamber (RHBOX) . . . 106

4.3.2 Sorption isotherm . . . 107

4.3.3 Water vapor permeability . . . 109

4.3.4 Water absorption coefficient . . . 111

4.3.5 Thermal conductivity . . . 112

4.4 Results and Discussion . . . 113

4.4.1 Sorption isotherms . . . 113

4.4.2 Water vapor permeability . . . 116

4.4.3 Water absorption coefficient . . . 118

4.4.4 Thermal conductivity . . . 121

4.5 Conclusions . . . 123

5 Influence of the hygric performance of the innovative material on the indoor comfort . . . 125

5.1 Experimental measurements of Moisture buffer value (MBV) . . . 127

5.2 Numerical simulation . . . 128

5.2.1 Lumped capacity model . . . 129

5.2.2 Case study . . . 130

5.3 Results . . . 132

5.3.1 Moisture buffer value (MBV) . . . 132

5.3.2 Numerical simulation . . . 134

5.4 Conclusions . . . 137

Conclusions and recommendations . . . 139

Synthèse . . . 143

Bibliography . . . 149

Appendices 171

Appendix A EDS map of elements 173

Appendix B Nitrogen adsorption data and BET calculations 181

Appendix C Water adsorption isotherm data and GAB calculations 185

Appendix D Water absorption coefficient correlations 187

Appendix E Modelling water sorption curves 191

Introduction

It is known that the excess of moisture affects significantly the performance of buildings causing many problems, such as low durability of materials, mold growth, discomfort, allergies and respiratory diseases. To counteract these effects and stabilize the level of humidity in the environment, heating, ventilation and air-conditioning systems (HVAC) are often used.

According to the Brazilian Energy Bulletin[1], 46% of electricity consumption in Brazil is attributed to residential, commercial and public buildings. Considering commercial buildings, 30% of the energy consumed is mainly due to HVAC systems which has a direct impact on the cost operation of a building and an indirect impact on the environment, thus revealing the urgent need for rapid improvement of energy-efficient products and the importance of projects associated to energy subject in a Brazilian context. In France, the building sector consumes the most energy from all economic sectors: equivalent of 70 million tons of oil and the annual average consumption of this sector is close to 400 kWh of primary energy per m^2 heated [ADEME 2017]. Therefore, with a view to reduce the energy consumption, an important program "bâtiment à faible impact environnemental", was implemented by the French government on the renovation of about 25 million dwellings and the improvement of the performance of 3 million additional dwellings by 2020 [DURABLE 2010].

In response to these concerns, a research on the development of materials for improvement of hygrothermal and energy performance of buildings is carried out. This new material would take advantage of porous material natural ability to adsorb/desorb moisture to attenuate the variation of relative humidity in buildings thus reducing the use of air conditioning systems. Indeed, some research works have shown that indoor humidity can be controlled by the house itself with little or no air conditioning with the assistance of humidity controlling materials.

[1] `https://ben.epe.gov.br`

The results showed that it might be possible to reduce energy consumption indoor for heating and cooling by up to 5% and 30%, respectively, when applying hygroscopic materials with well-controlled HVAC systems [Rao *et al.* 2012].

Therefore, the improvement of hygroscopicity of building materials can be very relevant to avoid moisture problems and ensure indoor air quality, energy performance, and the durability of the building envelope.

Clay-based materials are among the oldest materials in the world and remain very popular. They are versatile and can be used in different parts of a building such as walls, façades, roof, terraces and open spaces. Also, they are durable, have good insulation properties, are natural and low-cost. However, fired clays do not hold high hygroscopicity.

For that reason, this work focuses on the improvement of hygrothermal performance of clay-based materials by the addition of highly hygroscopic compounds. The moisture buffer capacity has been examined by several researchers and particularly by the NORDEST group. Rode [2005] succeeded to standardize and to quantify the moisture buffer ability of materials naming it moisture buffer value (MBV). Further references can be found in Chapter 1.

Research objectives

The importance of reducing air conditioning consumption and improving internal comfort are the two motivation factors behind this research. Although several studies have been published about evaporative cooling, porous building materials and hygrothermal behavior, just a few of them try to combine different materials to obtain a high performance humidity controlling material and there is a very little number of works which take into account materials microstructure (specially materials composition) and its effect on phenomenological properties. Therefore, the research main objective that will be addressed in this thesis is:

Increase the hygroscopicity of clay in order to attenuate the variation of relative humidity in indoor environments such as museums and libraries.

Characterize hygrothermal and microstructural properties of the improved clay in order to quantify the uptaking/releasing moisture capacity of the material and make a link between materials microstructure and their capacity of adsorbing/desorbing moisture.

Organization of this thesis

This thesis is organized in five chapters. Initially, there is an introduction with the main research problem and the motivation of the work. Chapter 1 is a background containing information that will be used in the experimental part of the work. The next chapter is centered around methodologies for producing porous materials and measurements of their properties. Chapter 3 is about the microstructural characterization of produced materials and Chapter 4 characterizes them hygroscopically. The last chapter evidences the moisture buffer effect on the attenuation of indoor relative humidity. Finally, a conclusion summarizes the observations and shows perspectives for future work. The details of each individual chapters are as follows:

Chapter 1 contains a reminder of the energy and environmental context of the construction sector, provides a bibliographical overview of the studies and projects carried out moisture buffer materials and their hygrothermal behavior at the material and building scale. It focuses mainly on fired clay-based materials selected here as a reference material and how to improve their hygroscopicity.

Chapter 2 presents the details of the sample production methodologies as well as the results of the physical characterization of the porous samples used for this thesis.

Chapter 3 illustrates and provides an enlightenment about microstructural matrix and components on selected samples. Characterization methods are described such as: optical and scanning electron microscopies, x-ray diffraction, mercury intrusion porosimetry and nitrogen adsorption. The microstructural morphology is illustrated with micrographies and quantified with the help of a software. Finally, a discussion about the influence of firing temperature and the incorporation of attapulgite and perlite on clay is provided.

Chapter 4 gives details of the hygrothermal characterization performed on the produced samples along with the results of this characterization. Additionally, an analysis of the influence of sintering temperature and the addition of the absorbents on the clay-based material is presented.

Chapter 5 shows results of simulation of the hygrothermal properties of the designed materials in room scale. The influence of the hygroscopic inertia of developed materials is emphasized on the attenuation of relative humidity level of a room.

List of Publications

Peer-reviewed journals

I. L.F. Dutra, N. Mendes, and P.C. Philippi. On the characterization of pore size distribution of building materials. Accepted for *Journal of Building Physics*, 2017.

II. L.F. Dutra, M.E. Freitas, A.C. Grillet, N. Mendes, and M. Woloszyn. Detailed microstructural characterization of clay-based ceramic composite with high higrothermal performance. Submitted to *Construction and Building Materials*, 2017.

Peer-reviewed conference proceedings

III. L.F. Dutra, A.C. Grillet, N. Mendes, and M. Woloszyn. On the improvement of hygroscopic capacity of clay-based materials. *International RILEM Conference on Materials, Systems and Structures in Civil Engineering*, Lyngby, Denmark, p.p 319-328, August 22-24, 2016.

IV. N. Mendes, and L.F. Dutra. Intrinsic permeability assessment from porous size distribution function. *Proceedings of the 1st International Symposium on Building Pathology*, Porto, Portugal, p.p 529-536, March 24-27, 2015.

V. N. Mendes, and L.F. Dutra. On the evaluation of pore size distribution function from sorption isotherms. *15th Brazilian Congress of Thermal Sciences and Engineering*, Belem, Brazil, November 10-13, 2014.

Chapter 1

Background

After presenting the context of the work, this chapter proposes a bibliographical synthesis of the studies carried out on moisture buffer materials and their importance to the energy and environmental context in the construction sector. It focuses particularly on fired clay, which is a very traditional and versatile building material. However, its hygrothermal properties have not already been detailed in literature thus they are introduced is this chapter. This information will be used in the following chapters to produce and characterize new fired-clay compositions.

Contents

1.1 Moisture in buildings **7**
1.1.1 Energy context 7
1.1.2 Moisture problems 9
1.1.3 Moisture buffering materials 10
1.1.4 Fired clay in buildings 13
1.2 Theoretical aspects of hygroscopic materials **15**
1.2.1 Porous media 15
1.2.2 Sorption isotherms 17
1.2.3 Water vapor permeability 20
1.2.4 Liquid uptake coefficient 22
1.2.5 Thermal conductivity 23
1.3 Literature review **25**
1.3.1 Moisture buffer capacity 25
1.3.2 Improving fired clay hygroscopic capacity 33
1.4 Conclusion **36**

1.1 Moisture in buildings

1.1.1 Energy context

Energy efficiency in buildings is a matter of global concern, accounting for about 40% of global annual energy consumption. According to the International Energy Agency[1], energy efficiency is the fastest and cheapest way to avoid the environmental catastrophe that may be caused by increased global energy consumption, especially among developing countries.

From the point of view of energy consumption in a building, there are three aspects to consider:

I. Energy consumed when building the edifice, embedded in the production and transportation of building materials, as well as in its manipulation at the construction site;

II. Energy consumed by the activities developed in the building, by the use of the indispensable equipments to the activities exercised by the users;

III. Energy consumed to provide users with the necessary comfort conditions.

Although all cited aspects are relevant, this work focuses on the third point.

In France, considering all economic sectors, building is the largest consumer of energy (42.5% of total final energy) and generates 23% of greenhouse gas. This impacts the environment and the purchasing power of households, especially on the most modest of them. These expenditures tend to increase with rising energy prices. Therefore, in order to reduce energy consumption and costs on a sustainable basis, the Grenelle Environment proposed thermal regulation programs that evolved with time (Fig. 1.1a). The thermal regulations currently in force (RT2012) made it possible to divide by three the energy consumption of new buildings compared to the previous regulations. These energy exigences are in terms of primary energy requirements, not to be confused with the final energy: the final energy (kWh_{EF}) is the amount of energy available to the end user; primary energy (kWh_{EP}) is the consumption required for production of this final energy. The next regulation is even more ambitious and introduces the concept of positive energy building, also called "BEPOS"[2]. They are generally passive buildings that produce more energy (heat, electricity) than they consume being efficient and strongly equipped with means of energy production in relation to their

[1] `www.iea.org`
[2] Bâtiment à énergie positive

energy needs. Walls, roofs and even windows can be put to use in the accumulation and return of heat or in the production of electricity [ADEME 2011].

Brazil is the 10th largest energy consumer in the world, and its consumption is expected to double by 2030, according to a World Bank study that mentions that the country could save about $ 2.5 billion a year if it uses its full potential for energy efficiency. The Brazilian electricity crisis in 2001 had as its immediate response the enactment of the law on energy efficiency and greater investment (more than R$ 1 billion) in the existing national program for the conservation of electric energy named PROCEL[3]. As a result, there was a significant cumulative energy savings between in the building sector of 30%, especially in the residential sector; this percentage rises to 50% in new buildings with a total economy of 107 billion kWh [PROCEL 2017]. Additionally, in order to regulate and optimize thermal performance in buildings, two main standards were proposed: NBR15220 [2005] and NBR15575 [2013]. Also, INMETRO [2012] classified residential buildings by their level of energy-efficiency rating from A (most efficient) to E (least efficient) (Fig. 1.1b). This label can be applied to new and existing buildings but is optional for residential buildings. The existing labeling for energy efficiency of residential buildings in Brazil, does not take into account moisture in the simulations performed for the envelope evaluation method, neither has a moisture related item of assessment. Considering the already high usage of air conditioning in some cities, representing around 30% of the mean electricity consumption of a house in Northern regions [Eletrobras 2007], moisture may play a role on energy efficiency assessment once it affects the heat transfer of the building envelope.

Moreover, moisture can also be responsible for mold growth, decreasing materials durability and causing health problems. That is why moisture-buffering effect of hygroscopic structures may have a significant effect on the relative humidity level and variations of the indoor air, which may improve the perceived comfort and quality of the air [Salonvaara *et al.* 2004].

[3]Programa Nacional de Conservação de Energia Elétrica `http://www.procelinfo.com.br`

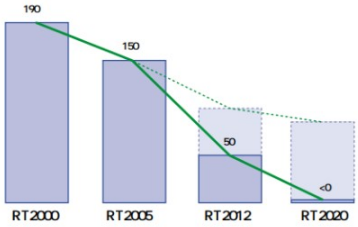

(a)

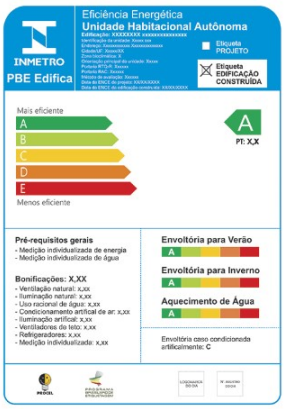

(b)

Figure 1.1: (a) Evolution of the regulatory requirements for energy consumption of new buildings in France. The dotted green line represents the predictable evolution without the adoption of the Grenelle Environment and the straight green line indicates the dynamics of reduction driven by the Grenelle Environment program. Consumption is in $kWh_{EP}/(m^2.year)$ [ADEME 2011]; (b) Brazilian energy efficiency label of a residential building [CBIE 2014].

1.1.2 Moisture problems

The control of humidity in buildings has taken great importance in recent years, an improper humidity control in buildings leads to occupants discomfort, health issues, building deterioration, mildew and mold growth, and bad odors [Chen *et al.* 2004]. Indoor humidity affects a number of health related agents, for example, high levels of humidity lead to the growth and spread of biotic agents, generating a number of health issues among which there are: infectious diseases, allergic reactions, nonallergic immunologic reactions, and myctoxicosis. Another problem of high levels of humidity is fungal contamination, which has been proven an issue above 70% or 80% RH (Fig. 1.2a). Other agents include dust mites and nonbiological pollutants. Even if most of these agents affect human health through their inhalation from the air, some of them have also effects through the skin [Baughman and Arens 1996; Arens and Baughman 1996].

Moisture in all forms (solid, liquid or vapour) can be indicated as the main factor causing building deterioration. It can lead not only to a direct attack on materials, but also to

condensation, which has been the greatest single post-war problem in building. Two and a half million homes in the UK are nowadays affected by condensation and mould growth [Ransom 2002]. Vapour pressure being usually higher inside the buildings, water vapour moves through permeable structures towards the outside, and at any point in this way, condensation is a possibility. This kind of condensation, usually called interstitial condensation, can be very harmful [Ransom 2002], causing, for example, cracking of the walls by the expansion of bricks (Fig. 1.2b).



(a) (b)

Figure 1.2: (a) Mould growth (b) Cracking caused by moisture excess on bricks. From Ransom [2002].

1.1.3 Moisture buffering materials

To guarantee a comfortable and healthy indoor climate and counteract the moisture problems in buildings, the use of hygroscopic materials can be a very interesting solution. A hygroscopic material is a substance that is capable of absorbing/desorbing moisture from/to surrounding atmosphere. This ability of the material can be used to attenuate relative humidity variations.

Figure 1.3 evidences the impact of hygroscopic materials on reducing relative humidity

variations thus improving indoor comfort. Simonson *et al.* [2002] demonstrated that wooden structures can damp moisture during humid weather in Belgium (Fig. 1.3a) lowering the variations in RH up to 20%. The darker line represents a permeable wall thus the moisture buffer effect of wood is considered, on the other hand, the lighter line does not take into account wood hygric inertia. Similarly, Fig. 1.3b shows the difference in performance between a room composed of hygroscopic materials such as hemp lime concrete (HLC) and a bio-based material called "straw lime concrete" (SLC) and a impermeable room. It is supposed that the room is occupied by 2 people from 8 a.m. to 6 p.m., which corresponds to a vapor production (G_{vp}) of 142 g/h during the period of occupation. Both materials lead to a significant reduction in the amplitude of indoor RH [Rahim *et al.* 2016].

Another advantage of using hygroscopic materials could be reducing the risk of surface condensation in a building [Zhang *et al.* 2012].

In addition, some authors pointed the importance of taking into account the effect of moisture buffering materials in numerical simulations to accurately predict variations on indoor humidity. For instance, Plathner and Woloszyn [2002] considered the effect of moisture buffering of the furniture on the calculation of internal relative humidity. The study suggests that a large portion of the moisture that is produced in the kitchen is absorbed by the kitchen walls and furniture and only a relatively small part of the moisture actually spreads to other parts of the house. Figure 1.4 illustrates the effect of considering moisture buffering by the furniture on the attenuation of relative humidity in the kitchen. Dots represents the measured values and straight line the simulated ones. It can be seen that after one hour, the calculations of vapor pressure value were closer to the measured one when moisture buffer capacity of furnitures is taken into account. Abadie and Mendonça [2009] presented a lumped model for building simulation, whose parameters can be determined from the moisture buffer capacity of materials obtained by experimental procedure. Results show that the use of this model considering material buffer capacity allows the prediction of the indoor air relative humidity evolution.

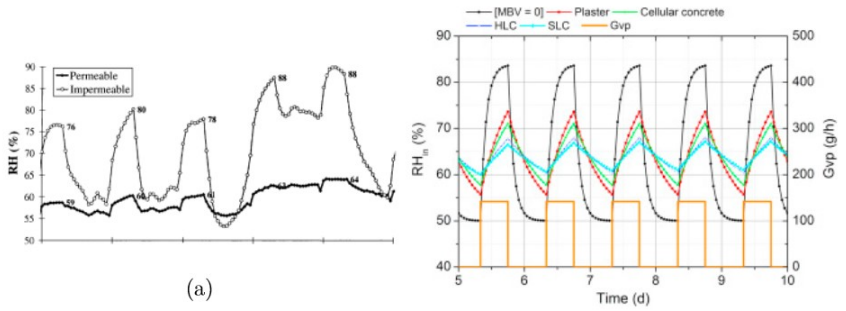

(a) (b)

Figure 1.3: Moisture buffer effect of materials on indoor relative humidity: (a) wood based material [Simonson *et al.* 2002] (b) hemp and rape-straw concretes [Rahim *et al.* 2016].

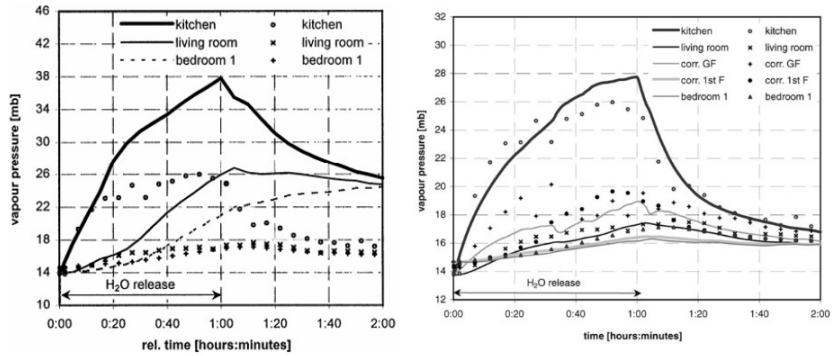

(a) (b)

Figure 1.4: Vapour release in kitchen: (a) neglecting sorption capacity of furnitures; (b) with sorption. From Plathner and Woloszyn [2002].

Indeed, such as the examples aforementioned, several other materials also have this capacity of dampen humidity when exposed in indoor and outdoor environments in building constructions. Buffering materials found in literature have different nature and can be natural, industrial or synthesized to this specific purpose. Unfired clay [Padfield 1998; Goodhew and Griffiths 2005; Hall and Allinson 2009; Allinson and Hall 2010; Ashour *et al.* 2011; Liuzzi *et al.* 2013], expanded vermiculite [Okada *et al.* 2008; Gencel *et al.* 2014], lime-hemp [Shea *et al.* 2012; Daly *et al.* 2012; Bruijn and Johansson 2013; Collet *et al.* 2008], hemp wools [Collet *et al.*

2011], sodium polyacrilate, cellulose [Cerolini *et al.* 2009], textile [Pires *et al.* 2011] are some examples of good humidity buffers.

Besides buffering capacity, some materials present other advantages such as good thermal insulation performance and low density. Moreover, bio based materials are naturally degradable [Taoukil *et al.* 2013] and clay-based usually have a large number of natural deposits [Vieira *et al.* 2008].

Sorption capacity is linked to the porous structure of the material. A high porous structure mainly composed of mesopores [Raimondo *et al.* 2007] and a wide specific area [Vu *et al.* 2013] may favor moisture buffer. This microstructural configuration also leads to materials with low density and low thermal conductivity. Vapor permeance appears to be governed by macropores [Hall *et al.* 2012]. Besides porous structure, other factors may influence in the buffering capacity. In the case of clay, mineralogy is more important for humidity buffering than changes that can be made to a particular soil (density, preparation methods or stabilisation) [McGregor *et al.* 2014b]. For instance, kaolinite type clay minerals have a lower surface affinity and surface area than montmorillonite type clay minerals which have a higher surface area due to their active interlayer space. However, porous materials may have secondary effects such as decreased mechanical strength. In the case of wood, moisture buffer rate is determined by the orientation of the fiber strands in relation to the moisture source [Svennberg 2006].

Starting from these results and considering the recent innovations introduced in material industry, this research tries to extend the unsteady characterization to highly absorbing materials coming from industrial sector. The possibility to use highly performing materials to dampen indoor RH variations could actually improve the system's efficiency, allowing to reduce the moisture buffering exposed area.

1.1.4 Fired clay in buildings

Fired clay has been one of the most widely used materials in building construction. Bricks and ceramic tiles made with baked clay can be found worldwide. Brazil is the second world producer and consumer of ceramic tiles with 899 million sq.m manufactured in 2015. This corresponds to 7.3% of world production [*World production and consumption of ceramic tiles*]. These materials are made from common clays, adapted to the requirements of the construction. They are largely used in all parts of the building (Fig.1.5) with efficiency because of their economic cost, modular-unit size dimensions, built-in design flexibility, good mechanical

resistance, durability and insulation properties. However, considering all materials mentioned on the previous section, fired clays lack of a good hygrothermal performance. Boosting the adsorption/desorption power of fired clays could be particularly interesting to take advantage of their traditional use on roofs by lowing its surface temperature or as walls/façades that could improve indoor hygrothermal comfort.

It would represent a sustainable and alternative way to cool buildings and therefore the urban area by enhancing properties of porous materials used in this urban area. In the case of lowing roof temperature, the idea is to take advantage of high relative humidity during night by adsorbing water vapor on the surface of pores and then releasing it during the day. Fig.1.6 illustrates this phenomenon. For instance, aluminium modified clays reduced roof temperature by 6.5°C having a significant potential as application materials for roof evaporative cooling [Vardoulakis *et al.* 2011a; Vardoulakis *et al.* 2011b]. Wanphen and Nagano [2009] also investigated the moisture and thermal performance of four kinds of porous and non porous materials for cooling roof purposes. Measurements showed that roof surface temperature decreases by up to 6.8°C and 8.6°C when porous materials are used.



Figure 1.5: Versatility of clay-based materials in buildings [Wienerberger 2017].

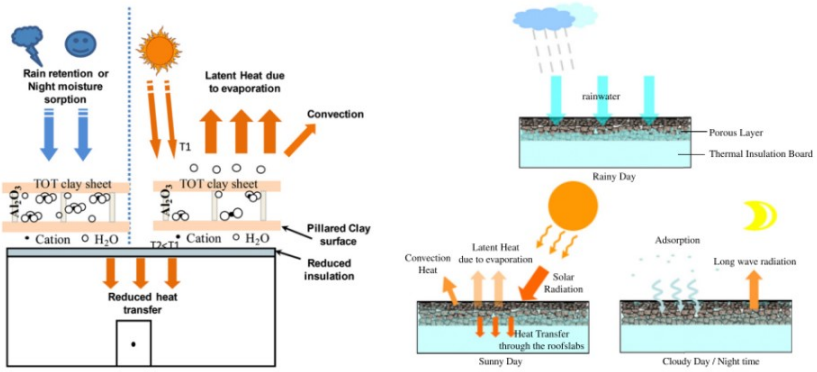

(a) (b)

Figure 1.6: Porous roof mechanism illustrated by (a) Vardoulakis *et al.* [2011b] (b) Wanphen and Nagano [2009].

1.2 Theoretical aspects of hygroscopic materials

1.2.1 Porous media

Water can be associated in materials in two different ways: by chemisorption or by physisorption. The chemical bonding is stronger and supposes a chemical reaction between water and material molecules. An example is the water bound in hydrated cement paste by covalent bonds. Water, in this case, is part of the chemical composition of the material and will not be released before material is severely degraded. In this work, this type of interaction is disregarded since materials are considered to be chemically inert. Therefore, absorbed water is only physically bounded by Van der Waals interactions and can be removed by a suitable drying method.

In the materials used in buildings, the attracted moisture is stored on porous solid structure, physically and chemically independent of the fluid contained therein (Fig. 1.7) thus there are certain physical entities related to porous medium whose definitions are relevant.

Porosity (η) which is the ratio between the volume of the porous space and the total volume of the surrounding solid:

$$\eta = \frac{V_s}{V}. \tag{1}$$

Degree of saturation (S) which is the ratio between the volume of liquid and the volume of voids:

$$S = \frac{V_l}{V_s}. \tag{2}$$

Specific surface area (S_o): it is the area of the solid/fluid interface within a material per unit of apparent volume of this material. It is a measure of the sites subject to surface phenomena, it also provides information on the average characteristics of voids.

$$S_o = \frac{s}{V} \tag{3}$$

where: s is the interstitial surface area of the voids and pores

Moisture content: it quantifies the amount of moisture in a given medium and can be represented as a ratio of volumes, masses or mass per volume.

$$u = \frac{m_w}{m_s}; \quad \theta = \frac{V_w}{V}; \quad w = \frac{m_w}{V}. \tag{4}$$

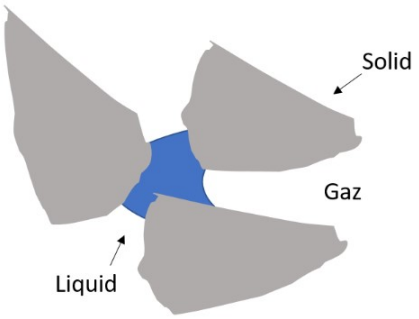

Figure 1.7: Representation of a porous medium.

According to IUPAC (International Union of Pure and Applied Chemistry) [Rouquerol *et al.* 1994], pore-size can be classified in:

Micropores have widths smaller than 2 nm.

Mesopores have widths between 2 and 50nm.

Macropores have widths bigger than 50 nm.

1.2.2 Sorption isotherms

When air that contains water molecules enters material pores, a molecular layer of water molecules is formed on the pore surface and remains thanks to Van der Waals interactions. In the mono-molecular adsorption, the vapor phase is dominant since there are not enough water molecules to form a liquid phase. With the increasing relative humidity, more molecular layers are formed under the existent ones and the layer becomes thicker. It can therefore form a liquid phase (polymolecular adsorption). When layers are thick enough to be in contact with each other forming a sort of 'bridge', liquid is retained by capillary forces and a meniscus separates the surface of contact of vapor and liquid.

The amount of water taken up by a material at equilibrium depends on the available water in the air, it means, the relative humidity. The material ability to stock moisture under different relatives humidities is given by the sorption isotherms. These curves can be quite different for distinct materials considering they are unlike in composition and morphology. As the name indicates, moisture equilibrium in sorption is influenced by temperature.

Moisture isotherms in literature end approximately at 95% RH which is called the hygroscopic range. This region begins at the dry state and the presence of water with the increasing relative humidity is due to molecular adsorption and capillary condensation. After 95% RH, there is the super-hygroscopic range in which pores are filled with water up to free water saturation. Above this range, there is the supersaturation region where there are no more equilibrium states and all cavities are supposed to be filled. In this range, material must be submitted to big pressures or immersed for long time in order to evacuate the air encapsulated in pores. Künzel [1995] illustrates these three regions (Fig.1.8).

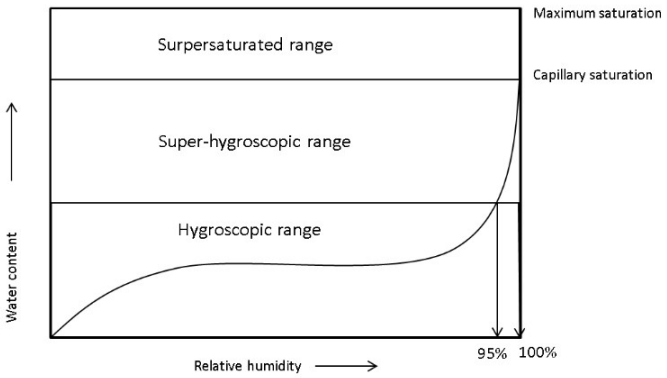

Figure 1.8: Water sorption isotherm regions for a porous material.

Usually, adsorption and desorption curves behaves differently. This phenomenon is called hysteresis and the most popular explanation is the 'ink bottle model' in which a pore with a narrow neck is filled by capillary condensation at a higher relative humidity when the RH increase than it is emptied when the RH decreases. IUPAC classifies sorption isotherms in six types (Fig. 1.9) taking into account hysteresis.

In order to represent adsorption isotherms, many theoretical, semi-theoretical and empirical sorption models have been proposed in the literature [Yanniotis and Blahovec 2009]. For instance, Hansen [1986] fitted data with an empirical model. Irving Langmuir proposed the first successful sorption model considering that sorption takes place in one layer on a surface (monomolecular adsorption) [Langmuir 1918]. However due to the simplified assumptions of this model, it is in most cases, not a suitable sorption model for water vapor on materials. Brunauer, Emmet and Teller (BET) [Brunauer *et al.* 1938] extended Langmuir model to polymolecular sorption, but it only gives a good fit to experimental data up to 40% of relative humidity. The GAB model (Guggenheim, Anderson, De Boer) has been extensively used in recent years being valid in a wider range when compared to BET model. For that reason, GAB fitting is used in this work. GAB model can be described as:

$$\frac{\theta}{\theta_m} = \frac{CK\varphi}{(1-K\varphi)(1-K\varphi+CK\varphi)}, \tag{5}$$

where:

θ_m is the volumetric moisture content when water molecules have covered the solid surface

with a monomolecular layer.

$$K = exp\left(\frac{E_L - E_m}{RT}\right), \tag{6}$$

$$C = exp\left(\frac{E_l - E_m}{RT}\right)\theta_m, \tag{7}$$

$$\theta_m = S_0 e_{H_2O}, \tag{8}$$

where:

S_0 is the specific surface area $[m^2/m^3]$;

E_l is the adsorption molar heat of the first layer [J/mol];

E_L is the latent molar heat of water vaporization [J/mol];

E_m is the adsorption heat for all molecular layers [J/mol];

e_{H_2O} is the thickness of one layer of water molecule [$\sim$3Å].

To facilitate de isotherm adjustment with the available experimental points, Eq.5 can be rewritten to Eq. 9:

$$\theta = \frac{\varphi}{\alpha\varphi^2 + \beta\varphi + \gamma}, \tag{9}$$

where:

α, β and γ can be described as:

$$\alpha = \frac{K(1-C)}{C\theta_m}, \tag{10}$$

$$\beta = \frac{C-2}{C\theta_m}, \tag{11}$$

$$\gamma = \frac{1}{CK\theta_m}, \tag{12}$$

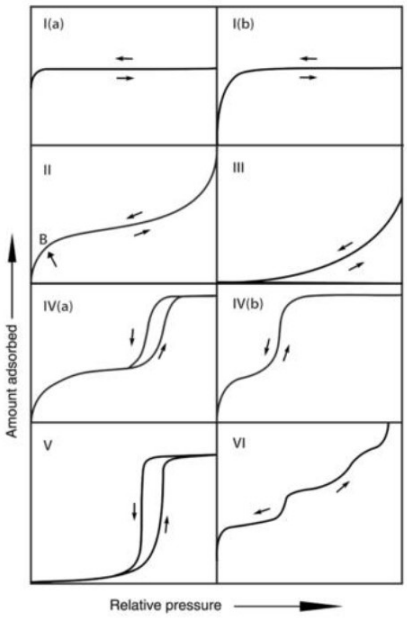

(a)

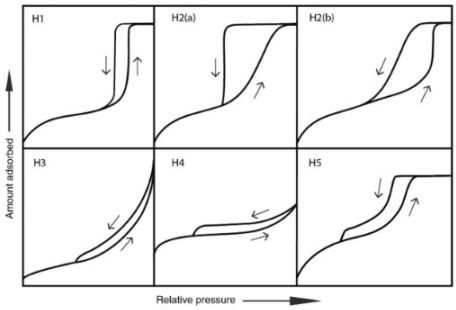

(b)

Figure 1.9: (a) Sorption isotherms and (b) hysteresis classification according IUPAC [Thommes *et al.* 2015].

1.2.3 Water vapor permeability

The previous section described how a porous materials can stock moisture vapor to reach equilibrium with surrounding air. This section relates how moisture vapor is diffused within the material.

Considering that air is a mix of water vapor and dry air, the differences in concentration of these two gases cause a transfer of vapor molecules towards the lowest concentration. Fick's law [Fick 1855] describes this behavior by:

$$g_v = -D_a \frac{\partial v_v}{\partial x}, \tag{13}$$

where:

g_v is the water vapor flux, in $kg/(m^2.s)$;

D_a is the water vapor diffusion coefficient in air, m^2/s;

v_v is the water vapor concentration, kg/m^3;

x is the position, m.

The water vapor diffusion coefficient in air can be given in function of temperature and total pressure of air by an expression of Krischer and Kast [1963] citing Schirmer's equation:

$$D_a = \frac{2.26}{P}\left(\frac{T}{273}\right)^{1.81}. \tag{14}$$

The diffusion of vapor in porous materials may consider that only part of the volume is made of open pores and factors such as tortuosity can influence in the vapor diffusion. Therefore, Eq. 13 can be rewritten as:

$$g_v = -D_v \frac{\partial v_v}{\partial x}, \tag{15}$$

where:

D_v is the water vapor diffusion coefficient in porous material, m^2/s;

Considering that water vapor is an ideal gas, the Fick's law can be expressed in function of the gradients of vapor pressure and temperature as:

$$g_v = -\frac{D_v}{R_v T}\frac{\partial p_v}{\partial x} + \frac{D_v p_v}{R_v T^2}\frac{\partial T}{\partial x}. \tag{16}$$

Compiling coefficients into a single one and for isothermal conditions, equation above can be simplified to:

$$g_v = -\delta_v \frac{\partial p_v}{\partial x}, \tag{17}$$

where:

δ_v is the water vapor permeability, in $kg/(m.s.Pa)$;

Water vapor diffusion in materials can also be expressed by a resistance factor, μ, which is the ratio between the water vapor diffusion in the material (δ_v) and the water diffusion in the air (δ_a):

$$\mu = \frac{\delta_a}{\delta_v}, \tag{18}$$

where δ_a can be calculated from D_a by an analogous process to δ_v obtainment from D_v thus modifying Eq. 14 to:

$$\delta_a = \frac{2.26}{PR_vT}\left(\frac{T}{273}\right)^{1.81}. \tag{19}$$

As shown in Fig. 1.10, in practice, water vapor permeability of materials varies with relative humidity.

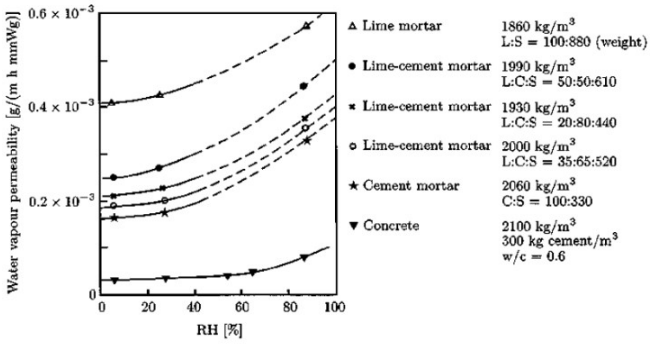

Figure 1.10: Water vapor permeability evolution with relative humidity. Adapted from Tveit [1966].

1.2.4 Liquid uptake coefficient

Capillary flow is the dominant transport mechanism in the super-hygroscopic area (Fig.1.8). In this range, moisture content is still in equilibrium with relative humidity. Thus, the capillary

transport can be expressed by the relative humidity gradient following equation as suggested by Krischer:

$$g_L = -D_{\theta,L}\frac{\partial w}{\partial x}, \tag{20}$$

where:

g_L is the liquid flux $[kg/(m^2.s)]$;

$D_{\theta,L}$ is the liquid transport coefficient associated to a moisture content gradient $[m^2/s]$;

w is the moisture content $[kg/m^3]$.

During water uptake, smaller pores provide the capillary pressure necessary, although flow mainly occurs in the larger pores because of the lower flow resistance [Larsen 1995]. The liquid transport coefficient can be measured by NMR (Nuclear Magnetic Resonance) or Gamma rays which are complicated techniques and not very easy to find.

Gravimetric method can give a convenient measure for the ability to transport water even if it cannot be used for calculations of moisture transport in general. This method has the advantage to be more simple to perform and it is suitable for comparing materials to each other. The water absorption coefficient can be calculated as:

$$Q = A_c\sqrt{t}, \tag{21}$$

where:

Q is the liquid uptake $[kg/m^2]$;

A_c is the water absorption coefficient $[kg/(m^2.s^{0.5})]$;

t is the time [s].

1.2.5 Thermal conductivity

The previous sections have shown the driving potential to moisture transfer that can be expressed by Fick's law. Analogously, Fourier's Law expresses the heat transfer based on temperature driving potential and can be defined as:

$$q = -\lambda\frac{\partial T}{\partial x}, \tag{22}$$

where:

q is the heat flux $[W/m^2]$;

λ is the thermal conductivity $[W/(m.K)]$;

T is the temperature [K].

The ability to exchange thermal energy with its surrounding air is represented the thermal effusivity:

$$E = \sqrt{\rho C_p \lambda}, \tag{23}$$

where:

E is the effusivity $[J/(m^2.K.s^{0.5})]$;

C_p is specific heat capacity $[J/(kg.K)]$;

The thermal conductivity also depends on the structure of the material and its constituents. In the case of a porous medium, the liquid and water phases coexist in the material and are variable as a function of the relative humidity. As previously described, a porous material in contact with humid air adsorbs moisture and condenses to form a liquid phase and invades the poral space by taking the place of the air. This results in a mass gain in the material which is more important in the case of materials with high porosity. It should be emphasized that the thermal conductivity of liquid water is thirty times higher than that of air. Consequently, the increase of the thermal conductivity as a function of the water content is systematic and can be not negligible especially for the case of hygroscopic materials (Fig.1.11). To this end, it is crucial to quantify the evolution of the thermal conductivity of the materials studied as a function of the relative humidity RH.

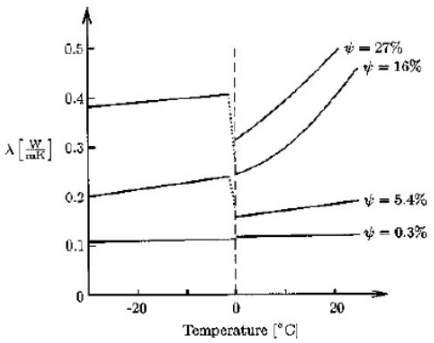

Figure 1.11: Thermal conductivity evolution with moisture content (vol-%) and temperature for aerated concrete with a density of 540 kg/m^3. Adapted from Hagemann [1981].

1.3 Literature review

1.3.1 Moisture buffer capacity

Section 1.1.3 reveled the potential of some materials to regulate indoor relative humidity by their ability to absorb moisture when relative humidity is high and desorb moisture when relative humidity is low. This is an application of moisture buffering capacity (MBC) of materials at the building scale. Considering it on the scale of the material, MBC has also been extensively studied since 1980.

Many researches measured the MBC to the scale of the material by the weight change of the sample when there is variation in relative humidity. For that, experimental setups that are capable to imitate natural environment variations on humidity were developed. Quantifying buffer ability is particularly interesting since it provides a comparison of different materials.

Padfield [1998] was one of the pioneers in characterizing hygroscopic materials using an experimental climatic chamber and in introducing the idea of moisture buffer capacity. MBC was defined as a weight change of the sample when there is variation in relative humidity. Several building materials were tested and the most efficient buffering material was wood due to its good water permeability and efficient diffusion.

Aiming to provide controlled variations on humidity and temperature to quantify MBC, high-accuracy climatic chambers are required [Meissner *et al.* 2010], which may not be available

in many laboratories. Therefore some researches proposed alternative features to establish a given level of relative humidity. Svennberg [2006]; Osanyintola and Simonson [2006]; Li [2011]; Zhang *et al.* [2017b] proposed a simple experimental facility based on the gravimetric method to measure adsorption and desorption capacity of the materials. It consists of a ordinary glass jar with saturated salt solutions as humidity generators. The lid is modified, with a large hole covered by a washer with small hole, to allow the sample to remain inside the jar during the complete experiment. The sample is hung in a steel wire and a rubber tube on the steel wire acts both as seal for the minute hole in the washer and as a stopper so the sample is stopped from falling down when the sample is not in a weighing position. The sample is weighed with a balance that is place on the top of the lid. This method has the inconvenient of a limited sample size and unknown and uncontrolled air velocity on the material surface which can affect measurements.

Besides the experimental measurements, Peuhkuri *et al.* [2004] analyzed analytically the behavior of hygroscopic materials with humidity variations, using a formula that relates volumetric moisture capacity of the material, the variation of ambient relative humidity and the penetration depth. These calculations guided a theoretical index proposed during a project (NORDTEST) [Rode 2005] which aimed to standardizes the moisture buffer capacity.

NORDTEST project provided a robust definition of moisture buffer capacity and confirmed the relevance and benefits of using moisture buffering materials in public and industrial sectors. The project presented two concepts: MBV_{ideal} and $MBV_{practical}$. Ideal conditions consider that moisture transfer has no resistance when flow is in or out of the material. However it is not valid for practical conditions even if climatic chambers are used. Therefore it was introduced the concept of moisture buffer value practical, $MBV_{practical}$, and it is defined as:

> $MBV_{practical}$ is assumed a surface resistance corresponding to normal air flow conditions seen in indoor environments (air velocity between 0.05 and 0.15 m/s), and an exposure with daily variations with 8 hours of high air humidity (75 % RH) and 16 hours with low humidity (33 % RH).

$MBV_{practical}$ can be classified according NORDTEST project as negligible, limited, moderate, good and excellent and it is illustrated in Fig.1.12.

Before NORDTEST, in 2002, a Japanese standard of building material [JIs 2002] proposed a method to test materials that regulate indoor relative humidity. Comparatively with NORDTEST, both benches acquired similar responses when comparing the same materials despite using different forms of measurement. The Japanese standard provides a time of 24 hours to carry

out the high humidity cycle and a further 24 hours for the low humidity cycle; the humidity range being between 53 and 33% RH, 75 and 53% RH and 93 and 75% RH. The standard proposed by Rode [2005] foresees a greater variation of humidity (33 to 75% RH) and cycles of 8 hours with high humidity and 16 hours with low humidity, representing daily oscillations. The comparative study also shows that when applying the concepts in simulations of work environments, the MBV implies better results, since its method of obtaining was taking into consideration the real conditions of a work environment [Roels and Janssen 2006].

Although NORDTEST is a widely used standard to assess moisture uptake/release by porous materials, some authors proposed new evaluation methods for moisture buffering effect. Considering that NORDTEST is limited to a sample material in a constant temperature and humidity oven, Zhang *et al.* [2012] proposed an index that is dimensionless. It was named moisture adsorption effect (MBE_a) during humidification period and moisture desorption effect (MBE_d) during decay period. In the calculation of these indexes, it was considered the mean value of the measured humidity ratio in air and the calculated result for indoor humidity ratio variation when there is no moisture buffering interaction. Therefore, MBE_a and MBE_d mean the ratio of humidity variation restrained under the influence of the hygroscopic material, compared with the case without moisture adsorption and desorption. Thus, the larger values of MBE_a/MBE_d are, the better effect of moisture absorption/desorption are. Latter, Zhang *et al.* [2017b] developed a new mathematical expression of MBV with a correction factor which takes into account a new cyclic step-change in relative humidity with a view to approach real conditions.

Some authors pointed the importance of taking into account other parameters during material characterization. It was found that moisture adsorption/desorption capacity increases exponentially when air change rate decreases. Moreover, a higher humidity level in the ventilation air increases the indoor humidity level, consequently enhancing the moisture buffering effect. [Umurigirwa *et al.* 2014; Zhang *et al.* 2012; Yang *et al.* 2014; Zhang *et al.* 2017a]. Thus predicting the behavior of the sample at different RH levels could be done considering the kinetic of this materials at two different amplitudes of RH variation and extrapolating this discrepancy from one test to the other [Delgado *et al.* 2006]. Increasing the rate at which the water vapour reaches into the deeper layers of the material and the air velocity can therefore raise the moisture adsorption [McGregor *et al.* 2014a].

Material properties also influence moisture buffering capacity. Increasing thickness of the sample leads to an augmentation in the moisture capacity until a limit [Rahim *et al.* 2015].

This maximum value is known as the moisture penetration depth. It was found that the penetration depths have an inverse relationship with the time required for the hygroscopic materials to reach a new equilibrium under a step-change moisture load or to reach a stable moisture buffering cycle under cyclic moisture loads [Ge *et al.* 2014]. Materials with higher vapor permeability have a greater moisture buffering potential under short-period and when the area of hygroscopic materials, involved in moisture balance of the indoor environment, increases, more moisture can be buffered [Zhang *et al.* 2012]. Moisture storage capacity is also influenced by the variable surface charge of the clay particles and their size which means that finer and clay minerals such as a montmorillonite significantly increases the moisture capacity [McGregor *et al.* 2014a].

Several researchers investigated different moisture buffering materials and table 1.1 summarizes the mainly findings of published works.

Despite of imperfections, NORDTEST is a widely used and validated standard thus it will be adopted in this work.

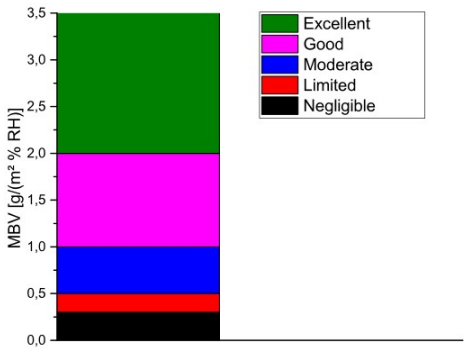

Figure 1.12: $MBV_{practical}$ classes according NORDTEST [Rode 2005]

Table 1.1: Moisture buffer materials in literature.

Materials	Buffer capacity	Test conditions	Experimental set-up	Reference
Plasterboard Cellular concrete	RH attenuation : Plasterboard = Cellular concrete = 50%;	daily variation in the test cell was humidification and dehumidification moisture load of 25 g water/hour. T= 20°C	Air and moisture tight test room of 38.0m^3	Mortensen *et al.* [2005]
Glass wool Cellular concrete Cellulose insulation Flax insulation sheep's wool perlite	22 g_{water}/m^2 per $\Delta\varphi$= 0.1 11 65 78 48 7	ΔRH =10% for 24h at 22°C	Cylindrical climatic chamber of stainless steel, 790 mm diameter and 500 mm deep	Peuhkuri *et al.* [2004]
Gypsum plasterboard Gypsum plaster Plywood Cement plaster Cement	1.25 $g/m^2\%\Delta\varphi$ 1.13 $g/m^2\%\Delta\varphi$ 1.30 $g/m^2\%\Delta\varphi$ 0.73 $g/m^2\%\Delta\varphi$ 0.76 $g/m^2\%\Delta\varphi$	12/12 hrs cyclic steps between 65 and 85 %RH and 33 and 75 %RH for plywood	Climatic chamber with a precision balance inside	Delgado *et al.* [2006]
Interior furnishing	Empty room: RH variation 35% and 80% Furnished room: RH variation 40% and 70%	daily moisture load of 33g/h for half day followed by a similar period of condensation. T=21°C	Highly insulated steel box standing on pillars with indoor floor area of 13.8m^2 and room height of 2.75m^2	Svennberg *et al.* [2004]

Table 1.1: Moisture buffer materials in literature.

Materials	Buffer capacity	Test conditions	Experimental set-up	Reference
Spruce boards	1.22 $g/m^2\%\Delta\varphi$	A cycle of 8 h at 75% RH followed by 16 h at 33% RH at 23°C	Retangular climatic chamber, 1100mm X 600mm	Rode [2005]
Concrete	0.42 $g/m^2\%\Delta\varphi$			
Gypsum	0.69 $g/m^2\%\Delta\varphi$			
Laminated wood with varnish	0.46 $g/m^2\%\Delta\varphi$			
LW aggregate concrete with stucco	0.74 $g/m^2\%\Delta\varphi$			
Cellular concrete	1.05 $g/m^2\%\Delta\varphi$			
Brick	0.39 $g/m^2\%\Delta\varphi$			
Birch panels	0.91 $g/m^2\%\Delta\varphi$			
Light weight wood	1 $g/m^2\%\Delta\varphi$	A cycle of 8 h at 75% RH followed by 16 h at 33% RH at 23°C	$8m^3$ cubic test-cell made of the hygroscopic material to be tested	Meissner [2008]
Sodium polyacrylate	8.97 $g/m^2\%\Delta\varphi$	A cycle of 8 h at 75% RH followed by 16 h at 33% RH at 20°C	Climatic chamber Angelantoni CH250	Cerolini *et al.* [2009]
Cellulose	3.07 $g/m^2\%\Delta\varphi$			
Gypsum board	1.06 $g/m^2\%\Delta\varphi$			
Porous ceramic pipe	Cumulative evaporation for the day was $932g/h$	$T_{max} = 30$ and T_{min}=19°C. The daily mean relative humidity was 62% and mean wind speed 0.5 m/s	Ceramic pipe placed in an outdoor location on a clear sunny day.	He and Hoyano [2010]

Table 1.1: Moisture buffer materials in literature.

Materials	Buffer capacity	Test conditions	Experimental set-up	Reference
Perforated unfired clay wood massive unfired brick cellular concrete	27 m^3water/m^2 material 15 m^3water/m^2 material 10 m^3water/m^2 material 7 m^3water/m^2 material 3 m^3water/m^2 material	Cyclic RH variation between 50% and 60% for one day. T=20°C.	Cylindrical climatic chamber of stainless steel, 790 mm diameter and 500 mm deep	Padfield and Jensen [2011]
Wood pannels	Peaks reduced from 60% to about 30% RH	Moisture generation of 42g/h for 8h followed by a similar period of condensation. T=21°C	Two boxes of: 7.5m X 4.4m X 3.6m and 7.5m X 4.4m X 6.1m	Li [2011]
Polyester spacer fabric with honeycomb structure	Evaporated water to absorbed water ratio (%)=91.4; Evaporated water to dry sample mass ratio (%)=208.3	Absorption: immersion into a water bath, at atmospheric conditions, until saturation. Desorption: drying process taking place in a test tunnel at 30°C	Test tunnel	Pires *et al.* [2011]
Hemp-lime	φ maintained at 60%	Real external relative humidity varying from 90% to 30%	Building with a floor area of approximately 27m^2.	Shea *et al.* [2012]
Baked clay	At the largest loading ratio, 40 to 90% $\Delta\varphi$ were restrained	Pre-conditioning of 24h, humidification of 6h (30-80 g/h), decay period 24h	Test room of 1.82 m X 1.82 m X 2.02 m	Zhang *et al.* [2012]
Unfired clay	1.13 - 3.73 $g/m^2\%\Delta\varphi$	A cycle of 8 h at 75% RH followed by 16 h at 33% RH at 23°C	Environmental chamber	McGregor *et al.* [2014b]

Table 1.1: Moisture buffer materials in literature.

Materials	Buffer capacity	Test conditions	Experimental set-up	Reference
Hemp concrete	1.85 - 2.65 $g/m^2\%\Delta\varphi$	A cycle of 8 h at 75% RH followed by 16 h at 33% RH at 23°C	Climatic chamber	Oumeziane *et al.* [2014]
Bio-based composite made with hemp fibres and wheat starch as a binder	4,25 $g/m^2\%\Delta\varphi$	A cycle of 8 h at 75% RH followed by 16 h at 33% RH at 23°C	Climatic chamber	Umurigirwa *et al.* [2014]
Uncoated gypsum board wood paneling	226g accumulated moisture 236g	4.7 g/kg HR supply air, 103.6 g/h for 10 h moisture generation, 0.5 ACH	Test room of 3.62 m X 2.44 m X 2.43 m	Yang *et al.* [2014]
Rape straw lime concrete Hemp lime concrete	2.59 $g/m^2\%\Delta\varphi$ 2.02 $g/m^2\%\Delta\varphi$	A cycle of 8 h at 75% RH followed by 16 h at 33% RH at 23°C	Climatic chamber (CL2 Biaclimatic Type-25)	Rahim *et al.* [2015]
Rammed earth	2 $g/m^2\%\Delta\varphi$	A cycle of 8 h at 75% RH followed by 16 h at 33% RH at 23°C	Climatic chamber	Arrigoni *et al.* [2017]

1.3.2 Improving fired clay hygroscopic capacity

Fired clay has been one of the most widely used materials in building construction. Bricks and ceramic tiles made with baked clay can be found worldwide. As a result of the large usage of these materials and economic cost, some researches aimed to ameliorate their mechanical resistance, durability, insulation properties and hygrothermal performance.

Bories *et al.* [2014], Velasco *et al.* [2014] and Munoz *et al.* [2017] presented reviews about the enhanced physical, mechanical and thermal properties of clay bricks by using pore-forming agents. First of all, it must be mentioned that the components of the clays may influence their properties including the porosity and thus their hygroscopic behavior. For example, Munoz *et al.* [2017] highlighted the influence of the clay composition on the aforementioned properties. Increasing SiO_2 content raises porosity, lowers density and mechanical resistance. Al_2O_3, the second most common clay component, leads to better mechanical properties due to the formation of mullite during firing process. Iron oxides which normally do not exceed 10% content leads to discoloration and/or efflorescence during firing process. In the case of calcareous clay (CaO $>$ 8%) when CaO reacts with silica, it provides an increase of mechanical resistance and a reduction of the firing shrinkage.

By considering the type of additive, it can be said that organic additives can be incorporated into the clay mixture before firing and burn during the heat process leading to the creation of voids that diminishes density providing lighter materials. Thermal conductivity is also affected since the creation of these voids within the structure, in other words, porosity, increases the air contained in these empty spaces and so thermal conductivity falls. However, porosity also weakens the structure decreasing mechanical resistance of materials. Thus, a compromise between these properties must be found. Inorganic residues produce different effects on brick properties depending on the type and show a lower correlation factor in results than the obtained for the organic residues. The introduced metals and minerals to clay matrix react in very different ways, melting or forming new phases thus modifying the crystal structures. In general, most of inorganic residues lead to a proportional relation between mechanical properties and bulk density. In contrast, bulk density can be increased while the body strength is weakened if some compounds remain inert at firing temperatures [Munoz *et al.* 2017].

In addition, the researches pointed that incorporating additives into a clay matrix may save energy in the manufacture process by the self combustion of aggregates, it can be also a way to recycle wastes and sometimes it could reduce water addition during manufacturing process

then improving the plasticity of the blend.

Novais *et al.* [2015] produced ceramic tiles with controlled porosity by using pore-forming agents as well. The ceramic discs were designed to obtain a dense top-layer, 4mm thick, and a porous bottom-layer with a similar thickness. The content of pore forming agent was an industrial spray-dried powder.

Another way to tune porous structure of fired clay materials is controlling sintering temperature. This parameter affects the porosity, pore-size and the transformation of minerals into other phases. Many researches agree that increasing firing temperature diminishes porosity promoting a denser structure, better mechanical properties, durability, but low thermal insulation and water absorption [Dondi *et al.* 1999; Riccardi *et al.* 1999; Monteiro and Vieira 2004; Cultrone *et al.* 2004; Karaman *et al.* 2006; Lee and Yeh 2008; Baccour *et al.* 2009; Trindade *et al.* 2009; Johari *et al.* 2010; Rathossi and Pontikes 2010; Ngun *et al.* 2011; Serra *et al.* 2015; Alves *et al.* 2016].

Nigay *et al.* [2017] induced porosity during the heat treatment of a clay-based ceramic by heating it up to 850°C and taking advantage of minerals transformation. Figure 1.13 illustrates the evolution of porosity during the heat treatment of a clay-based ceramic. The initial porosity is due to air trapped during sample mold/extrusion. This porosity value is then raised by the water released during drying process and constrained by the shrinkage from 100°C to 250°C. Between 450°C and 600°C, dehydroxylation (release of constitution water from the kaolinite−group and illite−group minerals) takes place leading also to an increase in the void numbers. Finally, decarbonation of calcite forms porosity from 650°C to 850°C. The decrease of porosity starts only after 850°C with elimination of the smallest pores due to the densification process. Moreover, the diminution in mechanical strength owing to the presence of pores was counteracted due to the formation of smaller pores than the 200 μm sheets of porosity.

Although there are several types of tests related in literature, hygrothermal performance is still rarely reported being mainly about hygroscopic property of raw materials and simple building materials (section 1.1.3). There is only a few data in the literature about humidity-control fired clayey materials and their complex structure in relation to hygroscopic properties.

Different techniques in the development of environment friendly humidity-control materials for indoor thermal management and humidity control were reviewed by Rao *et al.* [2012] but none of them was used to produce fired clay materials. For instance, Li [2005] optimized the water adsorption/desorption properties of the sepiolite by acid and heat treatment increasing

number of both micropores and mesopores. At low relative humidity (<43%), the hygrothermal performance is mainly influenced by specific surface area. At medium and high RH (>43%), the main factor is pore volume and pore distribution.

Wu *et al.* [2014] greatly improved the hygroscopic properties of a mortar by adding wood fiber, sepiolite and expanded perlite to its structure while conferring the material good mechanical and thermal insulating properties. The novel inorganic porous fibre-aggregate mixture has its adsorption ability directly proportional to the specific surface area and mesoporous distribution, but inversely proportional to the total pore volume. Same findings were reported by Vu *et al.* [2013] which verified that the best performance as a humidity control was given by a material with high specific surface area and with mesopore structure. The authors mixed diatomite, volcanic ash and sodium perborate to obtain a material with the mentioned characteristics. Sodium perborate promoted a reduction on the pore diameter in the final products while diatomite increased the surface area. To confer fine mechanical properties, the mix was sintered at 1000°C.

Hall *et al.* [2012] syntetized mesoporous silica (MS) with a higher buffering capacity with controlled pore diameter by changing the length of the surface directing agents and the introduction of organic auxiliary chemicals. Despite the relationship with the mesopore size that favors moisture adsorption, the study suggested that vapor permeance of an MS desiccant substrate is dominated by the macropore geometry and this could influence vapour sorption/desorption response rates at significant thicknesses.

Shang *et al.* [2017] enhanced the humidity-controlling properties of gypsum, by preparing a new type of composite using the sol-gel method. It consisted in using gypsum and plant fiber as the matrix material and adding different amounts of the humidity-controlling gel (produced with a mix of inorganic salts and reagent grade) as the activator. A coarse network with tiny pores is observed on the surface of the new composites, and this pore network provides sufficient space for moisture adsorption.

Likewise, to create a cooler urban environment, a passive evaporative cooling wall (PECW) was constructed using porous ceramics [He and Hoyano 2010]. This material has extremely thin pores, with a diameter of between 5 and 50μm, creating a water-soaking effect.

In devising sorptive applications, one must consider such clay characteristics as microporosity, capillary structure, surface area and active sorption sites (especially silanol groups), as well as grain size and mechanical strength of granules, and the features of the liquid to be absorbed. Absorption is dependent on liquid density, viscosity, and surface tension, which determine

capillary suction by clay granules; adsorption is even more markedly influenced by the size, shape, and polarity of the molecules involved [Galan 1996].

Therefore, with a view to obtain materials with enhanced hygrothermal properties with fine mechanical properties, one of the possibilities is modifying the porous structure of the traditional ones. It can be accomplished by incorporating substances that will act as mesopore-forms and consequently, inter alia, increase the available surface for moisture adsorption and desorption. Moreover, aggregates with high adsorption capacity could provide more room for expansion of the hydrophilic group and raise the number of active sorption sites. Sintering temperature also alters pore size distribution thus highly affects the material hygrothermal properties.

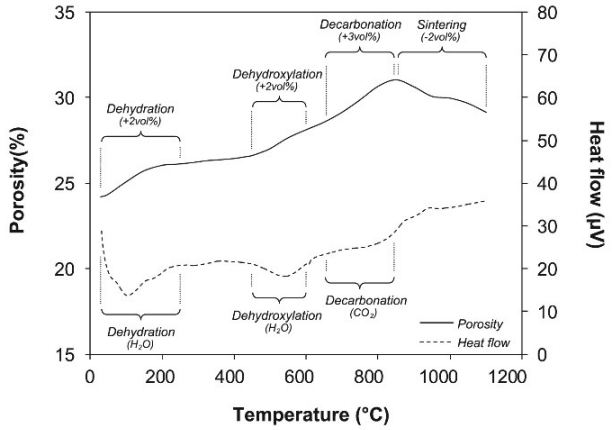

Figure 1.13: Impact of sintering temperature on the porosity of clay-based ceramic [Nigay *et al.* 2017].

1.4 Conclusion

This chapter is divided in four sections. The first one presents the importance of taking moisture into account in the building sector. The excess of moisture can be a root of mould growth, diminution of materials durability and the origin of healthy problems. Furthermore, energy efficiency of buildings is affected by relative humidity variations.

A sustainable solution to counteract these problems, is using materials that can adsorb/desorb moisture. They can control the amplitude of relative humidity in buildings using their own porous structure. However, traditional building materials such as fired clay do not have this good capacity to buffer moisture. Therefore, a section is dedicated to literature review of

how to improve fired clay buffer performance. This can be accomplished by the addition of pore-forming, high surface area agents and adjusting firing temperature. This information is especially interesting and these techniques will be used, in the next chapter, to produce fired clay with enhanced hygroscopicity.

The theoretical aspects of hygroscopic materials were also reported. They were the basis of the characterization of the hygrothermal properties in the experiments performed on Chapters 4 and 5. Particular emphasis was given to the index that represents moisture buffer capacity of materials (MBV) and how to quantify it.

Finally, the influence of moisture buffer materials on hygrothermal comfort in a room scale was also reported inspiring results of chapter 5.

Chapter 2

Materials processing and physical characterization

This chapter focuses on the fabrication and physical characterization of the clay-based materials. It presents a study of sintering conditions and absorbent addition on clay, and their influence on physical and mechanical properties of materials. Conclusively, the best sintering temperature and mixing proportions were selected with a view to characterize hygric properties and microstructure of the produced materials in the further chapters.

Contents

2.1 Introduction **41**
2.2 Elaboration of fired clay-based materials **41**
2.3 Materials **43**
2.4 Preparation steps **54**
2.5 Physical characterization **55**
2.6 Mechanical properties **57**
2.7 Results **57**
2.7.1 Physical properties 57
2.7.2 Mechanical properties 65
2.8 Conclusions **66**

2.1 Introduction

Chapter 1 showed that several materials have the capacity of dampen humidity when exposed in indoor and outdoor environments in building constructions. The possibility to use these high absorbing materials could provide energy consumption and improve thermal comfort in buildings. Among all materials, clay is presented as an interesting constituent since it can be formed into any shape, it has good mechanical resistance, durability and is widely used. Consequently improving clay hygrothermal behavior could be a very interesting use for cooling building purposes.

In this chapter, cheap and abundant absorbents were incorporated to clay to improve its capacity of adsorption and desorption of moisture.

In addition, section 1.3.2 pointed the influence of sintering temperature on pore structure of fired clay materials. Therefore, the influence of thermal treatment was investigated in order to optimize the fabrication process and to obtain enhanced hygrothermal properties.

Parameters such as heat rate and firing time can also affect materials properties but it would represent a great number of parameters to variate. Based on the investigation of Karaman *et al.* [2006] which concluded that the time the material was subjected to the firing process at a corresponding temperature had no significant effect on mechanical strength, water absorption and density of materials, we decided to maintain one value for each variable.

Finally, a physical characterization of elaborated materials provides important data to the following chapters.

2.2 Elaboration of fired clay-based materials

In general, the production of bricks and roof tiles is quite similar. The mainly raw material is clay. Some stages are necessary to get the final product as illustrated in the flow chart above (Fig.2.1).



Figure 2.1: General flow chart of clay brick/tile production.

1. *Raw material extraction* is made from clay mining sites.

2. *Preparation* comprises griding and milling processes in order to remove stones and other organic material. This step also aims to provide a good homogeneity and consistency of clay and hence water and other agents such as pore forming or sand can be added.

3. *Shaping* can be made by extrusion or by compressing clay in molds.

4. *Drying* prepares bricks for firing and it is important to avoid cracks in the final product. Bricks drying can last from 4 to 48 hours.

5. *Firing* bricks gives them durable strength as well as non-flammable and fire-proof characteristics. During this step, there is a significant microstructural changing which affects the final properties of the brick and that is the reason for what this stage is studied with more details in section 2.2.

The sintering (firing) of ceramic materials is the method that involves the consolidation of particles of ceramic powders by heating the piece after drying (green body). Firing occurs at high temperatures, below the melting temperature, where the material of the separated particles diffuses into neighboring particles [Rahaman 2007].

The green bodies produced by a forming process, such as molding, forming and pressing, contains, in addition to the mixtures of ceramic powders, water, and organic additives with deflocculants, binders and plasticizers. All these components are volatile at high temperatures, and must be removed prior to firing to prevent damage to the ceramic part.

All particles in a green body are surrounded by a film of water. When this water is removed by drying, a volume reduction occurs, known as a drying contraction. The drying contraction increases with the amount of water in the piece. The contraction also depends on the particle size and the forming process.

The driving force for the sintering process is the reduction of the surface energy of the particles caused by the reduction of solid-vapor interfaces. During the diffusion process, the pores in the "green body" decrease resulting in densification of the material, and improving the mechanical properties. The decrease in porosity is determined by the amount of initial pores, the temperature and time of the burn.

When clays are submitted to a process of firing, chemical reactions and fusion of components can modify the microstructure and consequently the physical and hygric properties of the material [Johari *et al.* 2010]. That is why firing temperature plays a very important role on clay properties and it is studied it this section. Figure 2.2 shows a schematic representation of the sintering process.

Firing process improves mechanical strength of materials and makes them permanently non-flammable. Clay bricks and tiles firing temperature typically ranges between 800°C and 1200°C.

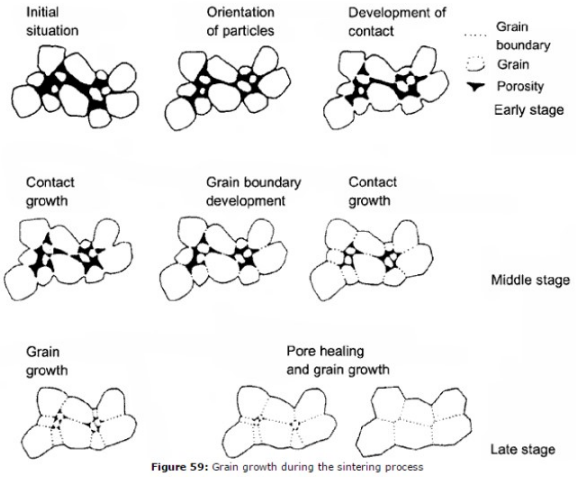

Figure 2.2: Sintering process [*Breviary Technical Ceramics*].

2.3 Materials

In the preparation of highly absorbing material by sintering process, clay is mixed with nine absorbent materials (attapulgite, diatomite, sepiolite, vermiculite, perlite, montmorillonite and zeolite), which are abundant in deposit. They are mainly sold as industrial liquids absorbents. Sepiolite is used in three different particle sizes. Attapulgite was sourced by Eurosorb in France, diatomite, sepiolite and montmorillonite by Textiles Essuyages in France and perlite and vermiculite by Boutin gardening in Brazil. Zeolite comes from Tosoh corporation. Clay was provided from a tile and brick company located in Curitiba, Brazil. Table 2.1 shows the characteristics of raw materials used in this work which were provided by the respective suppliers.

Table 2.1: Characteristics of raw materials.

Absorbents	Density (kg/cm^3)	Granulometry (mm)	Main applications
Attapulgite	600	0.30 - 0.80	Absorption of most liquids (hydrocarbons, water, chemicals etc ...).
Diatomite	505±0.5	0.50 - 1.4	Absorption of greases and oils in outdoor areas.
Montmorillonite	560	0.31 - 0.75	Absorption of most liquids (oil, emulsion, inks, ...).
Perlite	64 - 80	3 - 10	Thermal or acoustic insulation, water retention and soil aerator for agriculture.
Sepiolite			
Ultra-fine	660±10%	0.20 - 0.85	Absorption of liquids (oils, fuels,
Sand	640±10%	0.85 - 1.18	chemicals, water, etc.)
Granulate	690±10%	1.18 - 4.75	
Vermiculite	75 -80	0.5 - 4	Animal feed, foundry, horticulture, thermal and acoustic insulation in buildings.
Zeolite	Not mentioned	2.38 - 4.76	Adsorption of gases generated during semiconductor manufacturing processes.

2.3.0.1 Perlite

The name of perlite is a derivation from "Perl stein" originally given to certain glassy rocks with numerous concentric cracks, from the fancied resemblance of broken fragments to pearls [Samar and Saxena 2016] (Fig.2.3). Petrographically, perlite is a glassy volcanic rock which belongs to the same family of volcanic glasses as obsidian, pitchstone, pumice and scoria [Herskovitch and Lin 1996]. The chemical composition of the perlite contains SiO_2 with oxides of Al, K, Na, Ca, Mg, R_2O_3 and bound water (3.0%).

Raw perlite when heated (above 870°C) expands and transforms into a cellular material. The vaporization of the chemical water held within the perlite is responsible for this expansion process creating bubbles in the heat softened rock (Fig.2.4). The formation of these bubbles

allows perlite to expand even 15-20 times of its original volume and produces froth-like structure [Pichór and Janiec 2009]. This structure gives excellent insulation properties [Topçu and Işıkdağ 2007] and high absorption of sound [Yilmazer and Ozdeniz 2005]. Moreover, perlite is usually used as water retention and soil aerator for agriculture and horticulture due to its high porosity and low density [Singh and Garg 1991].

It has been also used to improve the hygroscopic properties of the mortars by adding a mix of wood fibre, sepiolite and expanded perlite being especially useful in constructions under high temperature (40°C) and high relative humidity (98%) during summer [Wu *et al.* 2014]. In addition, Padfield [1998] designed lightweight clay made from bentonite mixed with perlite that gave an excellent hygrothermal performance.

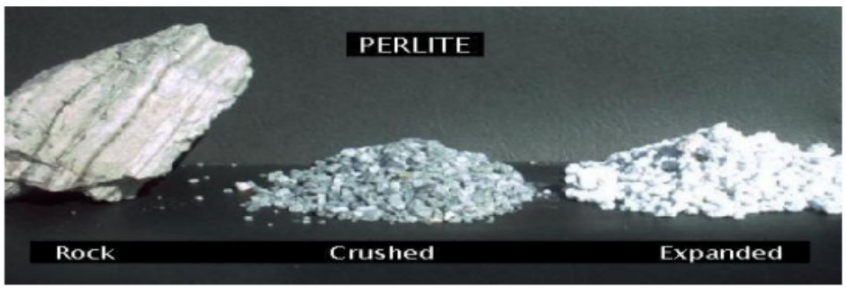

Figure 2.3: Petrological forms of perlite [Samar and Saxena 2016].

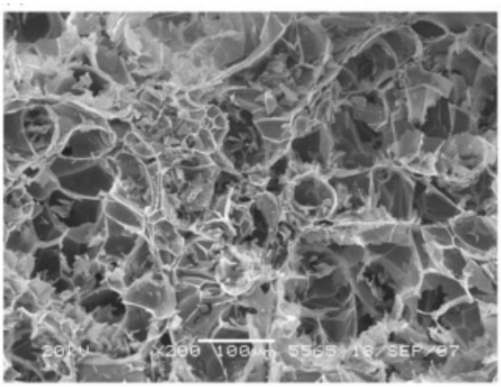

Figure 2.4: Scanning electron microscopy image of expanded perlite [Wu *et al.* 2014].

2.3.0.2 Montmorillonite

The name montmorillonite (after Montmorillon, France) was originally applied to a clay mineral with composition similar to that of pyrophyllite, except for the presence of excess water, $Al_4Si_8O_{20}(OH)_4.nH_2O$. Chemical variation of this basic formula yields a group of clay minerals which are related by common structure and by similarity of chemical and physical properties, and it belongs to the group of smectites. One member of this group is itself called montmorillonite and has the formula $Na_{0.7}(Al_{3.3}Mg_{0.7})Si_8O_{20}(OH)_4.nH_2O$.

The mineral structure consists of superimposed layers each of which contains a plane of Al ions sandwiched between two inward pointing sheets of linked tetrahedral (2:1 layer structure). In the central section of $Al_2(OH)_6$, two out of every three OH ions are replaced by apical oxygens of an Si_4O_{10} pseudo-hexagonal network. The charge balance is upset by substitutions in both octahedral and tetrahedral sites and is redressed by the presence of small number of interlayer cations, usually Na and Ca. The basal spacing can vary over a wide range with a minimum, corresponding to the fully collapsed state, at about a 9.6Å. Water is readily absorbed between the structural layers; it enters as integral numbers of complete layers of water molecules arranged in specific manner with relation to their neighboring tetrahedral networks (Fig. 2.5). The number of layers of water molecules is influenced by nature of the inter-layer cation: Ca montmorillonites usually having 2 layers per cell (d=15.5Å) and Na varieties having one (d= 12.5Å), two (15.5Å), three (19Å) or more layers per cell [Kawagoe *et al.* 2014]. A characteristic feature of montmorillonite is the extensive surface for the adsorption of water and ions, therefore the cation exchange capacity is very high.

The structural characteristics influence directly in these properties. The montmorillonite clay is type 2:1 expanding, because of this interlayer bonding is very weak. The cation exchange capacity (CEC) is high (80-150 $cmol/kg$), which is driving by negative charges resulting from partial substitution of Al by Mg, also by exposition of some O and OH groups in the flat external surfaces. The specific surface (700-800 m^2/g) is high, resulting from increase of the interlayer area [White 1987].

The expanding capacity is related directly to the quantity of water absorbed. Experimental Na-saturated montmorillonite hydrate with three layers of water was found be stable up to 340°C and 2 $\pm$ 1 kbar of H_2O pressure. It dehydrates to montmorillonite with one H_2O layers at 483°C and 4.4 $\pm$ 1.3 kbar, which in turn, dehydroxylates or melts at 525°C and 5 $\pm$ 1.4 kbar. These conditions are much lower than those found at lower pressures. Results confirm

that the dehydration temperature of montmorillonite significantly increases with increasing H_2O pressure, consistent with the idea that the density of interlayer H_2O in montmorillonite is higher than that of pore H_2O [Huang *et al.* 1994].

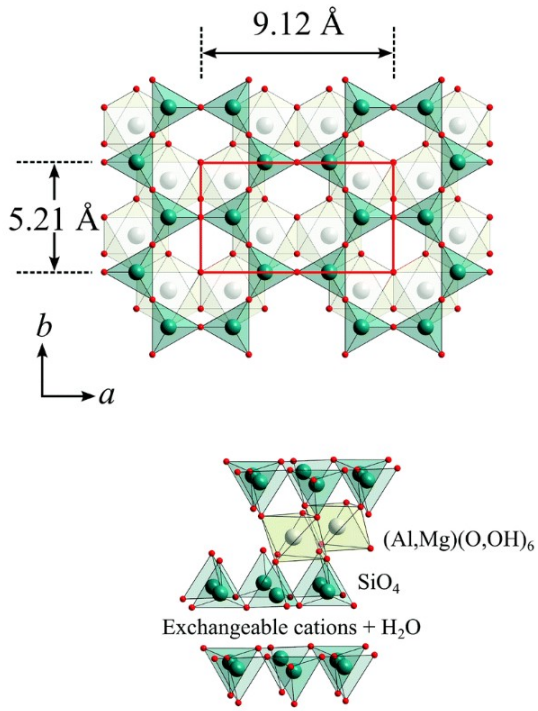

Figure 2.5: The crystal structure of montmorillonite projected on ab and ac axes, showing the position of the water entrance.

2.3.0.3 Vermiculite

Vermiculites are 2:1 phyllosilicates generally composed of macroscopic particles, similar in appearance to micas. In general, macroscopic vermiculites are of secondary origin and result from alteration of micas (phogopites or biotites), chlorites, pyroxenes or other similar minerals as a result of weathering, hydrothermal action, percolating grouns water, or a combination of the three effects [Calle and Suquet 1988]. The name, which is derived from Latin vermiculare, to breed worms, alludes to the peculiar exfoliation phenomenon exhibited when specimens are rapidly heated.

In its natural state the mineral has little useful application, but when exfoliated (Fig. 2.7) and included in the matrix of building materials, it decreases mechanical strength, density and thermal conductivity and it increases porosity, water absorption, workability and fire resistance [Rashad 2016]. The structure of vermiculite contains a central octahedrally coordinated layer of Mg and Fe ions which lies between two inward pointing sheets of linked SiO_4 tetrahedron.

The expanded vermiculite was also found to be an important porous material to counteract heat island effect due to its moisture buffer ability [Okada *et al.* 2008; Gencel *et al.* 2014].

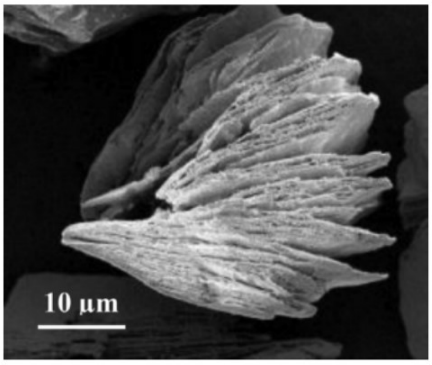

Figure 2.6: Scanning electron microscopy image of expanded vermiculite [Rashad 2016].

2.3.0.4 Attapulgite and Sepiolite

Palygorskite is the mineralogical term for this substance, although attapulgite has been used as a common name in much of the health effects literature. The term sepiolite derives from the Greek word "cuttlefish" because the compact shape of this clay recalls the porous and light inner shell of this mollusc [Berre 1989].

The structure of palygorskite and sepiolite contains open channels, and these give it some unique properties, particularly in the sorption of various materials (Fig. 2.7a). Small polar molecules interact at the inner surface of these channels and non-polar organic molecules are adsorbed onto the large external surface area [IARC 1997].

The structure of these minerals can be considered to contain ribbons of a 2:1 phyllosilicate structure, each ribbon being linked to the next by inversion of SiO_4 tetrahedra along a set of Si-O-Si bonds (Fig. 2.7b). Palygorskite and sepiolite are complex magnesium silicates with an open-channel structure forming elongated crystals, which can be present as partial

isomorphic substitutions of magnesium by aluminum or iron, characterizing as a ripiform crystalline structure, similar to amphiboles [Luz and Almeida 2005]. These substitutions of magnesium in the octahedral layers of clay minerals result in an excess of negative charges. These, associated with specific high surfaces, make the attapulgite and sepiolite sorbents for some polar molecules or positive ions. In addition, attapulgite elongated morphology differs from sepiolite only in minor respects mainly regarding the width of ribbons (Fig. 2.7b).

The general formulas of these minerals are [Berre 1989]:

Palygorskite – $Si_8Mg_5O_{20}(OH)_2(OH_2)_4, 4H_2O$

Sepiolite – $Si_{12}Mg_8O_{30}(OH)_4(OH_2)_4, 8H_2O$;

The palygorskite-sepiolite group of clay minerals has a wide range of industrial applications derived mainly from its sorptive, rheological and catalytic properties which are based on the fabric, surface area, porosity, crystal morphology, structure and composition of these minerals [Galan 1996]. It is also used as oil well drilling fluids, adhesives, liquid suspension fertilizers, emulsion paints, floor absorbent, cat litter, carrier for agricultural chemicals, pharmaceutical and catalysts [Haden Jr 1963].

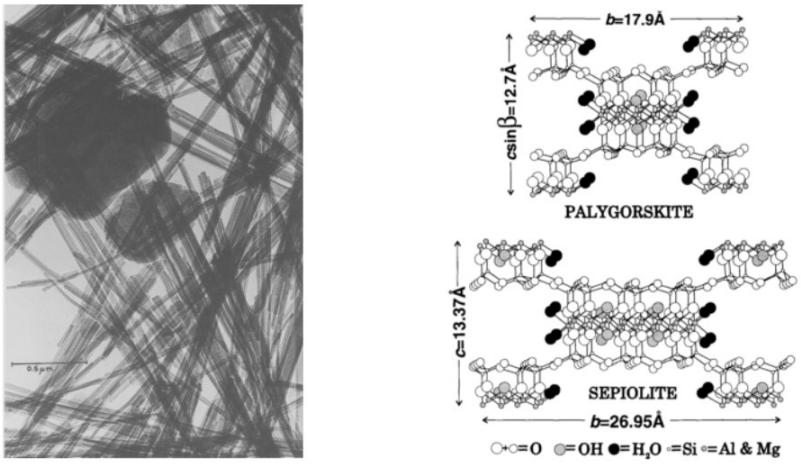

(a) (b)

Figure 2.7: (a) Transmission electron microscopy image of fibrous palygorskite (b) Schematic structure of palygorskite [Galan 1996].

2.3.0.5 Kaolinite

The word kaolin is derived from the Chinese word Kauling which means high ridge. The mine at Kauling, Kinagsi Province, was in operation from 11th century until 1964 [Giese 1988]. Commercially, kaolins have kaolinite as the dominant mineral and occurs in several countries of the world. Kaolinite is formed as a weathering product, by hydrothermal alteration, and as a authigenic sedimentary mineral [Murray 1988].

Kaolinite ($Al_2Si_2O_5(OH_4)$) has a layer of composition $(Si_4O_{10})_4$ which is formed by the linkage of SiO_4 tetrahedron in a hexagonal array, the bases of tetrahedron being approximately coplanar and their vertices all pointing in one direction. The apical oxygens, together with some additional OH- ions located over the centers of hexagons, form the base of a layer of composition $(OH)_6 - Al_4 - (OH)_2O_4$ (Fig. 2.8). The alternative sets of two Alvi sites when a second layer is superimposed produces different structures. This results in minerals chemically identical but have their layers stacked in different regular sequences, forming the kaolinite mineral group (kaolinite, dickite and nacrite) [Deer *et al.* 1992].

That structural array composed of one SiO_4 tetrahedral sheet linked to an octahedral sheet allows classified as 1:1 type layer silicates. Because of this arrangement, the positive charge of the H+ ions in the OH layer exerts a strong attraction for the negative oxygens of the neighboring sheets. In this way, the platelets of kaolinite are tightly bound together. Kaolinite is non-expanding mineral; hence, it is unable to absorb water into the interlayer position. The members of the kaolinite group show a nearly uniform chemistry: SiO_2 = 46.54wt%, Al_2O_3 = 39.50 wt%, H_2O = 13.98 wt%, corresponding to $Al_2Si_2O_5(OH)_4$. Small quantities of Fe, Ti, K and Mg, normally are found also. The presence of ancillary minerals in small quantities is to be expected, and sometimes these can be identified in X ray diffraction patterns. Bulk chemical or other analytical methods are of little use because it is not possible to eliminate the contamination problem [Giese 1988].

When the kaolinite minerals are heated so that all water molecules and OH- ions are driven off (about 650°C for the majority of specimens and is complete by 800°C for all), the products are called meta-kaolinite. When kaolinite minerals are heated beyond 800°C their layered structures are further disrupted and cannot be reconstituted by re-hydration. The final products of decomposition are mullite and crystobalite, with a defect spinel phase occurring at an intermediate stage [Deer *et al.* 1992].

Aras [2004] determined phase transformation sequence of mixture of the kaolinite-illite clays

and compared them with those individual pure clays. After the dehydroxylation, metakaolinite and illite/sericite anhydride structures are formed with the change from kaolinite to metakaolinite. The residual kaolinite peaks disappears at 550°C, leaving only quartz and a 4.48 Å peak representing kaolinite or illite anhydride. Metakolinite decomposes into spinel and amorphous phase by firing to 950°C. The reaction between the two phases produces mullite at 1150°C. The resulting SiO_2 crystallizes to cristobalite. Illite/sericite anhydride becomes progressively less crystalline and disappears at 1000°C . The stability areas and eutectic melt point are very different for Ca-containing system (Ca feldspar) and K-containing system (K feldspar), where K feldspar has a lower eutectic melt point.

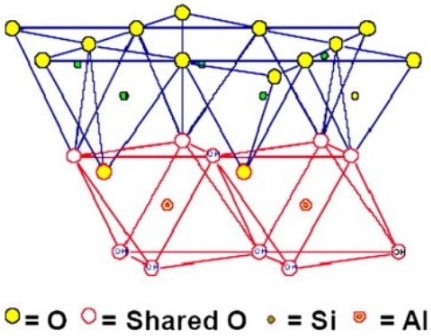

Figure 2.8: The crystalline structure of kaolinite.

2.3.0.6 Diatomite

Diatomite is a siliceous sedimentary rock formed in the tertiary and quaternary periods, consisting mainly of fossilized diatomaceous algae (liatomen and radiolaria) skeleton fragments. Diatom consists of a wide variety of shape and size (10-200 mm) in a structure containing up to 80-90% voids [Lemons 1997]. They are shells formed by hydrated silica, opal, with variable water contents ($SiO_2.nH_2O$). The rock matrix is still constituted by quartz, clays, carbonates, oxides and organic matter. Commercially exploited deposits are recent, starting from the Miocene, from marine or lake environments.

The industrial applications of diatomite result from its highly porous structure, low density and high surface area. These characteristics gives properties such as hydrophobicity, ion exchange capacity and adsorption. These properties are governed by the presence of water in the form of OH-active groups (silanol) bound to the Si-O (siloxane) groups. At room temperature, both of the isolates and H-bonded silanols associate with the physically adsorbed

water by hydrogen bond. After calcination treatment, physically adsorbed water will be desorbed from the silanols, and the silanols will condense with the increase of temperature. Generally, the H-bonded silanols condense more easily than the isolated ones. With increase of temperature of 200 - 1000°C, there is continuous desorption of water and the exposure of more and more silanols. At 1000°C, the amount of isolated silanols reached the maximum, but some weakly H-bonded silanols remain on the surface [Yuan *et al.* 2004].

Ibrahim and Selim [2012] have demonstrated through the experimental heat treatment of natural diatomite from Kom Osheem deposit, Egypt, that at the temperature range 100-200°C, the diatomite releases absorbed water through the endothermic reaction. At temperature range 250-600°C, another endothermic reaction was recorded, due to the release of the combined water of the clay mineral. An intense endothermic peak at the temperature range 600 to 750°C due to calcite mineral breaks to wollastonite. At 900-1200°C occurs the complete dehydration of diatomite structure and formation of a new silica material, varying from cristoballite to complete amorphous material.

The SEM images of the sample heated at 900°C for 3 hours showed maximum openings of the diatomite porous structure (Fig. 2.10a). This effect is similar to calcination operations. However, increasing the firing soaking time to 5 hours at 900°C, the diatomite structure begins to collapse (Fig. 2.10b). By increasing the temperature to 1000°C for 5 hours, complete dehydration of diatomite structure occurred which is accompanied by total collapsing and destruction of the porous structure (Fig. 2.10c).

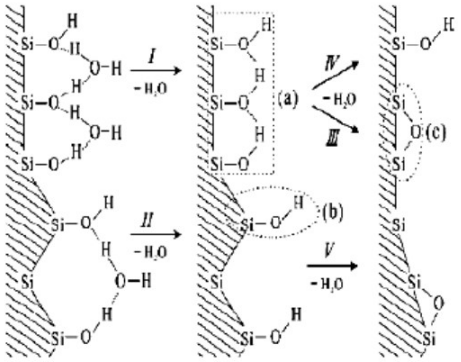

Figure 2.9: The hydroxyl structure and the dehydration of diatomaceous silica (a) H-bounded silanols, (b) isolated silanols and (c) siloxane [Yuan *et al.* 2004].

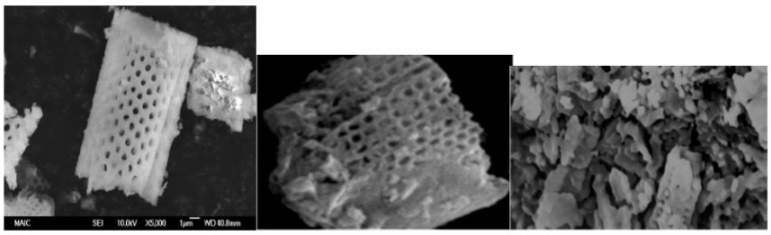

Figure 2.10: SEM images showing the diatomite structures: (a) at 900°C for 3 hours with clean opened pores, (b) at 900°C for 5 hours, smoother surface and collapsing of porous structure; (c) at 1000°C for 5 hours, the complete destroying of diatomite porous structure [Ibrahim and Selim 2012].

2.3.0.7 Zeolite

Zeolite is among the most effective adsorbent for the adsorption process because it has a high surface area and excellent sorption capacity and it is inexpensive [Alver and Metin 2012].

Its structure is highly porous and composed of hydrated alumina silicate having three dimensional crystal structures. The chemical formula is $Me_2/xO.Al_2O_3.mSiO_2.nH_2O$ (Me: metal ion).

Zeolites have a rigid, 3-dimensional crystalline structure, similar to a honeycomb, allowing water to move freely in and out of the pores [Lenntech 2017].

The industrial applications are wide for instance adsorption and removal of volatile organic compounds emitted from printing, painting and other facilities, removal of impurities of air, drying of pharmaceuticals and precision instruments and many others [Tosoh 2017].

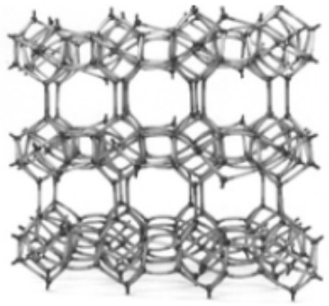

Figure 2.11: Crystalline structure of zeolite [Lenntech 2017].

2.4 Preparation steps

The elaboration of the ceramic body was performed mixing different proportions of additives to clay (5, 10 and 20%wt) and water was added to confer a good plasticity (workability) depending on the used amount of additives (Fig. 2.12). Samples were place in a silicon mold of 60mm X 20mm X 10mm (Fig. 2.13) and stayed for 48h at room temperature to naturally dry. They were additionally dried at 105°C for 24h and then sintered in a furnace (Fig. 2.14) at three different temperatures (800°C, 900°C and 1000°C) for 1h with a heat rate of 10°C/min to approach the actual commercial clay-based products (Fig. 2.15).



Figure 2.12: Preparation of the mix of raw materials and clay.

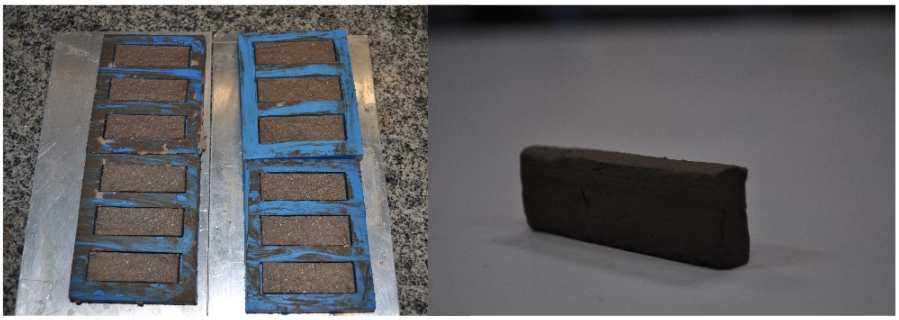

Figure 2.13: Preparation of samples using silicon mold



Figure 2.14: Samples in the furnace.

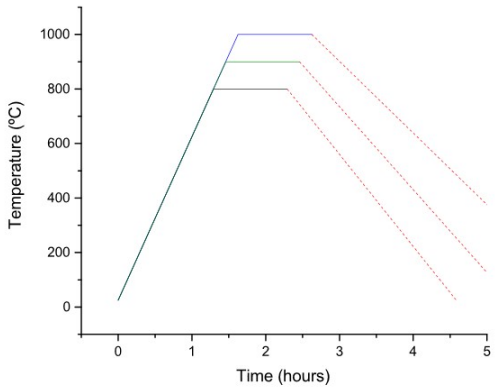

Figure 2.15: (a) Sintering cycle.

2.5 Physical characterization

The influence of mixing ratio (% of absorbents in clay) in mechanical and physical properties was tested using vermiculite and perlite. Their operational sintering temperature, physical and mechanical properties were studied.

Ceramics bodies were characterized according to technical standards for water absorption, total shrinkage, loss of ignition porosity and density. All the tests were carried out on 6 samples for each formula.

Bulk density (ρ), water absorption (WA) and open porosity (OP) for samples were determined in accordance with ASTM C 373-14. Six fired clays per composition were dried to constant

mass, m_{dry}, and placed in a water tank at room temperature. After 24 h, samples were completely immersed in the boiling water for 5h. Using the Archimedes principle, samples were suspended in the water with a wire lop that is suspended from one arm of the balance and mass of each specimen was determined, m_{sus}. After determination of suspended mass, m_{sus}, all visible water on the surface was removed from each specimen and then weighed again which gives the saturated mass, m_{sat}. Weight determination was performed immediately after the blotting process to avoid errors due to evaporation of water from the test specimen. Bulk density (ρ), water absorption (WA) and open porosity (OP) were then determined using the following equations:

$$\rho = \frac{m_{dry}}{m_{sat} - m_{sus}} * \rho_w \tag{24}$$

$$WA(\%) = \frac{m_{sat} - m_{dry}}{m_{dry}} * 100 \tag{25}$$

$$OP(\%) = \frac{m_{sat} - m_{dry}}{m_{sat} - m_{sus}} * 100 \tag{26}$$

where: ρ_w is the water density, in kg/m^3.

Total shrinkage (SH) values were obtained by measuring the length of the samples with a caliper before (L_b) and after (L_a) the firing stage in accordance to standard ASTM C210-95 and using Eq.27:

$$SH(\%) = \frac{L_b - L_a}{L_a} * 100 \tag{27}$$

Loss of ignition (LI) represents the loss of matter during firing process and was determined by measuring the mass loss of the sample between the drying at 105°C (m_d) and firing stage

(m_a) following Eq.28:

$$LI(\%) = \frac{m_d - m_a}{m_d} * 100 \tag{28}$$

2.6 Mechanical properties

The bending strength of the fired samples was determined by three-point bending in a mechanical testing machine with a load cell of 1000N until failure at Fmax (N). Loading was applied to rectangular ceramic samples of 60mm X 20mm X 10mm at a constant rate of 0.5mm/min. Six samples were used for each composition. Bending stress (σ) and elasticity modulus (e) were directly obtained by a software.

2.7 Results

2.7.1 Physical properties

Several physical properties of these porous clay bricks were determined: linear shrinkage, loss on ignition, density, water absorption and porosity. Once the samples had been prepared using the protocols described above, the impact of the added absorbent on different properties of fired clay bricks was studied as well as sintering temperature.

Firing linear shrinkage (before and after firing) are expressed as a percentage and calculated according Eq. 27 for different percentage of incorporated perlite and vermiculite and for three sintering temperatures as illustrated in Fig. 2.16. During firing, especially during sintering at high temperatures, ceramic particles fuse together leading to greater proximity and thus enhancing linear shrinkage [Martínez *et al.* 2012]. From Fig. 2.16, it can be seen that absorbent agents give positive shrinkage, representing water evaporating out of the system. Bricks must have a firing linear shrinkage lower than 8% in order to retain good mechanical performance [Weng *et al.* 2003; Kornmann 2009] as a large contraction could cause tension and breakage [Mekki *et al.* 2008]. In Fig. 2.16, shrinkage clearly depends on the absorbent used and its percentage incorporated, so no real comparison can be made between them. However, it can be seen that for both perlite and vermiculite incorporation, linear shrinkages are below 8%. In addition, the lower this result, the better the final product's properties.

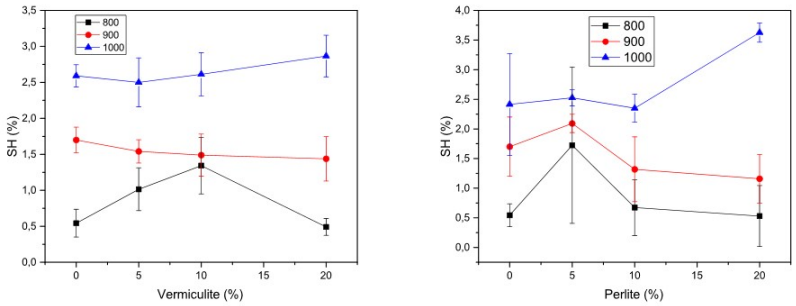

(a) (b)

Figure 2.16: Firing linear shrinkage in function of the percentage of additives in clay and firing temperature. Addition of: (a) vermiculite (b) perlite.

The linear retraction of all compositions with same percentage of additives (20%) at 800°C and 1000°C is shown in Fig. 2.17. It can be seen that as observed for CVER and CPER samples previously, sintering temperature also increases the loss of ignition for all compositions remaining lower than 8%. However, clayey materials behave differently according firing temperature. Considering average, linear shrinkage, montmorillonite, diatomite, sepiolite ultra-fine and sepiolite sand addition rise linear shrinkage of clay. At 1000°C, almost all compositions enhance clay SH-value except from CATT and CMMT. CPER was the most affected composition by the elevation of firing temperature showing an increase of 1450% in the value of linear shrinkage.

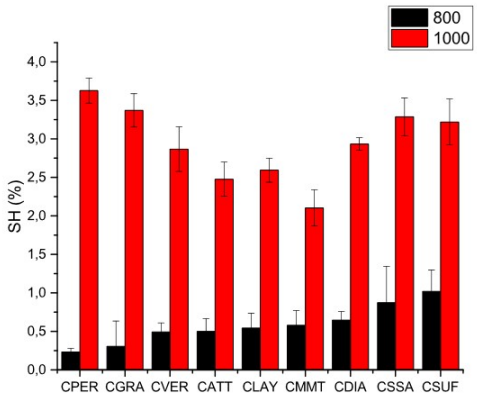

Figure 2.17: Firing linear shrinkage in function of the additives (20%) and firing temperature.

Loss on ignition was determined using Eq. 28 and a comparison of the percentage of incorporated absorbents and sintering temperature are illustrated in Fig. 2.18. Weight loss on ignition increases with sintering temperature. However, lower sintering temperatures, decreases densification of the material that could affect compression properties of the fired products and so weaken the structure [Lin 2007]. Thus, in order to retain good performance, weight loss on ignition should remain below 15% [Weng *et al.* 2003]. The absorbents described in Fig. 2.18 give a loss on ignition lower than this value. Comparing the quantities of incorporated matter, vermiculite and perlite exhibit a different behavior confirming the statement of Bories *et al.* [2014] that depending on the characteristics of the additives (chemical, composition, density), the results are completely different. Increasing the quantity of vermiculite incorporated to clay, also increases the loss of ignition (Fig. 2.18a), on the other hand, adding perlite decreases the LI-value (Fig. 2.18b).

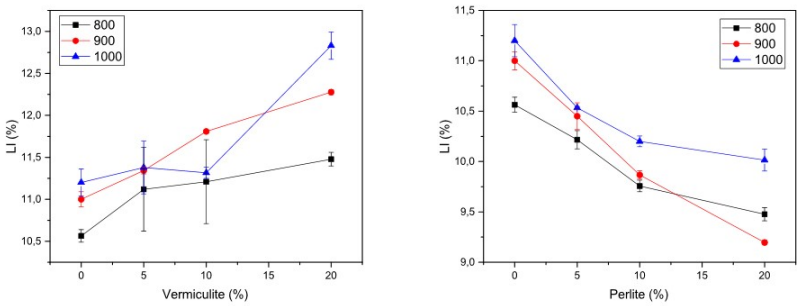

(a) (b)

Figure 2.18: Loss on ignition in function of the percentage of additives in clay and firing temperature. Addition of: (a) vermiculite (b) perlite.

Figure 2.19 compares all compositions with same percentage of additives (20%) at two firing temperatures. It can be seen that as observed for CVER and CPER samples previously, sintering temperature also increases the loss of ignition for all compositions remaining lower than 15%. As for perlite addition to clay, attapulgite, diatomite and montmorillonite diminished the mass loss of clay. Antagonistically, adding vermiculite and sepiolite (in all grain sizes: ultra-fine, sand and gravel) to clay enhanced its mass loss mainly for the sepiolite gravel incorporation which is the composition with bigger grain size.

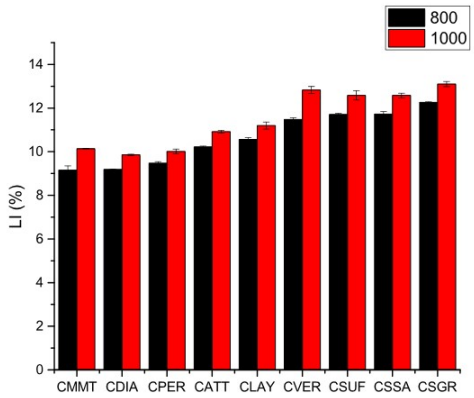

Figure 2.19: Loss on ignition in function of the additives (20%) in clay and firing temperature.

Apparent porosity of fired clay samples was measured using Archimedes' method described by Eq. 26. The apparent porosity of the system increases with the percentage of incorporated absorbents. Indeed, during drying and firing, the added particles burn leaving voids due to their breakdown, but also to gas emissions by decomposition of the matter (water, carbon dioxide). From Fig 2.20, all the samples tested have an apparent porosity of between 14 and 45%. Also, increasing firing temperature decreases the apparent porosity due to the beginning of vitrification in the clayey structure reducing the connection between pores in the flakes [Cultrone *et al.* 2005]. Therefore, as porosity is closely linked to the mechanical properties, increasing the percentage of incorporated absorbents produce more fragile materials that could be compensated by a higher firing temperature.

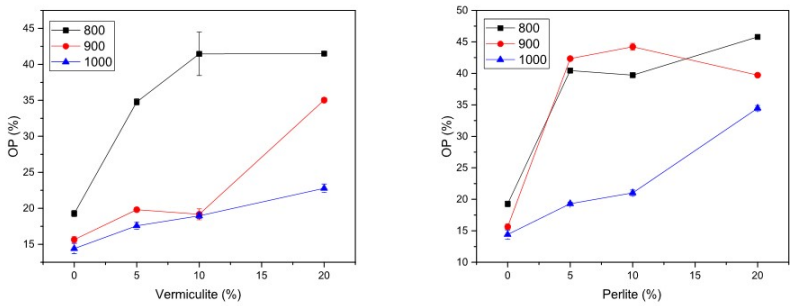

(a) (b)

Figure 2.20: Open porosity in function of the percentage of additives in clay and firing temperature. Addition of: (a) vermiculite (b) perlite.

Figure 2.21 shows that all absorbents increased the porosity of clay and that sintering temperature decreased open porosity as previously explained. The composition with diatomite improved the most the clay OP-value and CPER the least. Comparison illustrates, the bigger the sepiolite grain size, the higher the open porosity, for both sintering temperatures.

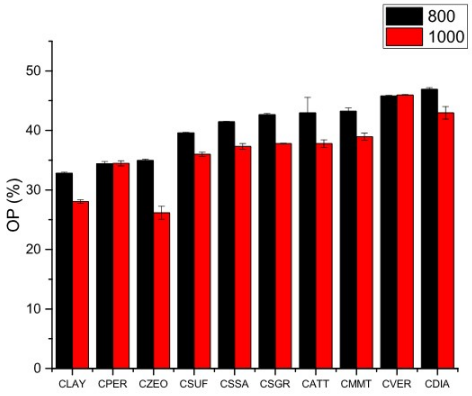

Figure 2.21: Open porosity in function of the additives (20%) in clay and firing temperature.

Water absorption of these bricks was determined using Eq. 25. The water absorption of the fired samples containing perlite and vermiculite is shown in Fig. 2.22. The creation of

porosity due to the incorporation of additives in the fired clay brick leads to an increase in water absorption. The voids in the structure while immersed, are filled with water and, depending on the arrangement of the pores and the way they are linked together, this can penetrate the material more or less easily, with a preferential pathway. Comparing these results with above, samples with a high water absorption capacity are also characterized by high porosity. These two properties are closely related, and the same profile was observed for porosity and water absorption in the samples tested by Saiah *et al.* [2010].

For water absorption, no standardized maximum value exists. However, a very large absorption capacity could be detrimental for the final brick as it may affect the durability of the product and its resistance to natural conditions [Pérez-Villarejo *et al.* 2012].

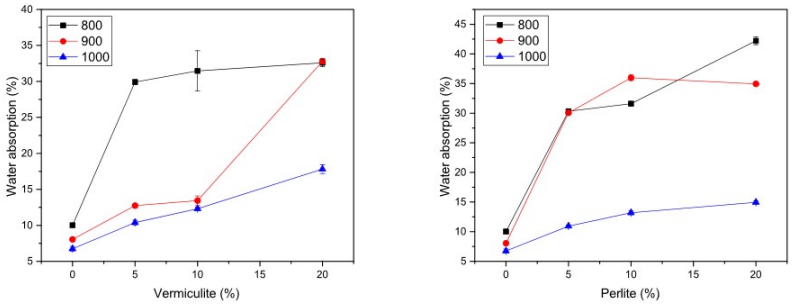

(a) (b)

Figure 2.22: Water absorption in function of the percentage of additives in clay and firing temperature. Addition of: (a) vermiculite (b) perlite.

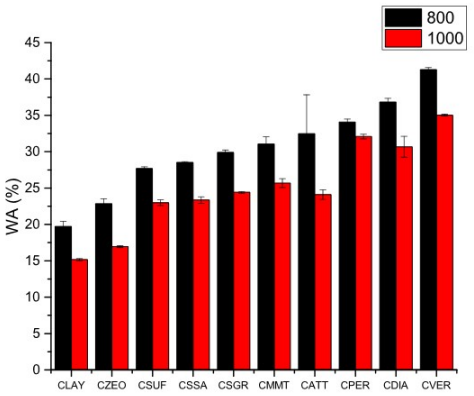

Figure 2.23: Water absorption in function of the additives (20%) in clay and firing temperature.

Bulk densities of compositions are given by Eq. 24. Adding absorbents into the clay mixture, that burn and break down during the manufacturing process, decreases the density of the material, as shown in Fig. 2.24. For the tested samples, there is an increase in bulk density with sintering temperature as expected due to densification process. At 800°C, the bulk density of samples with vermiculite significantly decreased from 1732.25 kg/m^3 to 958.56 kg/m^3 as the amount of expanded vermiculite increased from 0 to 20%. It is may due to the lower vermiculite unit weight and its microstructure composed of layered and expanded particles [Sutcu 2015]. For the samples with perlite addition, bulk density decreased from 1732.25 kg/m^3 to 1067.31 kg/m^3 at 800°C due also to the lower perlite unit weight .

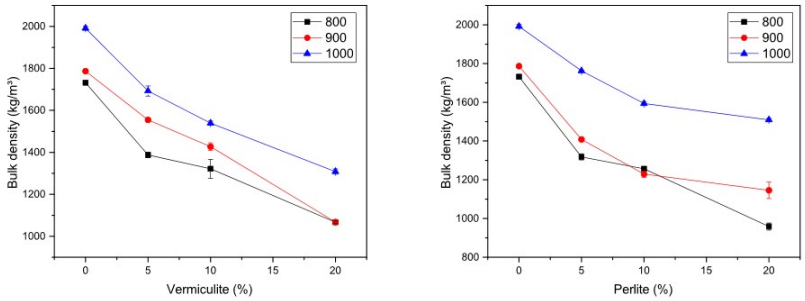

(a) (b)

Figure 2.24: Bulk density in function of the percentage of additives in clay and firing temperature. Addition of: (a) vermiculite (b) perlite.

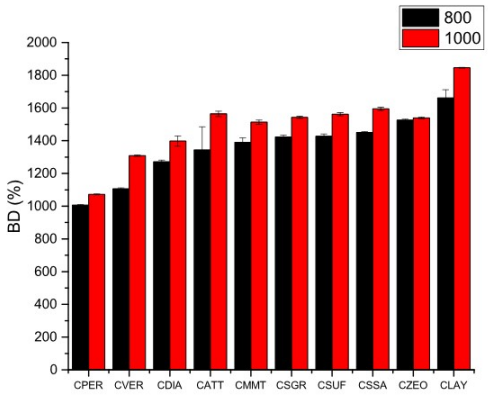

Figure 2.25: Bulk density in function of the additives (20%) in clay and firing temperature.

2.7.2 Mechanical properties

Mechanical properties are linked to pore structure of materials and consequently to sintering temperature. Flexural strength is a very important mechanical property concerning clay-based materials for instance clay tiles and it was measured by the three point bending test. Fig.2.26 shows the mechanical behavior of fired samples. Clay bending strength decreases when

vermiculite is added to its composition for all sintering temperatures tested (Fig.2.26a). The same trend is observed for perlite addition to clay (Fig.2.26b). However, when it comes to firing temperature, the relation is not so clear. As explained previously, the decrease in density of the material, the creation of porosity has important consequences concerning the products mechanical resistance. The samples with the flexural strength (Fig.2.26), and so the lowest resistance (addition of 20% of perlite or vermiculite to clay) also have a low density and the mechanical properties of excessively lightweight products decreased sharply. Therefore, compromises must be found between weight loss and resistance in order to avoid the production of fragile materials.

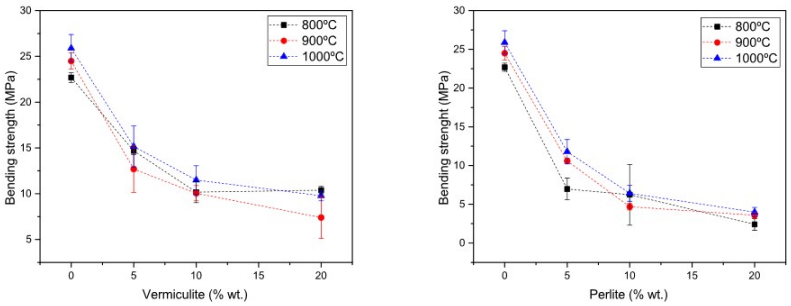

(a) (b)

Figure 2.26: Bending strength in function of the percentage of additives in clay and firing temperature. Addition of: (a) vermiculite (b) perlite.

2.8 Conclusions

In this study, the usable of absorbents from natural raw material sources in the fired clay production was investigated. Clay-based materials samples containing expanded vermiculite and perlite powder with different percentages were prepared to investigate the influence of absorbents proportion on fired clay. Three different firing temperatures were also tested. Physical and mechanical properties indicated the best proportion and this value was used for other additives on clay. The new compositions with sepiolite, diatomite, montmorillonite and zeolite were also physically characterized, allowing the following conclusions:

I. The bulk density of fired clay decreased with increasing vermiculite/perlite additive, while

their porosity and water absorption values increased. Sepiolite, diatomite, montmorillonite and zeolite addition also showed same behavior.

II. Bending strength values diminished with increasing vermiculite/perlite additive proportion on clay.

III. Increasing of the firing temperature affected the properties of the clay-based materials, which increased their mechanical strength, besides decreased their porosities.

IV. Temperature of 800°C presented the higher values of porosity as well as 20% wt of absorbents on clay. Firing temperature of 1000°C exhibited the best values of mechanical properties. Therefore, both temperatures (800°C and 1000°C) and absorbent proportion (20%) were chosen to be deeply investigated on the next chapters of microstructure and hygrothermal characterization.

Chapter 3

Microstructural characterization of fired clay-based ceramic composites

In order to understand the influence of the microstructure on hygrothermal properties of the produced materials, three samples that are characterized in Chapter 4 are selected: the composition with attapulgite that presents very good hygrothermal and physical properties, the sample with perlite which does not excel in hygric tests and the original clay material.
Although this chapter was made after the next one, we decided to put it before to better explain hygrothermal results based on material microstructure. First, materials were characterized by optical and scanning electronic microscopy, and x-ray diffraction. These techniques allow the phase identification of materials and provide a general panorama of sample microstructure. Afterwards, a quantification of geometric parameters of sample microstructure is performed with the help of a software. Lastly, results provide an enlightenment about the influence of material microstructure as well as the sintering temperature on hygrothermal properties.

Contents

3.1 Introduction **71**

3.2 Sample characterization techniques **72**

3.2.1 Pore size distribution 72

3.2.2 Optical microscopy 73

3.2.3 Scanning electron microscopy (SEM) 73

3.2.4 X-ray diffraction (XRD) 73

3.3 Results and discussion **74**

3.3.1 Phase identification and high temperature behavior 74

3.3.2 Microstructure morphology 78

3.3.3 Microstructural evaluation 85

3.3.4 Morphology of pores 91

3.3.5 Pore quantification 96

3.3.6 Mechanical properties 99

3.4 Conclusions **100**

3.1 Introduction

Last chapter has pointed the influence of firing temperature on physical and mechanical properties. Some authors analyzed pore size distribution of natural [Diamond 1970; Kuila and Prasad 2013] and fired clays [Maage 1984; O'Farrell *et al.* 2001] but few studies correlated firing temperature, microstructure and pore size distribution in fired clays [Goktas *et al.* 1997; Eliche-Quesada *et al.* 2017].

To fill this gap and considering that textural and pore size characteristics are associated to firing temperature, this chapter investigates the influence of composition and firing temperature on the microstructural evolution of three clay-based materials and links the referred properties with pore size distribution. An attempt to correlate mechanical properties and microstructure of selected materials has also been presented.

The size and the distribution of pores in a material are very important information to understand their hygric behavior since moisture storage and transfer occur in pores affecting their moisture buffer capacity. To find out whether pore size distribution affects microstructural properties with firing temperature, a detailed microstructural characterization of clay-based materials has been performed.

Results from an experimental campaign that includes elemental and phase composition, microstructure morphology at micro and nanoscales and pore distribution quantification are presented. For this purpose, nitrogen adsorption technique based on the Brunauer−Emmett−Teller (BET) theory [Brunauer *et al.* 1938] is very useful to access pore information but it is limited to small pores. In order to have more accurate data of larger pores, the mercury intrusion porosimetry (MIP) technique is also used. It is an analogous process with N_2 adsorption but it uses mercury as the pore filler instead of nitrogen. However, the MIP method tend to overestimates the volume of the smallest pores due to the ink-bottle shaped pores which means that large pores with small openings are identified as small diameter making the BET method more appropriate to measure small pores. Therefore, a combination of MIP and N_2 gas adsorption can provide information for the entire pore-size range. Typically, the pore diameter determination range of high-pressure mercury porosimetry is 10 nm−300μm and nitrogen adsorption is 1−100 nm [Rodts 2001]. Elemental composition was given by energy-dispersive X-ray spectroscopy (EDS) (Appendix A). Nevertheless, a ceramic material is not only governed by its chemical composition, but also by its crystalline structure. For instance, two ceramics with an identical composition but a different crystal structure may behave very differently

[Valette 2015]. Thus, X-ray diffraction (XRD) aided to characterize phase composition. Morphology from a scale of micrometers was obtained with optical microscopy (OM) and analyzed with the software Quantikov [Pinto 1996]. In addition, structures from nanometers were illustrated with the images from scanning electron microscopy (SEM).

3.2 Sample characterization techniques

This chapter focus on the microstructural study of three selected samples: the composition with attapulgite that presented very good hygrothermal and physical properties, the sample with perlite which did not excelled in hygric test and the clay base material (Chapter 4). All samples were analyzed at two different sintering temperatures: 800°C and 1000°C. Different techniques were performed with a view to access and compare the microstructure of three selected composition. Nitrogen adsorption and mercury intrusion porosimetry techniques (section: 3.2.1) provides pore size distribution information of materials. A general panorama of samples microstructure is given by optical microscopy (section: 3.2.2) and pores and nanostructures are illustrated by images from scanning electronic microscopy (section: 3.2.3). Finally, elements and phase composition are identified by X-ray spectroscopy (section: 3.2.3) and X-ray diffraction (section: 3.2.4) respectively.

3.2.1 Pore size distribution

Brunauer-–Emmett–Teller (BET) theory [Brunauer *et al.* 1938] aims to interpret the physical adsorption of gas molecules on a solid surface and is a base of experimental techniques that measure the specific surface area of a material that has a particular importance for adsorption and pore size analysis. The NOVA 2000e, Quantachrome from Ecomateriales laboratory at UANL (Universidad Autónoma Nuevo León, Mexico), is a surface area analyzer equipment that was used to obtain pore size distribution of samples using the BET theory. Nitrogen was the gas used as adsorbate since it does not react chemically with the material surface allowing the quantification of surface area and pore size.

Mercury intrusion porosimetry (MIP) from École des Mines d'Alès in France was used to access larger pores that BET technique cannot measure. Therefore, MIP combined with nitrogen adsorption provided the complete range of pore size distribution as well as pore shape and pore surface area.

Besides of pore size distribution, BET theory allows the calculation of materials specific surface. Sorption isotherms measurements made by the NOVA 2000e, Quantachrome (Ecomateriales Laboratory at UANL) provide data to these calculations detailed in appendix B.

3.2.2 Optical microscopy

Samples were prepared as polished thin sections and optical microscopy observations were conducted using a polarized microscope (Leica 4500) with a image capture system from Fluid Inclusions and Metallogenesis Laboratory at CDTN (Centro de Desenvolvimento da Tecnologia Nuclear). The main textural features observed in the optical microscopy were analyzed and measured using the software Quantikov. It provides the following microstructural parameters: the area, the perimeter, the length, the diameter, roundness and a statistic distribution of the grain size and phases in the microstructure of the material [Pinto 1996].

3.2.3 Scanning electron microscopy (SEM)

The polished thin sections were gold coated in the Quorum Q150R ES rotary-pumped coating system and the microstructure of the clay-based materials are analyzed by scanning electron microscope (Vega3, Tescan) from Materials Technology and Manufacturing Processes Laboratory at PUCPR, equipped with an energy dispersive X-ray spectroscope (EDS). The images were obtained using secondary electron (SE) detector, operated at a 10.0 kV accelerating voltage for morphology visualization.

3.2.4 X-ray diffraction (XRD)

The microstructural study was complemented by X-ray diffraction (XRD) analyses using a Rigaku D/MAX Ultima diffractometer from CDTN (Centro de Desenvolvimento da Tecnologia Nuclear, Brazil). The samples were analyzed as powders after a heat treatment at 800°C and 1000°C. Clay of the base material was dried and crushed. Absorbents (Attapulgite and Perlite) were also crushed and analyzed for initial composition identification, which enables the examination of absorbents influence when they are mixed to clay and sintered. Data were collected on a range of 2θ from 4° to 80° at a scan speed of $2\theta/min$, current intensity of 30mA and voltage of 40 kV and using a CuKα radiation source (λ=1.5405 Å). The identification of the mineral phases was carried out using Jade 0.9/MDI software and PDF2 database.

3.3 Results and discussion

3.3.1 Phase identification and high temperature behavior

The characterization of the phases was carried out initially through XRD, essential for the identification of the very fine phases, mainly the clayey type. However, quantification of the phases by this method was disregarded. Since the high intensities of the quartz and microcline peaks are related to the degree of crystallinity of these minerals when compared to the clay minerals, they can not be attributed to the proportion of these minerals.

The mineralogical composition of the clayey material consists predominantly of kaolinite, quartz, microcline and muscovite, characteristic of kaolinic clays. Figure 3.1 shows a comparison of the XRD spectra generated for the initial clay and the fired ceramic material at 800°C and 1000°C denoting a variation of the phases with the sintering temperature of the material. The kaolinite peaks disappear with the heating process. At 800°C the muscovite peaks increased slightly and may result from the transformation of part of the kaolinite. This aspect was also observed in optical microscopy, with formation of fine white mica in the clayey matrix. At 1000°C, the muscovite peaks disappeared, remaining only the peaks of the quartz and microcline.

In the ceramic material with the addition of attapulgite, the comparison of the diffraction results in the attapulgite pellets and the fired material at 800°C and 1000°C showed that the influence on the mineralogical composition is predominantly of the clay base material (Fig.3.2). The attapulgite pellets are essentially composed of: palygorskite, lizardite and muscovite/illite and quartz. At 800°C the palygorskite and lizardite peaks disappear, remaining only the muscovite, quartz and microcline. At 1000°C, only peaks of quartz and feldspar are observed, as in the base material.

The attapulgite granules were submitted to same firing conditions of the samples, crushed and the powder was analysed by XRD. Figure 3.2 shows the changes of mineralogical composition of attapulgite with the increase of temperature. When compared to the original material standard, at 800°C the pattern presents more noises, the peaks are less defined and there is a displacement of the base, indicating the beginning of amorphization of some phases. The remaining peaks coincide with quartz, muscovite and enstatite. At 1000°C, the enstatite peaks are more defined and the quartz peak remains. The general appearance of the diffractogram also suggests partial amorphization of the material.

Paligorskite is the main constituent mineral of attapulgite granules and its sorption and high natural porosity characteristics are dependent on the outer surface and the size of its molecular channels [VanScoyoc *et al.* 1979]. The morphological and structural characteristics of palygorskite [Frost *et al.* 2010], [Ruiz *et al.* 1996] and the variations that occurred during the heat treatment processes [Serna *et al.* 1977; VanScoyoc *et al.* 1979; Frini-Srasra and Srasra 2010] have been exhaustively studied. In this work, the palygorskite undergoes drastic structural variations during heating. At 120°C half of the coordinated water is lost and the structure folds during the removal of 50 to 65% of the structural water. The disappearance of palygorskite is consistent with structural variations occurring with the increasing of firing temperature, where dehydration and dehydroxylation is complete between 400 and 500°C, depending on the rate of heating [VanScoyoc *et al.* 1979]. The temperature to which these samples were submitted to is much higher than the one shown in all the experimental works. The transformation of palygorskite in other phases with the heating will release water and generate variation in the internal structure of the granules, which may facilitate the start of the melting, justifying the characteristics of the diffractograms, with lower a peak definition.

In the perlite-containing ceramic material, the influence of the additive can still be observed at 800°C, but at 1000°C, only quartz and feldspar remained in the base material. The perlite forms a broad peak with a maximum elevation of 2θ at 22°. At 800°C, the diffractogram shows background variation, coincident with the perlite curve. Muscovite, quartz and microcline peaks were also observed, as in the base material. At 1000°C, there is no more influence of perlite, nor as an amorphous material (Fig.3.3).

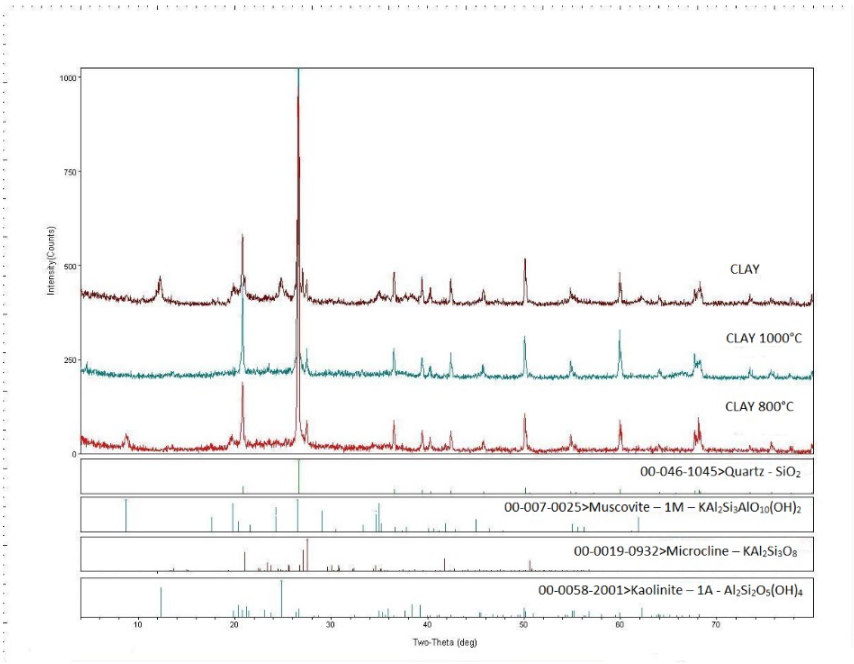

Figure 3.1: X-ray pattern to show the phase evolution of clay when firing temperature is increased.

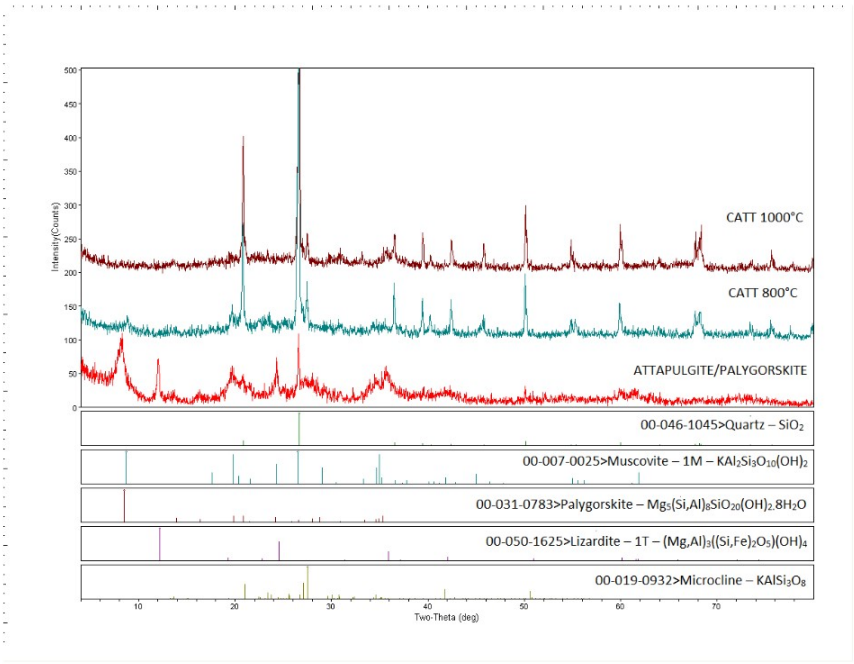

Figure 3.2: X-ray pattern when attapulgite is added to clay showing the phase evolution with the increasing of firing temperature.

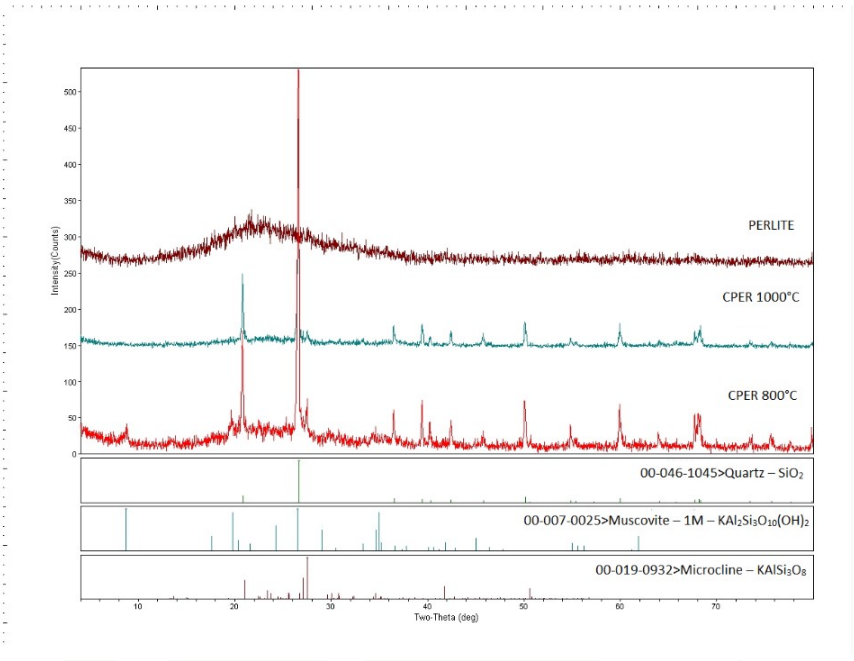

Figure 3.3: X-ray pattern when perlite is added to clay showing the phase evolution with the increasing of firing temperature.

3.3.2 Microstructure morphology

3.3.2.1 Clay

Figure 3.4 is a representative sample of the original clay material, without the additives. It is characterized by containing fragments of quartz crystals, feldspar and iron hydroxides, and to a lesser extent fragments of rocks, supported by a clayey matrix. The staining of the matrix varies from light beige to reddish, with the darker portions resulting from the presence of colloidal iron hydroxides.

In the sample fired to 800°C, the crystals of quartz and feldspar are distinguishable by optical microscopy. Two granulometric bands of fragments are observed: larger, between 500 and 1000μm, and small ones, smaller than 50μm (Fig.3.4a). It was also identified the presence of iron oxide and hydroxide crystals, occurring as subhedral crystals (Fig.3.4b). In the clay matrix, the presence of fine muscovite is highlighted, and may represent that part of the clay

recrystallized to mica with the increase of temperature (Fig.3.4c).

However, in the sample fired at 1000°C, the muscovite disappears, the matrix is darker with several types of rock fragments and minerals, in which shapes and sizes are similar to those found in the sample fired to 800°C (Fig.3.4d and Fig.3.4f). The fragments of quartz and feldspar are more difficult to distinguish through the optical properties, since the maclas disappear (Fig.3.4e).

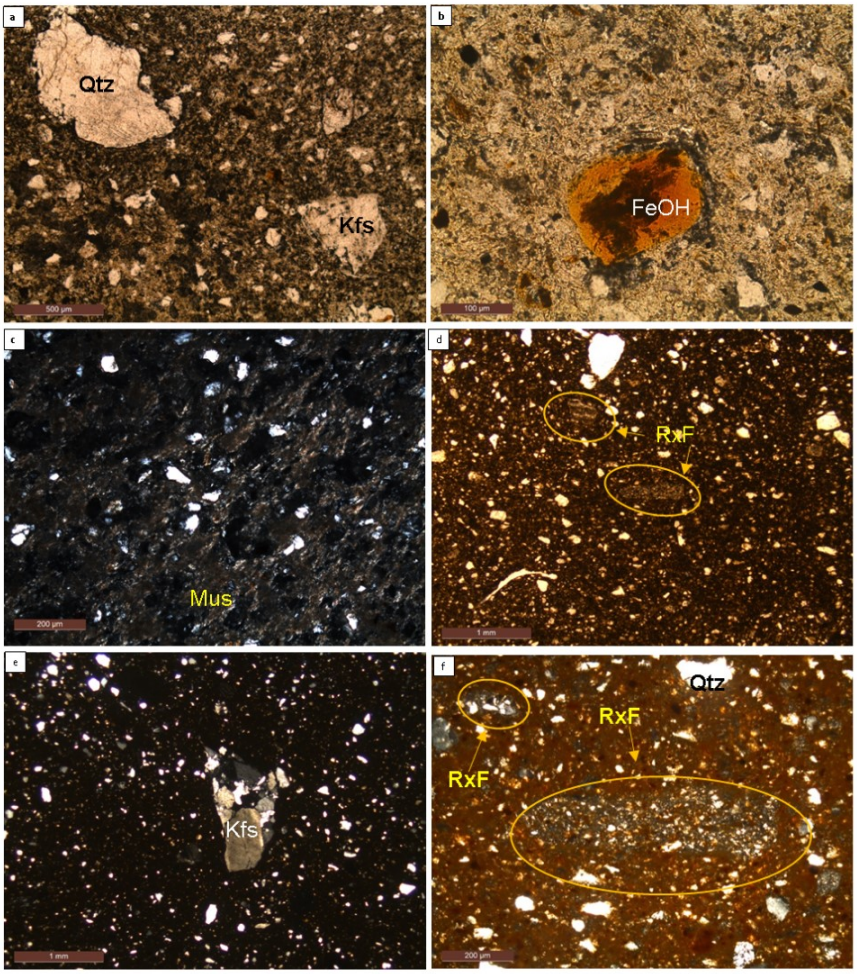

Figure 3.4: Photomicrographs of the clay samples without addition of absorbents showing the main characteristics of the clayey base material fired at 800°C: (a) larger fragments of quartz crystals (Qtz) and feldspar (Kfs) supported by a clay matrix with small crystals of quartz and feldspar. (b) detail of a larger iron hydroxide crystal (FeOH) and (c) polarized light showing the occurrence of small muscovite crystals near the clay matrix. Samples fired at 1000°C:(d) darker clay matrix with fragments of rock (RxF) and quartz agglomerates (natural light). (e) aggregate of feldspar crystals supported by the clay matrix (crossed nicols) and (f) detail of the rock fragments occurring in the clay matrix.

3.3.2.2 Clay with attapulgite (CATT)

In the samples in which attapulgite particles were added, a secondary porosity appeared around the fragments with the heating process. At 800°C, attalpulgite particles exhibit partial fusion features, with light, medium and dark portions. These structures may be rounded or irregular, but generally the central portions are the darkest. The lighter portions of the attapulgite particles still preserve the optical properties of the original material, however the darker portions become extinct, indicating fusion. Also, some particles are partially fractured, and the opening of these fractures also generate the secondary porosity (Fig.3.5a). In the clayey matrix there are still fine muscovite crystals, mainly observed with crossed nicols (Fig.3.5b). The corona secondary porosity, found around some attapulgite particles, may be complete, but it is generally narrow and does not occur in all grains (Fig.3.5c). It does not occur either around the remaining crystals or rock fragments of the clayey base material.

In the sample fired to 1000°C, it is observed that both the matrix and the attapulgite particles are darker, characterizing the burning of the material. The porosity coronas around the attapulgite particle are more abundant and thicker at this temperature (Figs.3.5d and 3.5g). This secondary porosity can be interconnected when there is a fracturing of attapulgite particles (Fig.3.5e). To a lesser extent, secondary porosity may form irregular channels in the matrix (Fig.3.5f).

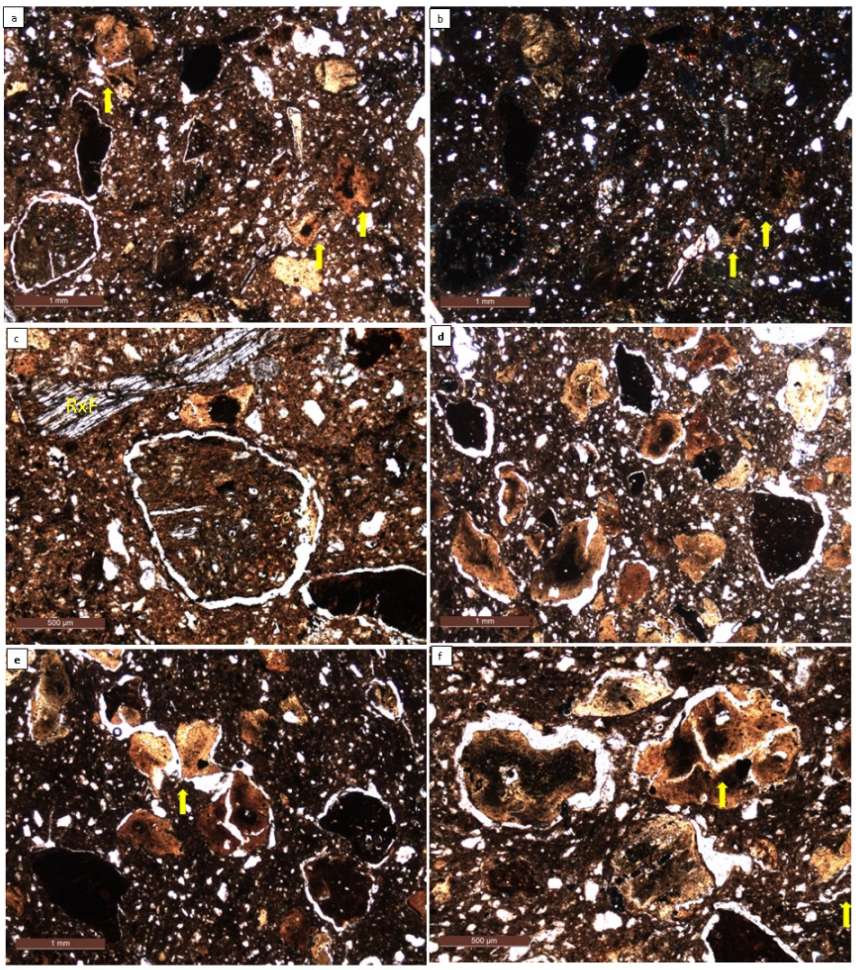

Figure 3.5: Photomicrographs of clay samples containing attapulgite particles fired at 800°C: (a) general characteristic of the sample showing the different behavior of the attapulgite particles with the heating, generation of a secondary porosity around some particles and the presence of fractures in the particles of attapulgite and particles with darker central portion indicating initiation of a fusion process (natural light). (b) same photomicrography as (a) with crossed nicols showing that the darker portions become extinct indicating the fusion, and in the matrix, the high birefringence of muscovite evidences its presence and (c) detail of the restrict corona-shape porosity formation in attapulgite particles. Samples fired at 1000°C: (d) higher ratio and width of the coronas in the attapulgite (e) attapulgite particle fractured and fragmented by secondary porosity and (f) detail of the thicker coronas and that the firing process generated the fracture and fragmentation of some attapulgite particles and formation of channels to a lesser extent.

3.3.2.3 Clay with perlite (CPER)

In the samples with addition of perlite, the main texture formed with the firing process is a secondary porosity in the form of channels, which tend to bind one particle to another. At 800°C, the perlite still preserves its internal structure, formed by rounded fractures (Fig.3.6a). There are small irregular channels forming that interconnect the perlite particles and the rock fragments and larger crystals of the base material (3.6b). These channels can be observed even in the cross section of the sample, indicating that it occurs in the 3 dimensions of the material (Fig.3.6c).

At 1000°C, the channels are more abundant and thick (Fig.3.6d), but there is a larger interaction with the rock fragments (Fig.3.6e) and the iron crystals / oxides / hydroxides (Fig.3.6f). Only in these crystals there is formation of secondary porosity in the form of coronas and, simultaneously, channels.

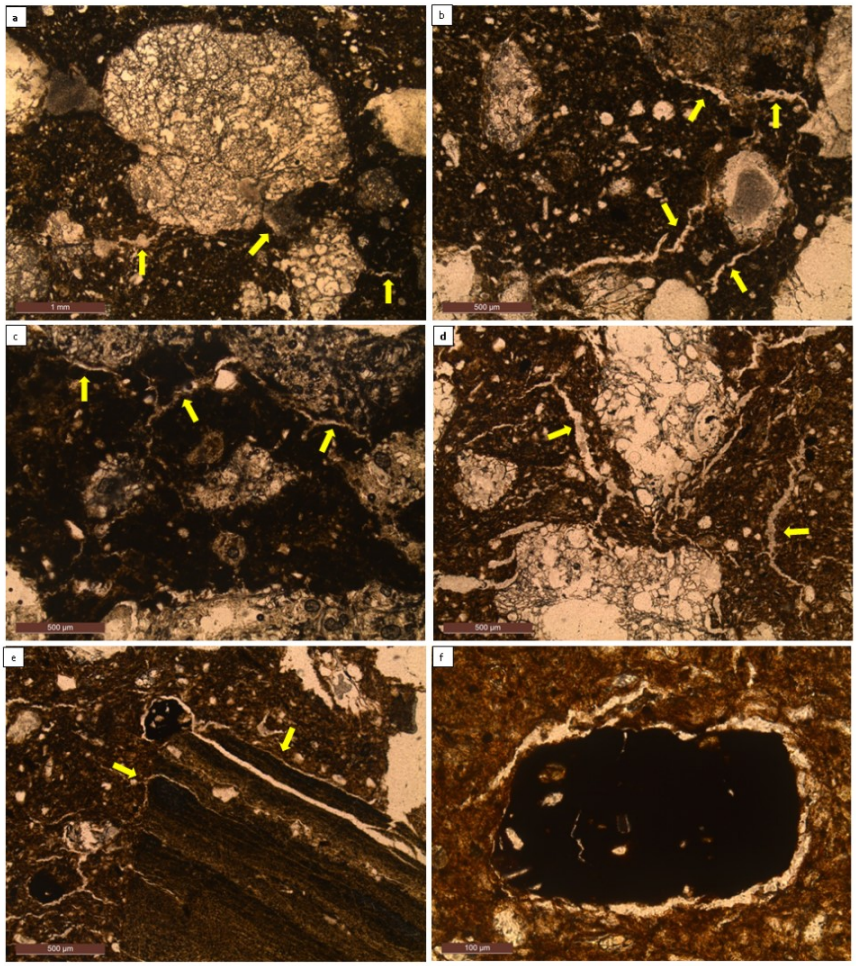

Figure 3.6: Photomicrographs with natural light, showing the main microstructures of the sample containing perlite fired at 800°C: (a) perlite particles with preserved internal structure and formation of secondary porosity in the form of channels. (b) small channels connecting the perlite particles and (c) channels observed in the cross section. Samples fired at 1000°C: (d) formation of channels in greater proportion and size, (e) detail of the interaction of channels with rock fragment and (f) iron oxide/hydroxide crystal with secondary porosity in the form of corona and channels.

3.3.3 Microstructural evaluation

The observation of the samples by optical microscopy allowed to identify the main structural characteristics of the different compositions and their responses to the heating process. Initially, the characteristics of the base material, clay, were studied to understand its behavior, aiming a comparison pattern with the ceramic material with addition of the absorbents. The textures and microstructures observed in the photomicrographs were treated using the program Quantikov [Pinto 1996] to size the visually observed differences (Fig.3.7 and Fig.3.8).

The clay material, used as the base reference, has the maximum amount of 5.7% of fragments supported by the clay matrix. These fragments were identified as quartz crystals, microcline, iron oxides and hydroxides and rock fragments. The largest proportion of these fragments is lower than 10μm: 36% in the sintered sample at 800°C (Fig.3.7a) and 46% in the sample sintered at 1000°C (Fig.3.7b). Approximately 80% of the fragments are smaller than 50μm. Larger fragments with a length of approximately 100μm represent less than 4% of the total. The degree of roundness of these fragments is 0.7, and is not influenced by temperature (Tab.3.1). The matrix remained homogeneous, showing no generation of microstructures observable by optical microscopy.

Samples with attapulgite addition were treated in two steps, initially the particles were measured to evaluate their behavior with the heating process. Subsequently, only the secondary porosities observed in the images were measured. In the sample sintered at 800°C, the attapulgite particles ranged from 256 to 1036μm, with a bimodal behavior, with a moda at 300μ and another at 500μm (Fig.3.7c). In the sample sintered at 1000°C, the particles ranged from 165 to 1127μ (Fig.3.7d). The decrease in the minimum particle size can be explained by the fracturing and fragmentation of the particles, which occurred with the temperature rise, as observed on the images (Figs.3.8d). The maximum size may be considered the same, which shows that the melting occurred during firing process did not generate a change in the volume of the particles that remained entire (Tab.3.2).

In the samples with attapulgite, the formation of a secondary porosity was observed, concentrating predominantly around the particles. Among the various quantified parameters, the main information refers to their corresponding area. In the sample fired at 800°C, the area of the secondary porosity represents 2.8% of the total, and at 1000°C, 4.8%. The total area is also almost double (tab.3.4). These data prove the visual information, that the secondary porosity increases greatly at 1000°C, when compared to the sample fired to 1000°C (Fig.3.8g

and Fig.3.8h). The width of this porosity is very variable, although it is visually estimated that there is an increase at 1000°C, the appearance of new coronas around a larger number of narrower attapulgite particles masks this statistic.

The perlite was added to the base material in the proportion of 20% by weight. Measurements in samples fired at 800°C and at 1000°C represent 25% in area. Although the original perlite fragments are rounded, there is a large variation in the size of the particles whose diameters range from 262 to 3598μm at 800°C (Fig.3.7e) and 380 to 3293μm at 1000°C (Fig.3.7f). The degree of roundness of the preserved particles is 1, however, the average degree of rounding found in both samples is 0.77 (Tab.3.3). These variations can be explained by the breaking of the particles during the transport and elaboration of the material. In the samples with perlite, the secondary porosity with heating was also observed. It has an irregular shape, similar to micro channels, ranging from 18 to 225μm in diameter at 800°C, representing about 1.6% of the sample area. In the sample sintered at 1000°C, the area of this porosity increases to 3.8% and the maximum width reaches 361μm (Tab. 11). The channels are more continuous, thicker and in greater proportion, as observed in the images 3.8i and 3.8j.

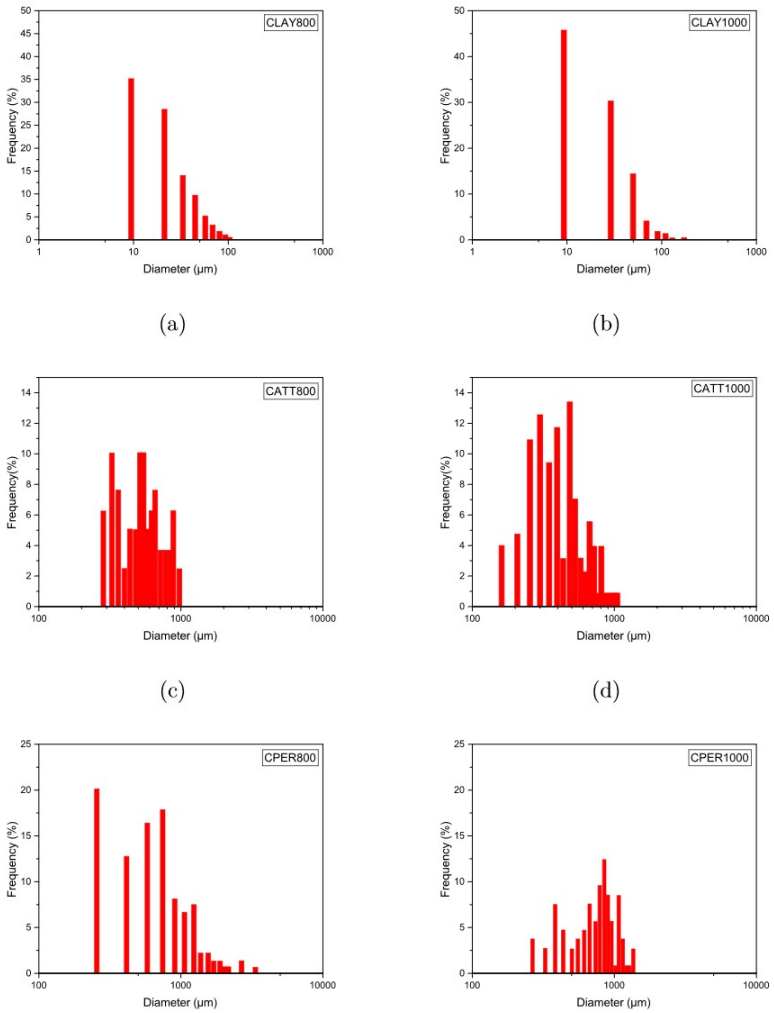

Figure 3.7: Particules size distribution by Quantikov. (a) Clay fired at 800°C, (b) clay fired at 1000°C, (c) clay with attapulgite fired at 800°C, (d) clay with attapulgite fired at 1000°C, (e) clay with perlite fired at 800°C, (f) clay with perlite fired at 1000°C.

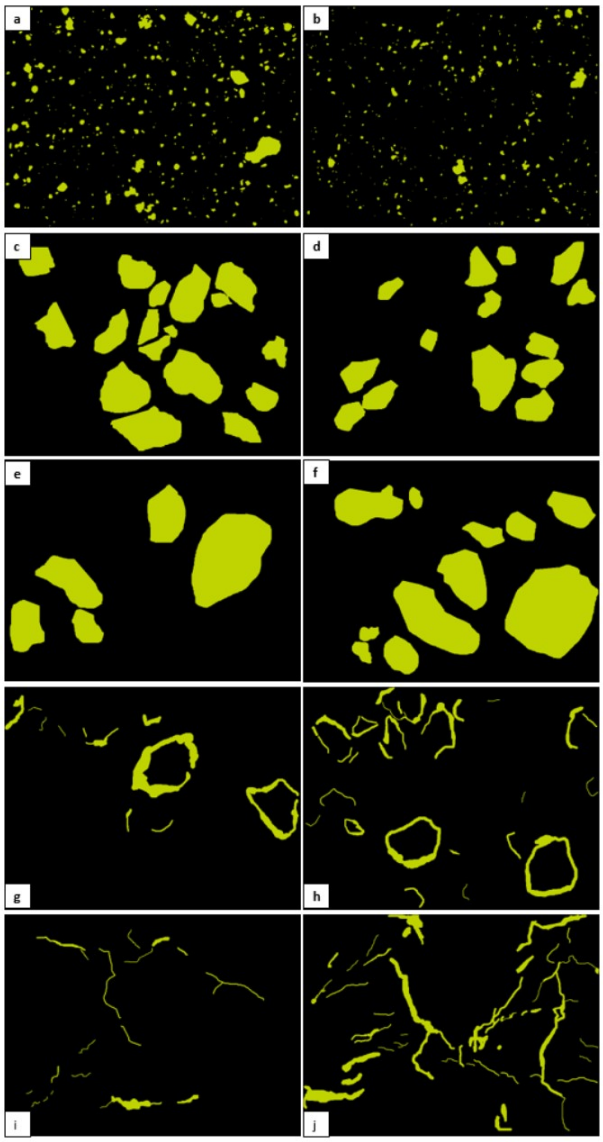

Figure 3.8: Examples of structures identification by the software Quantikov. (a) Clay fired at 800°C, (b) clay fired at 1000°C, (c) clay with attapulgite fired at 800°C, (d) clay with attapulgite fired at 1000°C, (e) clay with perlite fired at 800°C, (f) clay with perlite fired at 1000°C, (g) secondary porosity in clay with attapulgite fired at 800°C, (h) secondary porosity in clay with attapulgite fired at 1000°C, (i) channels at clay with perlite fired at 800°C and (j) channels at clay with perlite fired at 1000°C.

Table 3.1: Quantification of the CLAY microstructural parameters.

Parameter		CLAY 800°C	CLAY 1000°C
Diameter (μm)	Mean	32.475	38.052
	Sdv	24.754	30.891
	Max	255	426.57
	Min	9.6624	9.6624
Roundness	Mean	0.69	0.71
	Sdv	0.096	0.094
	Max	1	1
	Min	0.44	0.44
Number of objects		856	1063
Objects/μm^2		2.5468E-5	3.1627E-5

Table 3.2: Quantification of the CATT microstructural parameters.

Parameter		CATT 800°C	CATT 1000°C
Area (μm^2)	Total	2.3241E7	2.6627E7
	Mean	2.9052E5	2.0641E5
	Sdv	1.8506E5	1.7628E5
	Max	8.0577E5	9.5314E5
	Min	49384	20476
Diameter (μm)	Mean	591.16	484.01
	Sdv	195.87	203.15
	Max	1036.5	1127.3
	Min	256.6	165.23
Roundness	Mean	0.74	0.74
	Sdv	0.087	0.083
	Max	1	1
	Min	0.52	0.52
Number of objects		80	129
Objects/μm^2		5.2273E-7	8.4291E-7

Table 3.2: Quantification of the CATT microstructural parameters.

Parameter	CATT 800°C	CATT 1000°C
Fraction(%)	15.19	17.4

Table 3.3: Quantification of the CPER microstructural parameters.

Parameter		CPER 800°C	CPER 1000°C
Area (μm^2)	Total	1.0957E8	9.7503E7
	Mean	8.116E5	9.3753E5
	Sdv	1.2443E6	5.8916E6
	Max	9.7095E6	2.6858E6
	Min	51581	94340
Diameter (μm)	Mean	886.17	1058.2
	Sdv	546.85	362.77
	Max	3598	1892.4
	Min	262.25	354.66
Roundness	Mean	0.77	0.77
	Sdv	0.084	0.071
	Max	1	1
	Min	0.57	0.58
Number of objects		137	104
Objects/μm^2		3.1756E-7	2.3523E-7
Fraction(%)		25.77	22.05

Table 3.4: Quantification of the CATT (corona) microstructural parameters.

Parameter		CATT 800°C	CATT 1000°C
Area (μm^2)	Total	3.8597E6	6.5327E6
	Mean	32434	27681
	Sdv	51439	38973
	Max	3.487E5	2.3952E5
	Min	1133.6	318.84
Diameter (μm)	Mean	170.75	163.88
	Sdv	119.21	100.48
	Max	681.86	565.12
	Min	30.878	20.618
Roundness	Mean	0.43	0.39
	Sdv	0.15	0.1
	Max	0.78	0.84
	Min	0.14	0.15
Number of objects		119	236
Objects/μm^2		8.7476E-7	1.7348E-6
Fraction(%)		2.837	4.802

3.3.4 Morphology of pores

The images obtained by electron microscopy show the shape and arrangement of the crystals, the granules and the primary porosity in the ceramic material (Fig.3.9). However, quantification of this porosity through image analysis proved to be much more difficult due to the random orientation of the crystals.

The morphological characteristics of the clayey base material show filossilicate leaves still well defined in the sample fired to 800°C (Fig.3.9a). Although the diffraction data showed that the kaolinite did not withstand the temperature rise and that only part of them were transformed to muscovite, the shape of the crystals was preserved (Fig.3.9c). When compared to the images of the clayey material fired at 1000°C there is a softening of the texture, the leaves of the phyllosilicates are less defined, they began to melt, indicating the decrease of the porosity with the increase of the temperature (Fig.3.9b and Fig.3.9d).

In the material with absorbents addition, the matrix exhibits the same behavior of the clay base material with the heating, except for the generation of the secondary porosity shown in item 3.3.2. These absorbents have a much higher primary porosity than the clay base material, but with distinct characteristics. The perlite granules have a rounded, rough surface that are formed essentially of glassy material with bubbles, which are often overlap (Fig.3.10). With the heating process it was observed that the internal structure of the perlite granules in the sample at 800°C (Fig.3.11a) are very similar to those of the original sample (Fig.3.10b) which is expected since perlite starts to melt above temperatures of 900°C [Pichór and Janiec 2009]. At 1000°C the internal structure of the perlite is less homogeneous, the size of the bubbles decreases, the thickness of the edges of the bubbles is larger, part of the bubbles are filled with vitreous material and smooth portions are formed, evidencing the partial melting of the material (Fig.3.11b).

The attapulgite granules are originally less rounded than the perlite ones, their surface is smoother with lamellar internal structure (Fig.3.12). The attapulgite granules in the sample sintered at 800°C still preserve the lamellar texture, although the palygorskite is not stable anymore at this temperature (Fig.3.13a). In the sample sintered at 1000°C, the internal texture of the attapulgite is predominantly fine granular, formed by short prisms smaller than 0.5μm of length (Fig.3.13b). This texture is consistent with the XRD data showing the predominance of quartz and enstatite in attapulgite at the same temperature.

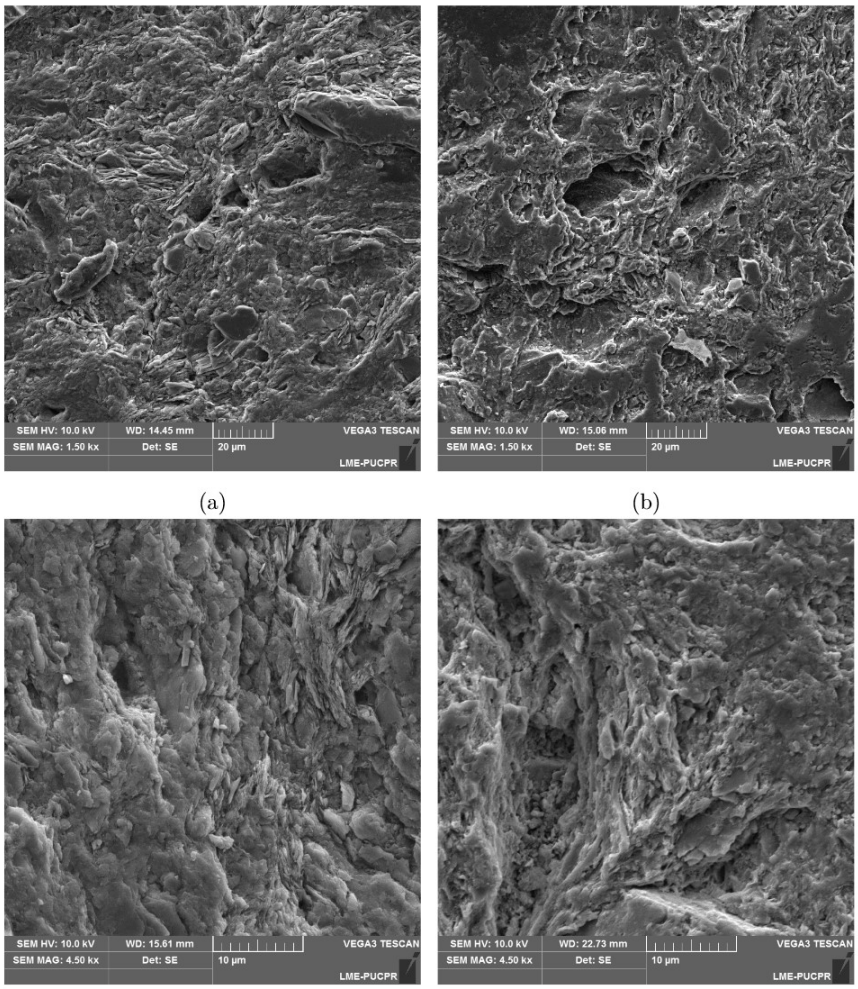

Figure 3.9: SEM images showing clay morphology at two different firing temperatures and magnifications (a) 800°C and 1500x; (b) 1000°C and 1500x; (c) 800°C and 4500x and (d) 1000°C and 4500x.

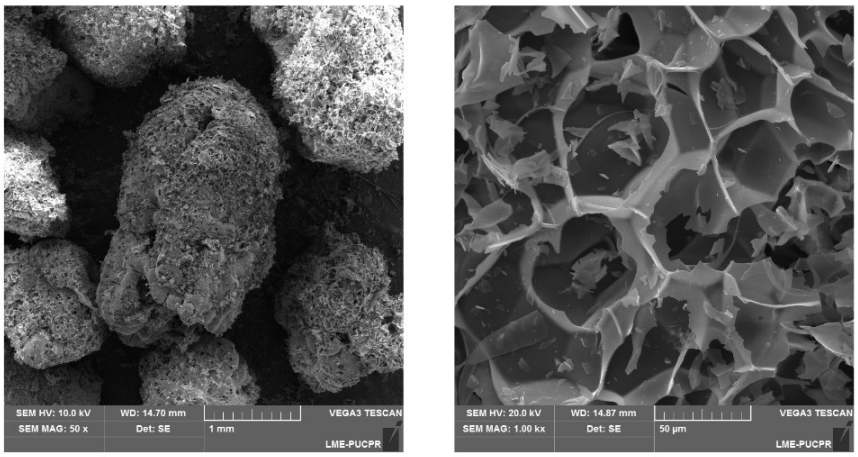

(a) (b)

Figure 3.10: SEM images showing raw perlite grain morphology at different magnifications (a) 50x and (b) 1000x.

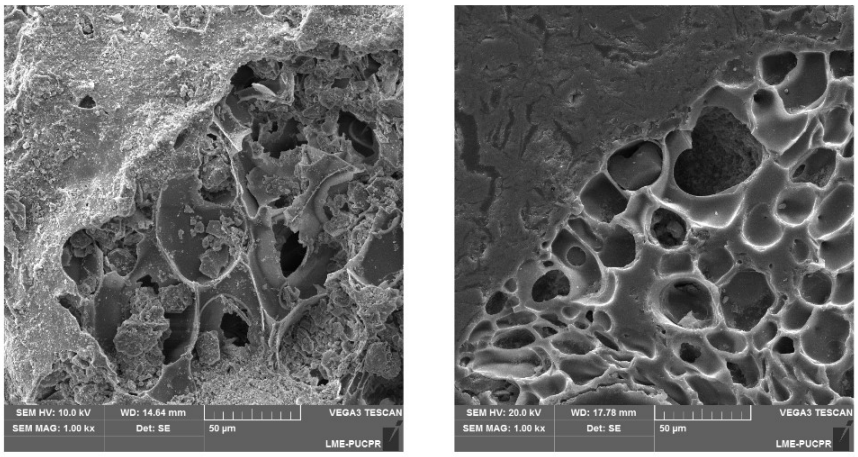

(a) (b)

Figure 3.11: SEM images showing morphology of the composition with perlite addition at a magnification of 1000x for the two firing temperatures: (a) 800°C and (b) 1000°C.

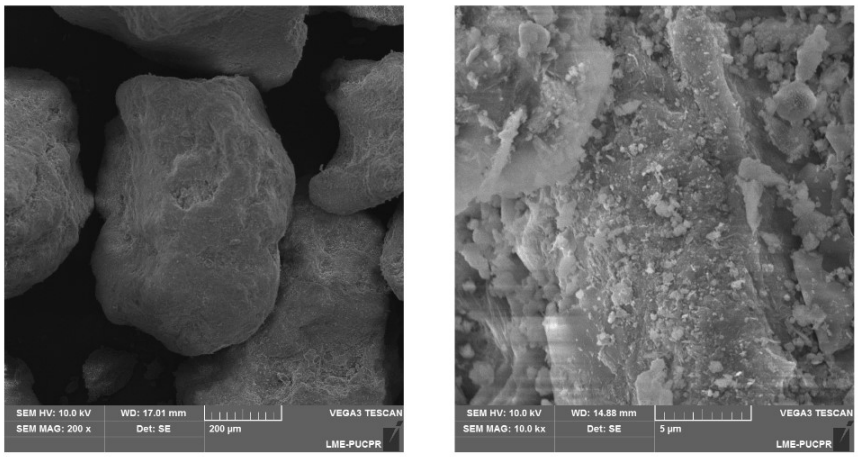

(a) (b)

Figure 3.12: SEM images showing raw attapulgite grain morphology at different magnifications (a) 200x and (b) 10000x.

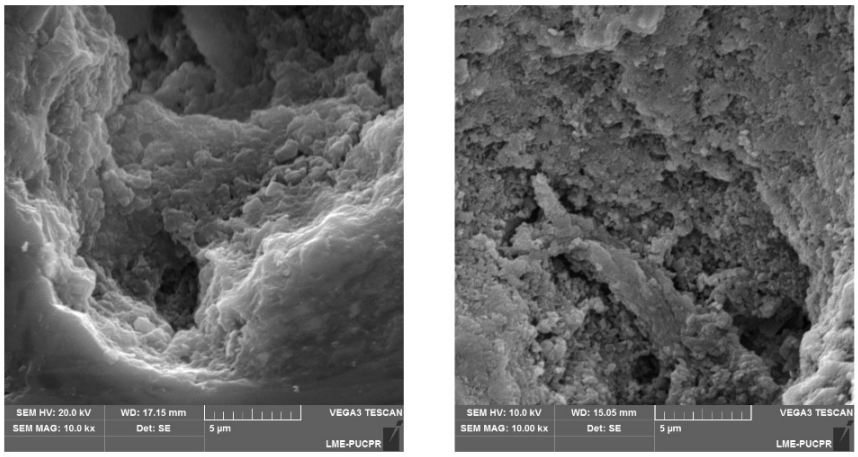

(a) (b)

Figure 3.13: SEM images showing morphology of the composition with attapulgite addition at different sintering temperatures at a magnification of 10000x (a) 800°C and (b) 1000°C.

3.3.5 Pore quantification

A comparison of pore size distribution (PSD) obtained from MIP and N_2 adsorption experiments for samples sintered at 800°C and 1000°C shows a different trend when the additives attapulgite and perlite are incorporated in clay and at two firing temperatures. The BET based technique was performed using nitrogen as the adsorbate at a bath temperature of 77.3K. The relation between pore diameter and pore volume was determinated by the Barrett−Joyner−Halenda (BJH) method and illustrated in Fig.3.14. It shows that, compared to other samples, the composition with attapulgite (CATT) has a microstructure with a greater number of small pores when it is sintered both at 800°C and 1000°C. However, for CLAY and CPER, increasing firing temperature decreases the number of small pores (Figs.3.14a and 3.14b). The surface area and the monolayer adsorption, originated from the adsorption isotherm, were calculated using the BET based method detailed on subsection 3.2.1. Additionally, total pore volume and the mean mesopore diameter were estimated by the BJH analysis and all these data are summarized in Tab.3.5. It can be seen that, clay surface area and total pore volume were increased when attapulgite and perlite were added to the base material for both firing temperature. Moreover, the average pore diameter, decreased for all samples when sintering temperature raises.

Incorporating attapulgite and perlite to clay, diminishes the pore diameter value at 800°C, but at 1000°C, CPER exhibits a higher value of pore diameter than the one for clay. Hall *et al.* [2012] found a positive correlation between pore diameter and pore volume but not with specific surface area for mesoporous silica suggesting that mesopore networks present different levels of corrugation. In this case, surface area and total pore volume are positively related counter to pore diameter. MIP results show that the clay base material has predominantly pores of 100nm at 800°C (Fig.3.15a). Raising firing temperature did not affect substantially clay pore size but diminished the number of pores of this diameter (Fig.3.15b). When perlite is added to clay and fired at 800°C, the mixed material presents a microstructure with a bimodal pore distribution where diameters mostly at 10nm and at 10μm (Fig.3.15a). Fig.3.15b revels that increasing firing temperature, changes CPER pore distribution with diameters values situate mostly at 100nm and in the interval from 1μm to 100μm. CATT has a bimodal pore distribution of mainly 100nm and 10μm at 800°C and still has a bimodal distribution at 1000°C, with an increment of the number of these pore groups.

Table 3.5: N_2 adsorption measurements for CATT, CPER and CLAY samples at different firing temperatures.

Sample	Specific surface area (m^2/g)	Total pore volume (cm^3/g)	Pore diameter (nm)
CLAY 800°C	18.3	0.12	5.46
CLAY 1000°C	7.02	0.05	1.84
CATT 800°C	29.53	0.16	2.36
CATT 1000°C	11.94	0.09	1.61
CPER 800°C	19.1	0.13	3.66
CPER 1000°C	9.24	0.08	2.42

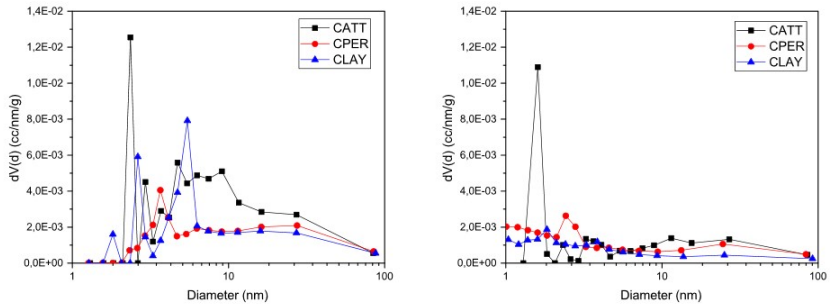

(a) (b)

Figure 3.14: Pore size distribution from nitrogen adsorption test: (a) samples sintered at 800°C and (b) samples sintered at 1000°C.

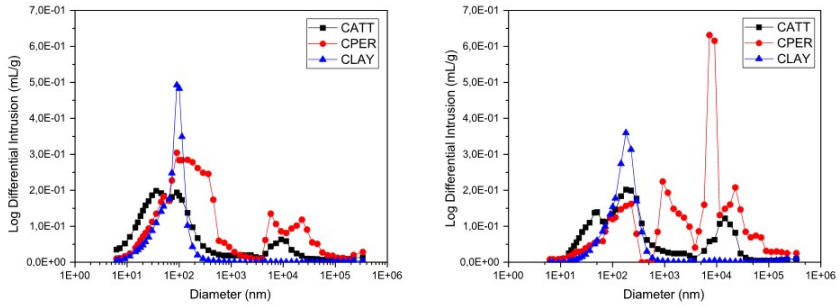

(a) (b)

Figure 3.15: Pore size distribution from mercury intrusion test: (a) samples sintered at 800°C and (b) samples sintered at 1000°C.

The smaller pores measured by nitrogen adsorption (BET) were not observed by optical microscopy and, although some of them have been observed by electron microscopy, it was not possible to quantify them with the use of this technique. On the other hand, the mercury porosimetry data can be correlated to the microstructures studied. Samples show distinctly two groups of porosity: pores in the order of 10^2nm and pores of the order of 10^4nm. The pores of the first group can be correlated to porosity found in the three samples (clayey base material, clay with perlite and clay with attapulgite). The second group refers to the secondary porosity, formed during heating process for the samples with the additives, as observed in the optical microscopy images.

At 800°C, in the sample with attapulgite addition, the first group of pores has a bimodal distribution, where the pores with smaller diameter are related to attapulgite granules and the pores with larger diameter refer to the clayey material of the matrix and are coincident with the peak of the clayey base material. In the sample with addition of perlite, the opposite occurs because the perlite porosity is much larger, as shown in Fig.3.15.

In samples sintered at 1000°C, there is a reduction of primary porosity and the increasing of the secondary porosity both with perlite and attapulgite addition to clay. Although the secondary porosity area of the samples containing attapulgite, observed in the images and measured by Quantikov, is greater that the one found for the samples with perlite, the Hg porosimetry method shows that the amount of measured pores is higher in the sample with perlite than for the one with attapulgite. This can be explained by the shape of these secondary

pores: the attapulgite corona-shaped pores are isolated, whilst the secondary porosity of the sample with perlite is interconnected, facilitating the percolation of fluids.

3.3.6 Mechanical properties

To investigate the load bearing capacity of the building materials including the perlite and attapulgite additions and fired at two different temperatures, a three point bending test was performed on samples with 20% by weight of additives incorporation.

Figure 3.16 show that firing temperature and additives play an important role on mechanical properties of ceramic materials. It can be seen that mechanical strength increases with firing temperature for mixed materials. This is mostly due to the sintering process that takes place between 900-1000°C causing the reduction of porosity and compaction of particles [Kshama *et al.* 1992]. The formation of the crystalline phase during the sintering process in the ceramic matrix provides a piece with a high fired mechanical strength [Jordan *et al.* 2008]. Novais *et al.* [2015] also reported lower bending strength values with increasing porosity for a bi-layered ceramic tile.

It was then expected that perlite and attapulgite decrease mechanical strength since they boosted clay porosity. Additionally, Jiang and Guan [1999] analyzed the influence of pore size on bending strength for pastes made with different fly ash contents and concluded that pores bigger than 100nm have a sharper effect on decreasing flexural strength. Yakub *et al.* [2012] studied the mechanical properties of porous clay ceramics, fabricated by sintering a mixture of clay and woodchips as pore-formers and observed that elastic modulus decreased as the average pore size increased. Indeed, the addition of perlite decreased significantly the bending strength owing to its wider number of pores bigger than 100nm and microstructural flaw size. The channels formed during the firing process also contribute to material fragilization. Analogously, attapulgite addition decreased bending strength but not as much as perlite composition. This is probably because of its smaller pores and the secondary porosity 'coronas' which are closed.

Therefore, decreasing density, allowing good porosity and lower thermal conductivity, inevitably comes at the cost of reduced mechanical strength [Aouba *et al.* 2016].

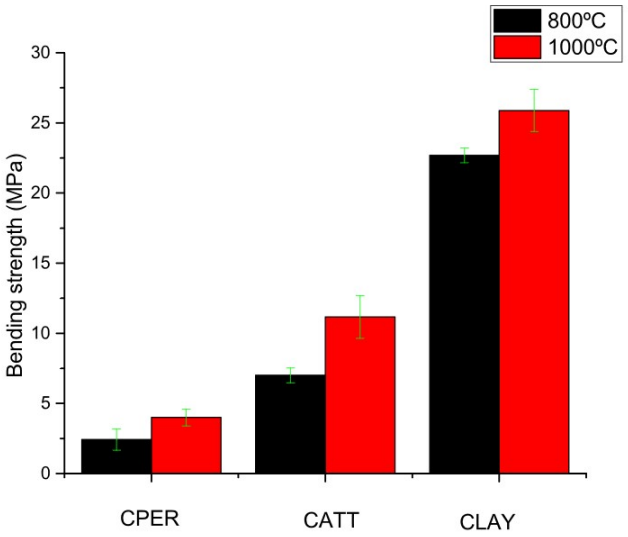

Figure 3.16: Mean bending strength values for samples sintered at 800°C and at 1000°C. The error bars depict the standard deviation.

3.4 Conclusions

This chapter presented a detailed microstructural characterization of a clay material, a clay with addition of attapulgite and a clay with addition of perlite. Results were obtained for all samples at the firing temperatures of 800°C and 1000°C.

The following conclusions can be extracted from this study:

I. The observation of the textures of the original clay material by optical and electronic microscopy showed that there was no generation of secondary porosity with the firing temperature. The addition of attapulgite generated secondary porosity in the form of coronas around the particles. Comparing materials sintered at 800 and at 1000°C, there is an increase in area and quantity of these coronas. The coronas shape, circular but isolated, will act as a closed porosity. In the sample with perlite addition, a secondary porosity was generated in the form of channels, which increased in size and width with the increase of firing temperature, forming a network with high connectivity.

II. The mineralogical study through XRD showed that there was variation of phases with the firing of the material. Attapulgite granules, initially formed by palygorskite, lizardite, muscovite and quartz are partially amorphized and the remaining minerals re-equilibrate. Paligorskite and lizardite disappear. At 800°C there are still muscovite peaks, quartz and enstatite. At 1000°C, the quartz and enstatite peaks predominate. Paligorskite is a mineral with high natural porosity and sorption capacity, hence, its disappearance or rebalancing for other mineral phases leads to a decrease in the primary porosity of the material. The amorphization observed in the diffraction occurs due the partial melting of the material, as observed in optical and electronic microscopy. Perlite granules showed evidence of partial melting and decreased internal porosity when sintered at 1000°C .

III. The generation of the secondary porosity can be compared with the mercury porosimetry data. The increased interconnectivity of secondary porosity in the samples with perlite at 1000°C may explain the increase in pore size showed by the porosimetry test. In the sample with attapulgite, although the increase in secondary porosity at 1000°C is clearly observed in the pore group of greater size, the measured porosity is lower compared to one obtained by the addition of perlite at the same temperature. This behavior is due to the fact that this porosity remains isolated.

IV. Pore size distribution and the generation of the secondary porosity can be compared with mechanical results. The pores of greater size of the composition with perlite significantly weakened the material as well as the interconnectivity of secondary porosity in the samples. On the other hand, a higher sintering temperature increased the bending strength.

Chapter 4

Hygrothermal properties and characterization of fired clay-based ceramic composites

This chapter aims to present the hygrothermal characteristics measured, on a material scale, for clay-based materials. After a presentation of their formulation and how they were produced in the Chapter 2, this chapter begins with an introduction dealing with a short theoretical explanation of the performed hygric analysis. This stage is followed by the description of the experimental characterizations and finally by the presentation of the experimental results with their analysis.

Contents

4.1 Introduction **105**

4.2 Materials **105**

4.3 Sample characterization techniques **106**

4.3.1 Climate chamber (RHBOX) 106

4.3.2 Sorption isotherm 107

4.3.3 Water vapor permeability 109

4.3.4 Water absorption coefficient 111

4.3.5 Thermal conductivity 112

4.4 Results and Discussion **113**

4.4.1 Sorption isotherms 113

4.4.2 Water vapor permeability 116

4.4.3 Water absorption coefficient 118

4.4.4 Thermal conductivity 121

4.5 Conclusions **123**

4.1 Introduction

This chapter presents the hygrothermal characterization of clay-based materials produced by means of different additives, and sintered at two temperatures: 800°C and 1000°C (as commented in Chapter 2).

The hygric behavior is analyzed based on sorption isotherms, water vapor permeability, moisture buffer value and the water absorption coefficient. The thermal behavior has been expressed by a direct measurement of thermal conductivity and thermal effusitivity.

Concerning hygric behavior, the two types of moisture storage and transport were considered: vapor and liquid. Sorption isotherms, water vapor permeability and moisture buffer capacity can give an idea of water vapor behavior in materials. Indeed, at low water content, the transfer of moisture in the vapor phase is predominant. At a water content greater than the critical water content the diffusion of liquid phase is increasingly important in relation to the vapor phase.

As previous mentioned, in the super-hygroscopic area capillary flow is the dominant transport mechanism. Therefore, liquid phase is expressed in the water absorption coefficient test.

Moisture storage is represented by sorption isotherms which are fitted by the GAB (Guggenheim-Anderson-de Boer) equation and also by the moisture buffer value (MBV) which will be reported in Chapter 5. Vapor transport is described by water vapor permeability test which is determined with the help of dry-cup method. The vapor diffusion resistance factor is also calculated.

The differences regarding hygrothermal behavior are closely related to the microstructure of materials. Therefore, we use results of Chapter 3 to explain the hygric performance of the six selected samples.

Further information about the exploitation of experimental results can be found in Appendix E.

4.2 Materials

Compositions prepared by mixing clay and absorbents in the previous chapter, were characterized here. Table 4.1 summarizes the produced materials which were sintered at 800°C and at 1000°C.

Table 4.1: Different compositions sintered both at 800°C and at 1000°C.

Clay + 20%wt Montmorilonite (CMMT)
Clay + 20%wt Attapulgite (CATT)
Clay + 20%wt Diatomite (CDIA)
Clay + 20%wt Sepiolite Gravillon (CSGR)
Clay + 20%wt Sepiolite Sable (CSSA)
Clay + 20%wt Vermiculite (CVER)
Clay + 20%wt Perlite (CPER)
Clay + 20%wt Sepiolite Ultra Fine (CSUF)
Clay + 20%wt Zeolite (CZEO)

4.3 Sample characterization techniques

The properties of the raw materials and of the final products were determined by using various techniques. Sorption isotherms were obtained by saturated salt solutions, water vapor permeability by the cup method, water absorption coefficient by partial immersion and, finally, thermal conductivity by direct measurement using a C-Therm analyser.

All procedures are detailed in the following sections.

4.3.1 Climate chamber (RHBOX)

At the Laboratory for Optimization of Design and Environmental Engineering (LOCIE) there are two of this climatic chambers named RHBOX that are interconnected (Figs.4.1). This setup is a large polycarbonate box sealed by joints and capable of keeping a certain level of temperature and humidity in each chamber. Inside, there is a heat exchanger located at the rear and controlled by a thermostattedd bath outside the enclosure. Inside each box there are two fans controlled by an external supply to allow the air to circulate inside and to homogenize the distribution of the temperature and relative humidity. Fans are only activated when salt solution is changed; during weighings they are turned off. Relative humidity is controlled by saturated salt solutions. Temperature is regulated by means of the exchanger and the thermostatted bath: a temperature is imposed on the bath which will then circulate the fluid in the exchanger and make it possible to control the temperature inside the enclosure. The manipulations of samples are carried out using gloves fixed to the front of the box and

the passage of the samples and the necessary elements for the tests is done by a lock on the side. Two scales (Mettler-Toledo XPE603S) are also attached to the top of each enclosure to weigh the samples. Finally, the measurement of the relative humidity and temperature inside the boxes is made using thermocouples and hygrothermal sensors. The values of the temperature measured by the thermocouple are continuously acquired by a program based on LabVIEW. Hygrothermal sensors can record both temperature and RH and data can be read with the help of the Warito software from Waranet Solutions. This climate chamber was used to perform the tests of moisture buffer value (MBV) (section 5.1), water vapor permeability (section 4.3.3) and thermal conductivity (section 4.3.5).

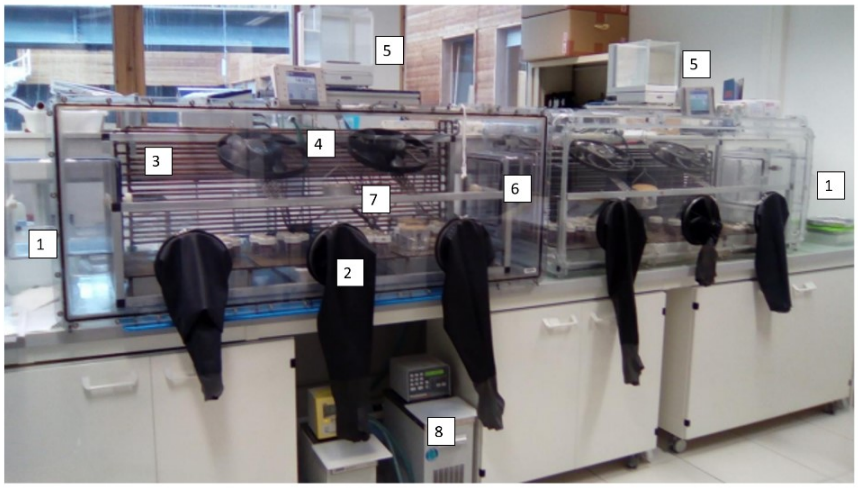

Figure 4.1: Photo of the climate chamber (RHBOX) at LOCIE: 1 - entrances of the RHBOX; 2 - gloves used to manipulate samples inside the chamber; 3- heat exchanger used to regulate internal temperature; 4 - ventilators that help to homogenize internal relative humidity; 5 - precision scales; 6 - channel that connects the two chambers; 7 - sample being wheighed inside the chamber; 8 - thermostatted bath.

4.3.2 Sorption isotherm

Sorption isotherms can be obtained by submitting samples to an environment with controlled humidity and constant temperature. Humidity can be controlled by salt solutions. This is a very robust and inexpensive method, therefore it was used in our work. However, this method has some limitations such as: a few points are measured and the highest humidity level generally

obtained is around 97%. Extrapolation can then be done by theories of physical adsorption or by mercury intrusion test [Mendes 1997]. Table 4.2 summarizes relative humidity produced by seven salt solutions at 30°C, used in the present work.

Table 4.2: Humidity levels generated by saturated salt solutions of sorption curves at 30°C.

Salt solution	Humidity level (%)
KOH	7
CH_3CO_2K	22
$MgCl_2$	33
NaBr	57
NaCl	75
KCl	85
K_2SO_4	97

In order to measure adsorption isotherms, samples were previously dried in an oven at 105°C and then weighed (m_0). Samples of each composition were placed in a box with the correspondent salt solution, being periodically weighed until a constant mass (m_1) is reached (the rate of increase in mass of adsorbed moisture is less than 0.01 g in 24 h) . Then, they were moved to another box with different relative humidity values: 7% to 22%, 22% to 33%, 33% to 57%, 57% to 75%, 75% to 85% and 85% to 97%. Again, samples were periodically weighed until reaching a constant mass in the new humidity level (m_3). Then the moisture content is given by Eq.29:

$$u_a = \frac{m_3 - m_0}{m_0}. \tag{29}$$

Desorption isotherms were measured by moving samples from adsorption test (m_3) to another box with different relative humidity, in the following order: 97% to 85%, 85% to 75%, 75% to 57%, 57% to 33%, 33% to 22% and 22% to 7%. Samples were periodically weighed until reaching a constant mass in the new humidity level (m_4). Then, the moisture content is given by Eq.30:

$$u_d = \frac{m_4 - m_0}{m_0}. \tag{30}$$

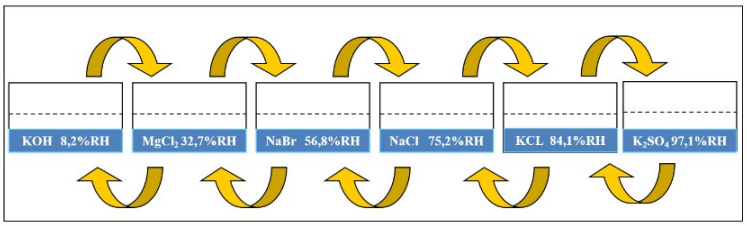

Figure 4.2: Schematic drawing of the method used to measure sorption isotherms

4.3.3 Water vapor permeability

Water vapor permeability was determinated by the cup method based on the international standard [ISO12572 2001]. Before testing, the test specimens were stored at 30°C, 57% relative humidity until stabilization of sample weight. The test specimen is sealed to the open side of a test cup containing a desiccant (dry cup). The assembly is then placed in the test chamber (RHBOX). The sample dimensions are: 49mm x 49mm x 5mm. Because of the different partial vapour pressure between the test cup and the chamber, a vapour flow occurs through permeable specimens. Periodic weighings of the assembly are made to determine the rate of water vapour transmission under a steady-state regime. Two different humidity levels in the RHBOX were used: 33% and 75% and a constant temperature of 25°C. The relative humidity in the dry cup is considered at 6%. The mass change rate was calculated, Δm, using Eq.31 :

$$\Delta m = \frac{m_2 - m_1}{t_2 - t_1}, \tag{31}$$

where:

Δm is the change of mass per time for a single determination, in kg/s;

m_1 is the mass of the specimen at time t_1, in kg;

m_2 is the mass of the specimen at time t_2, in kg;

t_1 and t_2 are the successive times of weighings, in s.

The regression line between mass and time was calculated. The slope of this line is G, in kg/s.

The density of water vapor flow rate, g_v, is then given by Eq.32

$$g_v = \frac{G}{A}, \tag{32}$$

where:

A is the exposed area of the test specimen, in m^2.

Vapor pressure on either side of the specimen may be calculated from the temperature and relative humidity using Eq.33 [BS5250 1989]:

$$p_v = \varphi \ 610.5 \ e^{\frac{17.269\Phi}{237.3+\Phi}}, \tag{33}$$

where:

Φ is the temperature, in $^{\circ}\mathrm{C}$;

φ is the relative humidity .

The relative humidity was calculated as a mean of the value in the inner part of the cup (considered 6%) and the outside value (75% or 33%).

Therefore, since the gradient of vapor pressure (Δp_v) and the density of water vapor flow rate (g_v) are known, Eq. 17 can be rearranged to:

$$\delta_v = g_v \frac{d}{\Delta p_v}, \tag{34}$$

where:

d is the thickness of the specimen, in m.

In practice, there are water resistances imposed on the transfer of vapor through the sample in addition to the resistance of the sample. Therefore, the permeability will be considerably underestimated in the case of highly hygroscopic materials. The water vapor resistance to the water vapor flow that occurs in the air between the saline solution and the inner surface of the sample, can be expressed as:

$$Z = \frac{d_a}{\delta_a} \tag{35}$$

where:

d_a is thickness of the air space, in m.

In order to take this resistance into account, Eq. 34 becomes:

$$\delta_v = \frac{d}{\frac{\Delta p_v}{g_v} - Z}. \tag{36}$$



Figure 4.3: Cup method with silica gel (blue)

4.3.4 Water absorption coefficient

The movement of moisture within hygroscopic capillary building materials is a combination of vapor and liquid flows. As stated in section 1.2.4, liquid uptake can be estimated by a coefficient using a simple gravimetric technique. It assesses the rate of absorption of water, by capillary action.

In this case, the water absorption coefficient is obtained by partial immersion in distilled water. The sample is placed in an apparatus that maintains a constant level of water and weighed periodically. Water level in contact with sample is kept to 3mm. The coefficient can be determined by measuring the change in mass of the test specimen, the bottom surface of which is in contact with water, over a period which is usually at least 24 h. The water contact area of each test specimen is 30.25 cm^2, thickness is 15mm and samples are side protected with wax and an aluminum tape to avoid water rising on the sides. Samples are also pre-conditioned at 30°C and at 57% relative humidity. Before the measurement, sample is superficially drained and wiped. The slope of the graph of mass variation against the square

root of weighing times gives the water absorption coefficient (Eq.37).

$$A_c = \frac{\Delta m_f - \Delta m_0}{\sqrt{t}}, \tag{37}$$

with:

$$\Delta m_f = \frac{m_f - m_0}{A}, \tag{38}$$

Where:

m_f is the mass at the end of the weighing, in kg;

m_0 is the mass in the beginning of the weighing, in kg;

A is the area of the base of the specimen, in m^2;

Δm_f is the value of Δm on the straight line at time t_f, in kg/m^2;

Δm_0 is the value of Δm on the straight line at time t_0, in kg/m^2;

t is the total duration of the test, in seconds;

A_c is the water absorption coefficient, in $kg/(m^2.s^{0.5})$.

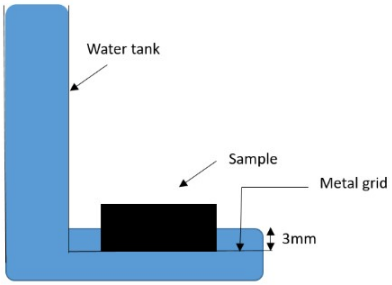

Figure 4.4: Experimental setup to measure water absorption coefficient.

4.3.5 Thermal conductivity

Thermal characterization was performed using a thermal conductivity analyzer from C-Therm technologies. The C-Therm TCi Thermal Conductivity Analyzer employs the Modified Transient Plane Source (MTPS) technique to characterize the thermal conductivity and effusivity of materials. It employs a one-side, interfacial heat reflectance sensor that applies a momentary constant heat source to the sample. Typically, the measurement pulse is between 1 to

3 seconds. Thermal conductivity and effusivity are measured directly, providing a detailed overview of the heat transfer properties of the sample material. Compared to other thermal conductivity methods such as traditional guarded hot plate, transient plane source and laser flash diffusivity, TCi requires an easier sample preparation, testing time takes seconds, it is a non-destructive method and it can measure a wider ranges of conductivity and effusivity.

Measurements were made at 33% and 75% RH in the RHBOX and for materials sintered at 800°C and 1000°C. Samples of about 49mm x 49mm x 5mm were side covered with grease in order to facilitate heat transfer in materials. A few measurement cycles until the sample stops absorbing the grease were performed and values were quite variables, thus an average value is presented for each material. Grease is a contact agent that is taken into account in the calibration of the device.

4.4 Results and Discussion

4.4.1 Sorption isotherms

The measured adsorption/desorption curves are shown in Fig. 4.5. They all belong to type II with the hysteresis loop type H3 according to IUPAC recommendations (Fig. 1.9). This type of curve characterizes the mesoporous and macroporous materials. It can be observed that the adsorption isotherms of the materials display a similar pattern, which is to be expected because they have the same base material.

As the relative humidity increases, the moisture content raises (in this case is represented as a percent variation of mass -u-), due to adsorption of more water. For all compositions, when relative humidity exceeds 75%, moisture content increases higher than at low RH. Although points at 85% and 97% of relative humidity were difficult to measure due to the condensation effect in the boxes where samples were placed, at 97%RH, the moisture content of CSSA is the highest (Fig. 4.5e). This fact may be associated with the microstructure of clay-based materials. Indeed, it can be seen from CPER microstructure that the number of pores with wider diameter increases with firing temperature (attributable also to the formation of secondary porosity) and this can favor water absorption by capillary suction. All absorbents increased the moisture adsorption of CLAY for samples sintered at 800°C. Same behavior is not observed in the curves of samples sintered at 1000°C which have a lower sorption capacity.

From Fig. 4.5, it can be seen that there is a different sorption behavior of fired clay

materials when sintering temperature is increased. Water vapor adsorption/desorption highly decays at higher firing temperatures for all compositions due to the reduction of specific surface area and the elimination of small pores during sintering process. However, at 97%RH samples sintered at 1000°C exhibit higher values moisture content probably because of the pores with bigger diameter formed during sintering process.

All ceramic materials tested showed hysteretic effect which means that the moisture content during adsorption is smaller than the one during desorption and their significance differed depending on the composition. Hysteresis can be explained by the presence of ink-bottle pores with the pore diameter of about 100nm and higher [Koronthalyova 2016], capillary condensation and contact angle hysteresis. Therefore, all the adsorbed moisture is not desorbed and thus the moisture content of the desorption curve is higher than that of the sorption curve.

It is convenient to describe the sorption isotherms by an analytical relation for simulation of hygro-thermal performance of building materials. Moreover, the interest of using physical models comes from the fact that the parameters have a physical meaning and therefore do not take any value. Rudy *et al.* [2017] compared several formulas describing the water vapor sorption and ranked GAB as the best fitting model. It is was also used for clay-based materials [Chemkhi *et al.* 2004]. Therefore, in this work, curves were approximated with the GAB model (Eq. 5). The adjusted R^2 remained close to 1, corresponding to a very good correlation between the model and the experimental curve. The lowest correlations ($R^2 \approx 0{,}964$) were found for adsorption and desorption curves of CVER, CLAY, CSUF and CZEO all sintered at 1000°C. GAB model constants and R^2 are given in Appendix C.

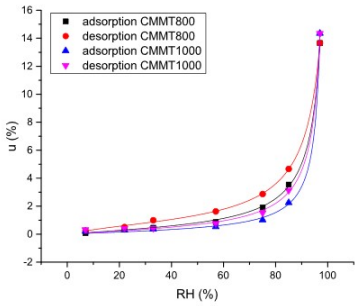
adsorption CMMT800
desorption CMMT800
adsorption CMMT1000
desorption CMMT1000
u (%)
RH (%)

(a)

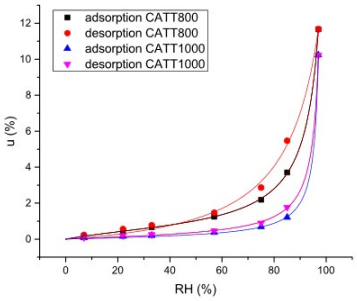
adsorption CATT800
desorption CATT800
adsorption CATT1000
desorption CATT1000
u (%)
RH (%)

(b)

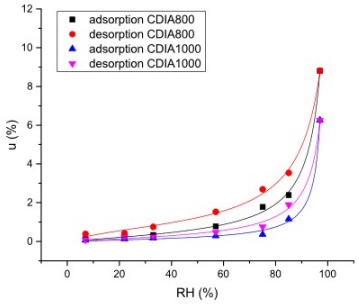
adsorption CDIA800
desorption CDIA800
adsorption CDIA1000
desorption CDIA1000
u (%)
RH (%)

(c)

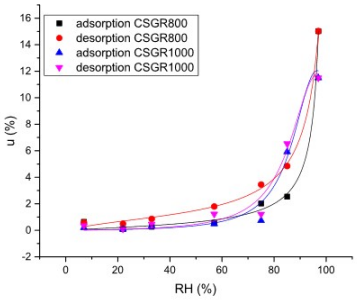
adsorption CSGR800
desorption CSGR800
adsorption CSGR1000
desorption CSGR1000
u (%)
RH (%)

(d)

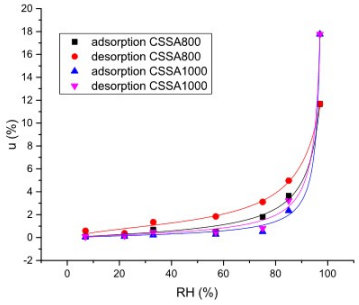
adsorption CSSA800
desorption CSSA800
adsorption CSSA1000
desorption CSSA1000
u (%)
RH (%)

(e)

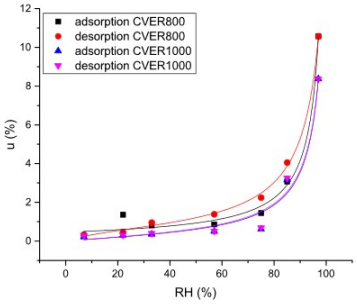
adsorption CVER800
desorption CVER800
adsorption CVER1000
desorption CVER1000
u (%)
RH (%)

(f)

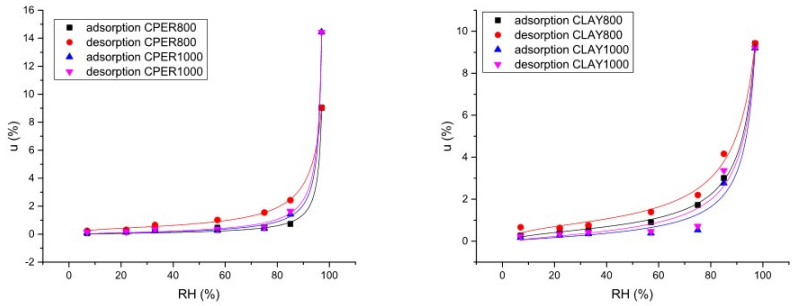

(g)

(h)

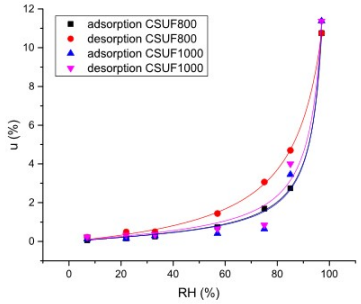

(i)

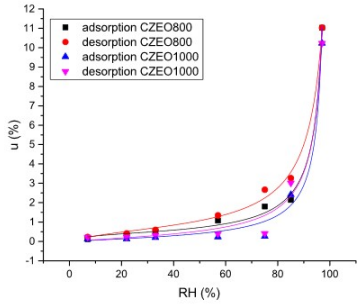

(j)

Figure 4.5: Measured water vapor adsorption and desorption curves for samples sintered at 800°C and at 1000°C and their approximations using GAB model: (a) clay with montmorillonite; (b) clay with attapulgite; (c) clay with diatomite; (d) clay with sepiolite gravel; (e) clay with sepiolite sand; (f) clay with vermiculite; (g) clay with perlite; (h) fired clay; (i) clay with sepiolite ultra-fine; (j) clay with zeolite.

4.4.2 Water vapor permeability

When it comes to hygrothermal characterization, the water vapor permeability, δ_v, is an important parameter. At low humidity levels, the moisture transport is mainly governed by vapor transfer although menisci of water are already formed in narrow pores. Thus, the cup test allows the quantification of this water vapor flux through the sample. Results are indicated in Fig. 4.6.

The water vapor permeability value obtained for clay is in agreement with values commonly

found for this type of material [Dondi *et al.* 2003; Gomez *et al.* 2007]. It can be seen that all absorbents increase clay water vapor permeability for all tested relative humidity (33% RH and at 75%RH). Compositions containing diatomite, zeolite and perlite provided the highest values. As the moisture levels increase, it is also expected the water vapor permeability value to be greater. Tveit [1966] showed that water vapor permeability increases with relative humidity for different building materials. Same behavior is observed for all compositions in our experiments as it is illustrated in Fig. 4.6.

Sintering temperature also plays an important role on water vapor diffusion. It was observed that compositions sintered at 1000°C presented higher values when compared to 800°C. This fact can be related to microstructure since it is well known, that during sintering the smaller pores coalesce, giving rise to a coarser residual porosity. Dondi *et al.* [2003] statistically analyzed δ_v values and the microstructural variables of bricks and found a positive correlation of the water vapour permeability with a coarser porosity. In addition, Togkalidou *et al.* [2013] which studied various microstructure parameters of different building materials, including bricks, and aimed to correlate them to the water vapor permeability, concluded that the highest contribution to water vapor permeability is for the pore size distribution that corresponds to pore radius sizes greater than 10μm, in the case of materials which present a wide pore size distribution, toward coarser pores. In the case of materials with a narrow pore size distribution, toward smaller pores the highest contributions to permeability correspond to pore radius sizes between 0.421 and 1.778μm. In the case of CPER and CATT compositions, the microstructural analysis corroborates this statement. The coarser pores reveled by MIP at 1000°C probably due to coronas formed in CATT and the channels formed in CPER microstructure may increase δ_v-value. CATT value is lower than CPER because its coronas remain isolated and less connected than CPER channels.

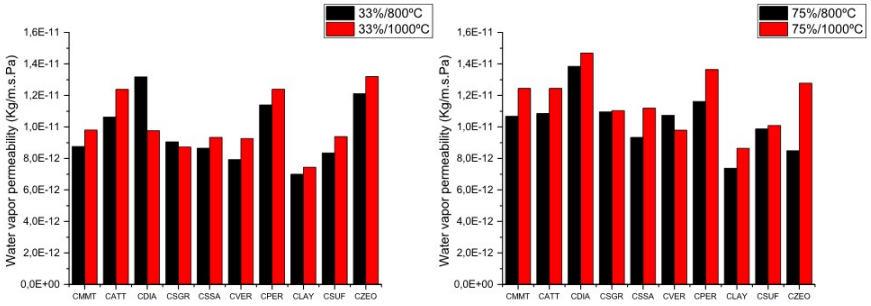

(a) (b)

Figure 4.6: Dry cup water vapor permeability for samples sintered at 800°C and at 1000°C exposed to the relative humidity of: (a) 33% (b) 75% .

4.4.3 Water absorption coefficient

The capillary absorption test can characterize the water content profiles during the imbibition process while the material is in contact with water. Considering the variation of the mass of the samples during time, it is possible to obtain the water absorption coefficient (A_c). This coefficient compares the capacity of absorbing water by capillarity of the different building materials.

According to Bomberg *et al.* [2005], there are many sources of uncertainties in the measurement of A_c coefficient mainly for bricks due to its nature and production process. The contact area, type of side protection, type of drying, period of testing and the initial time of weighing have an important effect on the final result. To obtain a A-coefficient that is constant enough, the initial two data points from the measured results were excluded and it was found an average value of 0.1490 $[kg/m^2s^{0.5}]$ for ceramic bricks. Mukhopadhyaya *et al.* [2002] encountered an average of 0.084 $[kg/m^2s^{0.5}]$ for red clay bricks. For Raimondo *et al.* [2009], values varied from 0.06 to 0.35 $[kg/m^2s^{0.5}]$ for clay bricks. Karagiannis *et al.* [2016] found A_c values of 0.249 and 0.198 $[kg/m^2s^{0.5}]$ for two different clay bricks.

In this work, A_c for brick sintered at 800°C was 0.501$[kg/m^2s^{0.5}]$ and this value almost remained the same (0.505$[kg/m^2s^{0.5}]$) with the increasing sintering temperature to 1000°C. It suggests that microstructural changing during firing process did not seem to affect the water absorption coefficient for clay as it was expected. In other words, if it is true that a less dense

ceramic body is able to absorb a higher liquid amount for the same porosity, the influence of the other parameters characterizing the capillary structure is not obvious [Raimondo *et al.* 2009]. A less homogeneous microstructure of samples selected to this test could explain these similar values regardless firing temperature. Nevertheless, it is important to note that A_c-value calculation was extremely sensible to the choice of initial and final times of weighing.

On the other hand, incorporating absorbents to clay affects its absorption coefficient. Fig. 4.7 shows that adding absorbents to clay increases clay water absorption coefficient. Also, all compositions improved water absorption coefficient at a higher sintering temperature in particular CSSA which has the highest A_c-value. This fact is probably due to the better connected and homogeneous microstructure formed with absorbents addition and with the increasing of sintering temperature. In the case of perlite addition (CPER), for example, it was observed the presence of more interconnected channels when compared to clay microstructure and the increase of these channels with sintering temperature (chapter 3). Indeed, A_c value for CPER is higher than CLAY and even more at 1000°C (Fig. 4.7a). Same trend is observed for attapulgite addition (CATT) which improved clay water absorption coefficient for both sintering temperatures. The higher pore diameter reveled by MIP at 1000°C probably due to coronas formed in CATT microstructure may improve A_c-value. Despite of this microstructural changing, CATT value is lower than CPER because its coronas remain isolated and less connected than CPER channels. Among all compositions, the one with sepiolite sand which has an intermediate granulometry when compared to sepiolite ultra fine and sepiolite gravel, exhibited the higher A_c-value suggesting that for sepiolite, absorbant grain size is not directly correlated to an interconnected microstructure.

Figure 4.8 illustrates the variation of the mass of the materials during time. The initial slope indicates that water is penetrating in the material. Once it reaches the top surface of the sample, the variation of mass becomes stable. The initial rate of water absorption (IR) represented by the values of suction rate in the first two minutes (Fig. 4.7b) and the total amount of water absorption (AW) are also reported in Fig. 4.7c. Both show a very good and positive correlation with A_c-value mainly IR. CSSA still has the higher IR and AW values, CLAY also presents very close IR and AW values for both sintering temperatures. CATT and CPER confirms the tendency of higher values of IR and AW at 1000°C however CVER presented high IR and AW but a low A_c-value. Moreover, for CSGR, IR and AW were higher at 800°C, contrary to A_c. CDIA and CMMT have a low IR but a high AW. CZEO presented a high IR but a low AW. An attempt to correlate A_c-value with open porosity, pore mean diameter and

specific surface area was made but it presented a very low statistical significance (Appendix D) confirming the complexity of water uptake phenomena in these materials.

Additionally, a cycling test with CATT, CPER and CLAY compositions sintered at 800°C was performed with a view of understanding materials behavior under different liquid/vapor solicitations. Samples were put in contact with water during 24h and then moved to an atmosphere with 57% of relative humidity without being in contact with water for 16h. Then samples were again put in contact with liquid water for 8h, successively changing from 16h with water contact and 8h with air contact. Fig.4.9 shows that all selected compositions presents a stable cycle with no significant changing in absorption and desorption capacity during time.

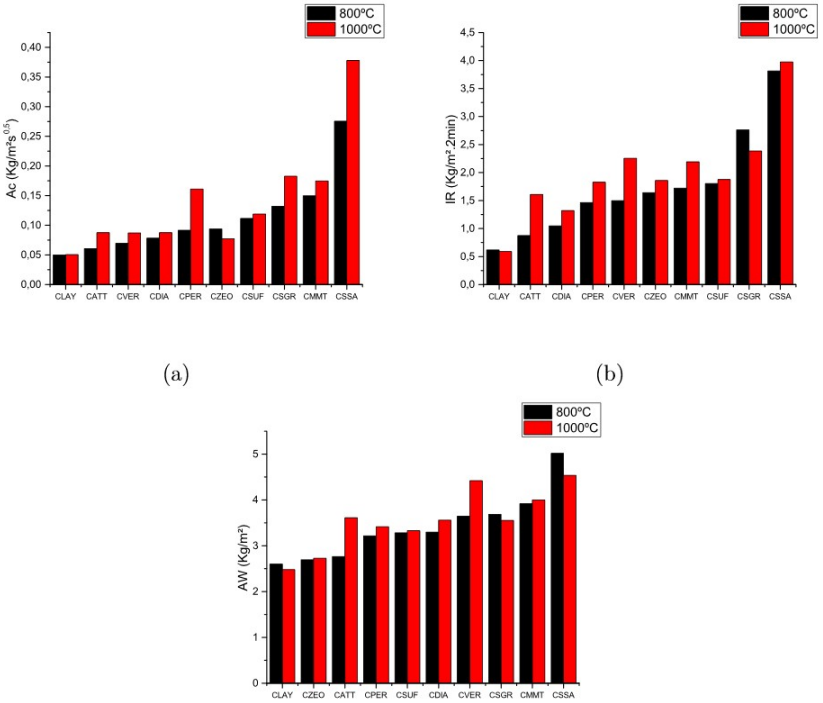

Figure 4.7: Absorption parameters for samples sintered at 800°C and 1000°C: (a) Water absorption coefficient (A_c) (b) Initial rate of absorption (IR) (c) Amount of water absorbed (AW).

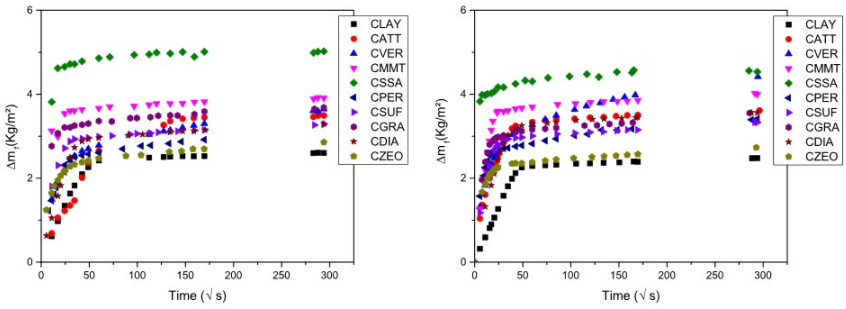

(a) (b)

Figure 4.8: Kinetic of water absorption for: (a) samples sintered at 800°C and (b) samples sintered at 1000°C.

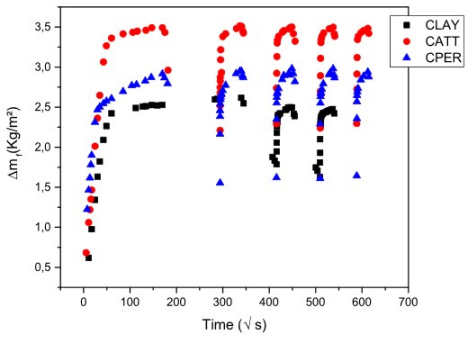

Figure 4.9: Water absorption/desorption cycling for three selected composition sintered at 800°C.

4.4.4 Thermal conductivity

Thermal conductivity depends on the firing temperature, density and therefore porosity of the samples [Sutcu 2015]. The thermal conductivity test results of the fired clay-based samples are presented in Fig. 4.10. Their thermal conductivities decrease when some absorbents are added to clay and increase with rising of the firing temperature confirming the findings of Demirboğa and Gül [2003] and Sutcu [2015] who studied the influence of perlite and vermiculite addition in bricks. At 800°C, all absorbents decreased λ-values of CLAY except for CZEO and

CSSA at 33% whereas at 75% CMMT, CATT, CVER and CPER diminished the heat flux of CLAY. At 1000°C, CMMT and CVER decreased λ-values of CLAY at 33% whereas at 75% CSGR and CVER diminished the heat flux of CLAY.

The effect of the different relative humidities on the thermal conductivity of the clay-based materials was additionally investigated. All compositions showed higher values of thermal conductivity at 75% RH than 33%. This result was expected since moisture conducts heat better than air. Also, comparing different firing temperatures, it can be seen that for most compositions, increasing firing temperature leads to an augmentation of the heat flux in samples mainly at 75%RH.

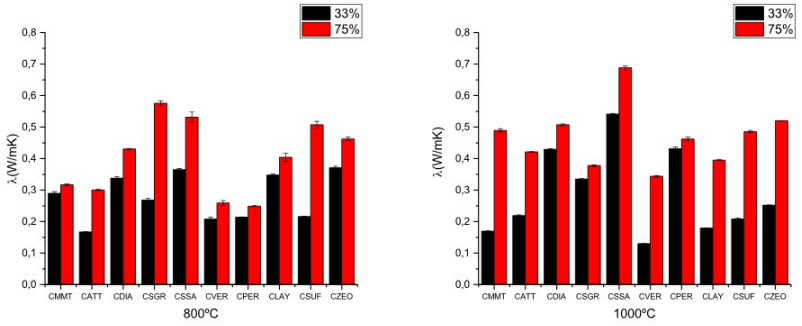

(a) (b)

Figure 4.10: Thermal conductivity at 33% and 75% of relative humidity for: (a) samples sintered at 800°C and (b) samples sintered at 1000°C.

Additionally, thermal effusivity has also been evaluated. Therefore, if a material has a good capacity of exchanging heat with surroundings, it will have a high value of effusivity and it will not be able to hold heat for a long time. Inversely, a low effusivity value indicates that the material can hold heat for a longer time. Figure 4.11 shows the values of effusivity at 33%RH and 75%RH. At 800°C and 33%RH, CZEO and CSSA that caused an increase in heat flux of clay, also raised effusivity. Same tendency is observed at 75%RH, since CMMT, CATT, CVER and CPER that dropped the λ-value of clay also decreased its effusivity. At 1000°C, sample capacity to exchange heat with surroundings improves alike thermal conductivity for both relative humidities. It is also observed a gain in effusivity when there is an increment in the relative humidity value at both firing temperatures. Oladunjoye and Sanuade [2012] found a positive correlation between the thermal effusivity and moisture in soils. This is due to the

fact that water can work as a bridge linking one grain soil to another which facilitates the heat conduction. Additionally, heat capacity of water is also much higher than the one for the air. However, the formation of microcracks and the tortuosity of the material can decrease the thermal conductivity of the material [Jougnot and Revil 2010].

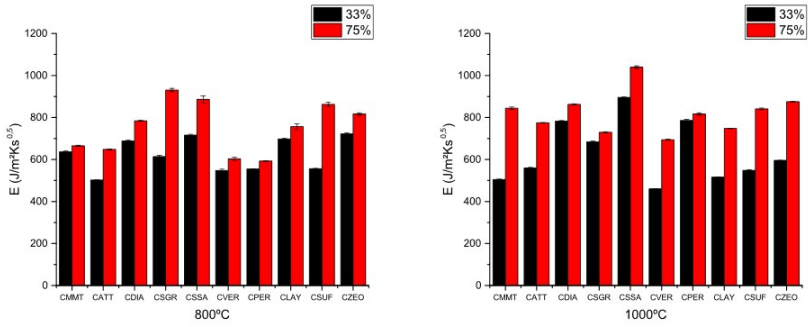

(a) (b)

Figure 4.11: Thermal effusivity at 33% and 75% of relative humidity for: (a) samples sintered at 800°C and (b) samples sintered at 1000°C.

4.5 Conclusions

This chapter has dealt with the hygrothermal characterization of fired earth materials produced by mixing mineral absorbents with clay at two sintering temperatures. The hygrothermal properties studied during this work were vapour sorption, water vapour permeability, water absorption coefficient, thermal conductivity and effusivity. The fired clay-based materials were also characterized from the physical and mineralogical points of view in the previous chapters.

The thermal results show that the incorporation of additives on fired clay and a sintering temperature of 800°C produces materials with low thermal conductivity that could be used as a construction material for insulating applications.

The hygrothermal characteristics measured on the samples are very close to each other and often close to the few data existing in the literature on fired earthen materials. The hygrothermal properties of the earth bricks confirmed their capacity to rapidly absorb a significant amount of water vapour and thus their capacity to participate to the regulation of the relative humidity of indoor air, especially because the fired clay has a very high permeability

to water vapour. The results of sorption experiments using the saturated salts solution method also highlighted this capacity.

Moreover, the present experimental study could be advantageously completed by the use of experimental data measured in models via hygrothermal software which is reported in the next chapter.

Chapter 5

Influence of the hygric performance of the innovative material on the indoor comfort

In this chapter, the influence of innovative materials on indoor climate is investigated. The moisture buffer value determined experimentally is used as input data to the numerical model which was implemented in the software SPARK. Results show that hygroscopic materials can effectively attenuate the variation of internal relative humidity thus improving hygrothermal comfort in a room.

Contents

5.1 Experimental measurements of Moisture buffer value (MBV) **127**

5.2 Numerical simulation **128**

5.2.1 Lumped capacity model 129

5.2.2 Case study 130

5.3 Results **132**

5.3.1 Moisture buffer value (MBV) 132

5.3.2 Numerical simulation 134

5.4 Conclusions **137**

5.1 Experimental measurements of Moisture buffer value (MBV)

Section 1.3.1 presented the concept of moisture buffering capacity. It can be understood as the ability of the material to absorb moisture when relative humidity is high and desorb moisture when relative humidity is low. This capacity has been extensively studied since 1980 [Rode 2005].

NORDTEST presented the definition of $MBV_{practical}$ as an attempt to approach real conditions of experiments. It takes into account the resistance when flow is in or out of the material during moisture transfer which is not considered in ideal conditions. $MBV_{practical}$ can be quantified by Eq.39:

$$MBV_{practical} = \frac{\Delta m}{A\Delta\varphi}, \tag{39}$$

where:

Δm variation of the mass of the sample during time [kg];

A area of the exposed surface [m^2];

$\Delta\varphi$ variation of the relative humidity level (between 33% and 75%).

To perform the MBV test, sides of samples were first sealed with aluminum tape to ensure that moisture transfer occurs through one surface of the sample. Then, they were preconditioned in small boxes at 30°C with NaBr salt solution which provides an atmosphere of 57% RH. When the variation of the mass of the samples is lower than 0.1%, equilibrium at 57% RH is reached and samples are moved to one of the RHBOX chambers (Fig.4.1) to start the test protocol. Specimens begin in the chamber at a 75% relative humidity provided by the NaCl salt solution. Therefore, material adsorbs moisture and in order to quantify it, samples are weighed each hour, during 8 hours. After this period, moisture desorption is started by moving samples to the chamber conditioned at 33% by the $MgCl_2$ salt solution for 16 hours. This 24-hour procedure is considered as a cycle and the combination of, at least, three stable cycles is needed for the calculation of MBV.

5.2 Numerical simulation

Predicting the hygrothermal behavior of different walls and even of a building, without going through long and costly experiments, can be done with the help of simulation tools. All the phenomena involved, heat transfer, diffusion and vapor effusion, liquid water transport, phase changes, make the modeling complex. Given this complexity and the interaction of the phenomena, the Annex 41 by the International Energy Agency[1] studied, validated and compared the main existing simulation models.

One of the goals of the Annex 41 was exploring the numerical tools which are available to perform building simulation taking into account heat, air and moisture transfer [Woloszyn and Rode 2008]. Table 5.1 shows some of the softwares tested.

A simplified model implemented in SPARK software[2] by Rahim [2015] was adopted in order to evidence the effect of moisture buffer capacity of materials in the attenuation of the relative humidity of a room. This model, based on "effective capacity" just take into account the experimental obtained moisture buffer value of the material. A lumped model is useful to simplify complex models.

To perform simulations, three compositions produced and characterized in the previous chapters were chosen: pure clay, clay with attapulgite and clay with perlite all sintered at 800°C. The selected materials were used as the wall component of a fictive room with the geometry of the BESTEST common exercise proposed during the Annex41.

The next section will detail the simulation tool chosen in this work.

[1] MOIST-ENG Subtask 1: Subtask 1 – Modelling Principles and Common Exercises `https://www.kuleuven.be/bwf/projects/annex41`

[2] SPARK – Simulation Problem Analysis and Research Kernel `https://simulationresearch.lbl.gov/VS/spark.html`

Table 5.1: Heat, air, moisture models. Adapted from Woloszyn and Rode [2008].

Software	Number of zones	Simplified (lumped capacity)/Detailed (1D HM)
BSIM	Multi-zone	Detailed
Delphin	1 zone	Detailed (1D/2D HM)
EnergyPlus	Multi-zone	Simplified or detailed (1D HM)
Domus	Multi-zone	Detailed
SPARK	Zonal model	Simplified
WUFI Plus	1 zone	Detailed

5.2.1 Lumped capacity model

The "effective capacity" model assumes that the moisture buffer capacity of the envelope is always in equilibrium with the internal psychometric conditions. This model makes it possible to evaluate the impact of hygroscopic materials and other parameters (such as ventilation rate, vapor source, exposure time, exposed surfaces, furniture, etc.) on the relative humidity variation using experimentally measured MBV values. It is established from the mass conservation equation which is written as follows [Vereecken *et al.* 2011]:

$$\left(\frac{V}{R_v T_i} + \frac{100V\overline{MBV}}{P_v(T_i)}\right)\frac{\partial P_{vi}}{\partial t} = (P_{ve} - P_{vi})\frac{n_v V}{3600 R_v T_i} + G_{vp}, \tag{40}$$

$$\overline{MBV} = \frac{\sum_k A_k MBV_k}{V}, \tag{41}$$

where:

MBV is the measured moisture buffer value $[kg/(m^2.\Delta\varphi)]$;

$\overline{MBV}$ is the normalized moisture buffer value $[kg/(m^3.\Delta\varphi)]$;

A_k is the exposed surface of the element k $[m^2]$;

V is the internal volume $[m^3]$;

T_i is the internal temperature $[K]$;

R_v is the gas constant for water vapor $[J/(kg.K)]$;

G_{vp} is the vapor source $[kg/s]$;

n_v is the ventilation rate $[1/h]$;

P_{ve} exterior partial vapor pressure $[Pa]$;

P_{vi} internal partial vapor pressure $[Pa]$;

P_v saturation vapor pressure $[Pa]$;

This model have been implemented in the Simulation Problem Analysis and Research Kernel (SPARK) simulation environment to evaluate the influence of the moisture buffer capacity on the internal relative humidity of the room, by using the experimental results of the materials studied in this work.

5.2.2 Case study

During the IEA Annex 41, an exercise was proposed with the intention of simulating a fictive room where moisture production periodically takes place. The effects of the porous material of the wall on the level of relative humidity of the room air are studied in this common exercise. The room, called here the BESTEST (Fig.5.1), is submitted to two basic cases of moisture perturbation (Fig.5.2). Both configurations are isothermal (T $= 20°\mathrm{C}$). There is a periodic moisture perturbation induced by the presence of an internal moisture gain (0.5 kg/h) between 9:00 and 17:00 every day corresponding to the occupation of two people and no other moisture gains are considered. External air enters the room at a constant rate of 0.5 air changes per hour. Outside and initial indoor vapor concentrations are set to 5.22 $g.m^{-3}$ (equivalent to 30% of relative humidity at $20°\mathrm{C}$). The external wall surface is impermeable. Case 1A considers an impermeable internal wall surface while case 1B includes the moisture transfer between the zone air and the envelope. Table 5.2 summarizes the conditions of each case. A semi analytical solution has been provided by Hagentoft *et al.* [2004]. Here this geometry with identical internal loads and ventilation system was used as base case. In order to investigate the impact of materials on the indoor climate, the original walls (concrete) are successively replaced by some of the elaborated innovative clay-based materials.

Table 5.2: Simulation input data of BESTEST case.

Case	V $[m^3]$	A $[m^3]$	T_i [°C]	T_{ext} [°C]	Moisture gain $[kg/h]$	Ventilation rate $[ach]$	φ_i [%]	MBV g/(m^2%φ)
1A	129.6	48	20	20	0.5	0.5	30	0
1B	129.6	48	20	20	0.5	0.5	30	>0

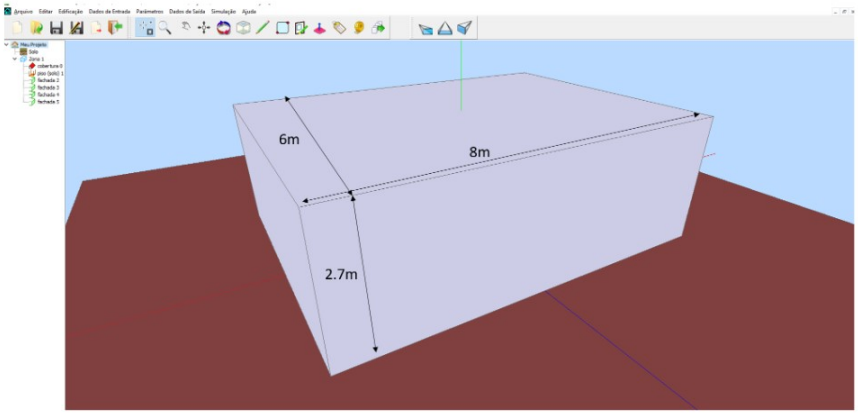

Figure 5.1: BESTEST building dimensions.

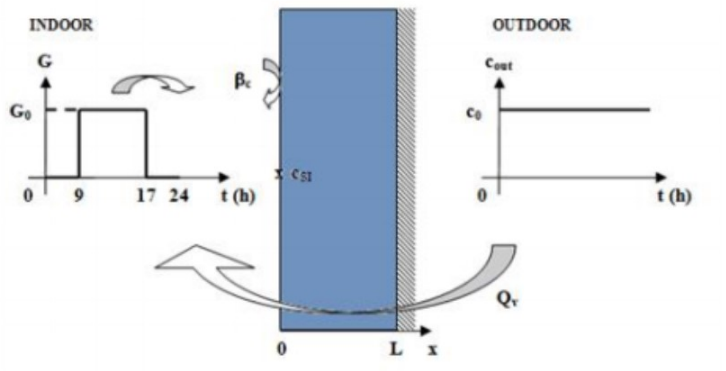

Figure 5.2: Schematic view of moisture perturbations.

5.3 Results

5.3.1 Moisture buffer value (MBV)

Figure 5.3 shows the mass variations of samples during cycles of MBV test. Samples showed stability in cycles after 200h of test thus mass variation and MBV value reported were calculated after this period of time. In addition, to reach 200h it is necessary to cross a weekend and as the building is closed on weekends it is not possible to cycle the material during those days. Compositions sintered at 800°C exhibit a different behavior with time compared to compositions sintered at 1000°C. As it was reveled by Fig. 5.4, lower firing temperatures increase the MBV value and this tendency is confirmed in (Fig. 5.3a). At 800°C samples show a similar behavior except for CATT that adsorbs and desorbs humidity faster than other compositions. This may justify its high MBV value. At 1000°C (Fig. 5.3b) compositions appear to be more outspread. Most additives are very much affected by this temperature, slowing clay buffer performance.

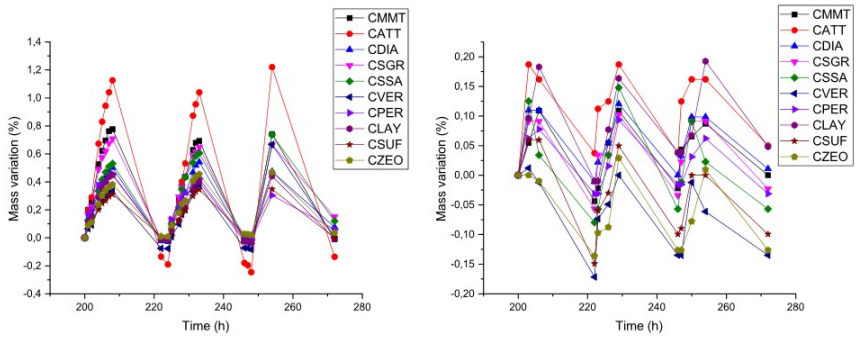

(a) (b)

Figure 5.3: Mass variations during MBV test for: (a) samples sintered at 800°C and (b) samples sintered at 1000°C.

Besides the kinetic of MBV experiment aforementioned, the practical moisture buffer value for clay and developed materials was evaluated. Figure 5.4 shows that compositions with attapulgite, sepiolite sand, sepiolite gravel, montmorillonite and zeolite sintered at 800°C increased clay MBV value; other absorbents maintained clay value except for the composition with perlite which decreased the moisture sorption capacity of clay. At 1000°C, all values are quite equivalent considering error bars which depict standard deviation.

According to the classification [Rode 2005], at 800°C,CATT has an excellent moisture buffer performance, CMMT, CSSA, CSGR, CZEO, CLAY and CDIA exhibit a good performance while CSUF, CVER and CPER have a moderate MBV. Considering samples sintered at 1000°C, all exhibit a limited/poor moisture buffer performance. As expected, the excellent performance of CATT fired at 800°C in the MBV test is resultant of its sorption curves (Fig. 4.5b) which demonstrate the good moisture adsorption/desorption capacity in the range of 33 and 75%RH. It is interesting to note that some materials have good sorption capacity above 75%RH but it is not reflected in the MBV test since it is limited to the range of 33 and 75%RH.

Comparing to materials tested during NORDTEST protocol, fired clay-based materials proposed in this work considerably improved the reported fired clay MBV value ($0.4 g/m^2\%\varphi$). Samples sintered at 800°C presented MBV value superior even to some unfired clays ($1.13 g/m^2\%\varphi$) [McGregor *et al.* 2014b] making them suitable to be used as moisture buffer materials.

In the case of CATT and CPER, microstructure plays an important role. The mesopores formed in the CATT structure and the increased specific surface area boost the buffering performance. Larger pores and the elongated secondary porosity of CPER microstructure did not favor the moisture adsorption/desorption. The dramatic diminution in the MBV value at 1000°C also agrees with microstructural changes due to sintering process. The observed increase of CPER pore size at 1000°C, mainly owed to the expansion of secondary porosity, seems to decrease buffer performance.

Correlating grain size of sepiolite with moisture buffer capacity, it can be seen that finer particles (CSSA) improved clay performance as much as coarser grain size (CSGR). Moreover, CSUF did not appear to considerably improve sorption capacity. Therefore, in this case, a correlation with sepiolite grain size and sorption capacity cannot be performed. This is probably due to microstructural changes occurred during sintering process. This tendency is observed at both sintering temperatures.

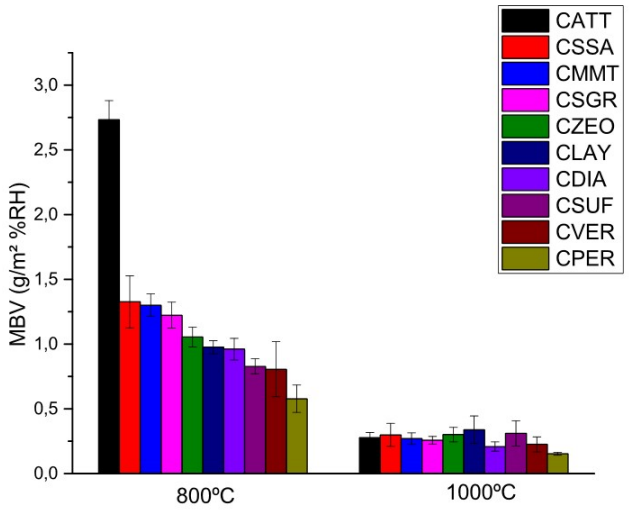

Figure 5.4: Moisture buffer value calculated for samples sintered at 800°C and at 1000°C.

5.3.2 Numerical simulation

5.3.2.1 Preliminary validation

In order to gain confidence in model results, numerical simulations are tested against analytical solutions. The first test considers that there is no hygric inertia in the walls that means the material is impermeable. Occupants, which means vapor generation, and ventilation are taken into account. Figure 5.5 shows that the adopted model agree with the analytical solution proposed by Hagentoft *et al.* [2004].

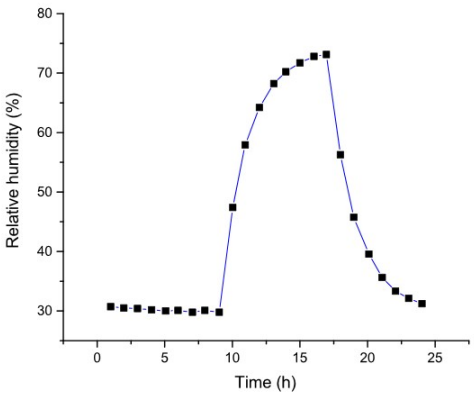

Figure 5.5: Relative humidity variation in the room when there is no hygric inertia (MBV=0) with vapor generation and ventilation (first case). Dots represent the analytical solution and straight line corresponds to SPARK simplified model results.

5.3.2.2 Effect of proposed materials

Second test case analyses the effect of the walls hygric inertia on the variation of the internal humidity in the room. It investigates the influence of the different moisture buffer values on the amplitude of variation of the room relative humidity.

Indeed, as it can be seen in Fig. 5.6, in the case of the room with walls without hygric inertia (MBV = 0), the maximum value of the relative humidity is 72% with an amplitude of 42% according to SPARK. The material produced with clay and perlite ($MBV = 0.58g/m^2\%\varphi$), has the maximum humidity of 69% with an amplitude of 39%. The material produced only with clay ($MBV = 0.97g/m^2\%\varphi$), has the maximum humidity of 65% with an amplitude of 30%. The material produced with clay and attapulgite ($MBV = 2.77g/m^2\%\varphi$), the maximum humidity of only 55% with an amplitude of 15%.

Comparing the three developed materials with other building materials in NORDTEST protocol, such as brick ($MBV = 0.41g/m^2\%\varphi$) and concrete ($MBV = 0.35g/m^2\%\varphi$), underlines the better hygric performance of CPER, CLAY and CATT.

The increase on the MBV value thus makes it possible to attenuate the variation of relative humidity inside the room.

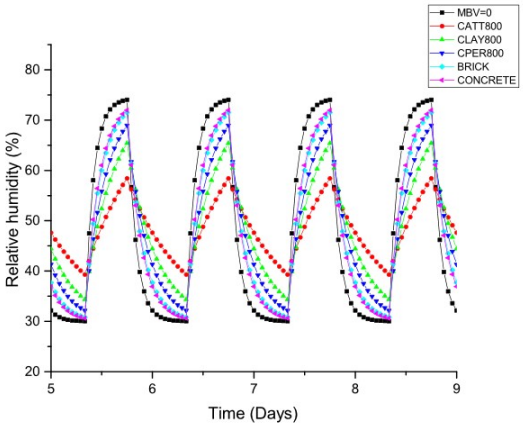

Figure 5.6: Influence of the adsorption/desorption effect on the internal relative humidity.

Aiming to compare the moisture control capacity of room materials, Rahim [2015] defines a coefficient $A/A0$ which represents the ratio of the amplitude of variation of the internal relative humidity of the room with and without taking into account the buffer capacity (A<A0). A low A/A0 ratio represents better comfort. In this work, we propose Eq. 42 based on Rahim [2015] coefficient to see directly the reduction of RH amplitude (R_A).

$$R_A = \left(1 - \frac{A}{A_0}\right) 100. \tag{42}$$

Due to the high buffer capacity, the $A/A0$ values are much lower for the composition with attapulgite than for clay or the composition with perlite. According to numerical simulations (Fig. 5.7), comparing produced materials with the case of the impermeable walls (MBV = 0), amplitude can be reduced using CATT material in the wall by 57%, whereas for CLAY, 23% and for CPER, 11%.

These numerical simulation results show that the materials studied (CATT, CLAY and CPER) enable to considerably improve the hygrothermal comfort in the room. In terms of hygric inertia, the results obtained with the composition with attapulgite is better than those of traditional materials and the one with perlite addition.

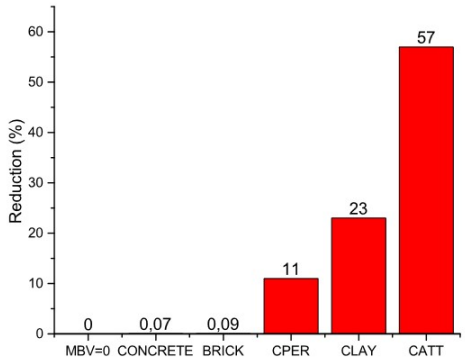

Figure 5.7: Indoor RH amplitude reduction for materials with different MBV.

Considering cities with high values of relative humidity or environments with high moisture production rates, the reduction of the RH amplitude due to moisture buffer effect may be even more evident. This can be an interesting solution to improve hygrothermal comfort or to avoid the use of dehumidifiers in places such as museums and libraries.

5.4 Conclusions

The measured hygrothermal parameters of the fired earthen building materials were described in the previous chapter. However, some properties such as sorption isotherms are operated in static mode, waiting for the steady state to be achieved at each step of increasing (or decreasing) RH. Such test gave interesting information on the physical properties of the porous media but did not permit to estimate the real evolution of relative humidity. Therefore, to analyze the dynamic behaviour of water vapour sorption/desorption the NORDTEST protocol is used and the obtained MBV compared with that of other building materials, considered as conventional, proving that some of the novel fired clayey materials have good and excellent response to daily variations of relative humidity.

Three new compositions with measured MBV values (CATT, CPER and CLAY with 2.77, 0.58 and 0.97 $g/m^2\%\varphi$, respectively), were further chosen to perform a numerical simulation in order to investigate their effect on indoor environment.

The reduction of the relative humidity amplitude due to moisture buffer capacity of the produced materials (CATT, CPER and CLAY) was simulated at the level of a monozone local using the SPARK simplified model. This method uses the experimental MBV value as input data.

Considering a scenario without HVAC system at the level of a monozone local, the numerical simulations show that the CATT significantly dumps the amplitude of relative humidity fluctuations demonstrating that the fired earthen materials with the addition of absorbents have a better moisture buffering performance comparing to the clay without any addition. It shows that although CATT behavior was not fundamentally different from the other samples with respect to equilibrium properties, its buffer capacity is significantly higher than the others.

Conclusions and recommendations

The main objective of this work as stated at the beginning of the manuscript is the development of a clay-based material with high hygroscopic performance for moisture buffer applications in buildings.

Fired clay is a traditional building material. To improve the humidity-controlling properties of fired clay, it was prepared a new type of humidity-controlling composite using high absorbents.

The methodology can be divided into two main phases:

I. Evaluation of the nature of absorbents and their proportion when added to clay and the influence of sintering conditions on physical and mechanical properties of materials. In this specification, different absorbents were selected and particular attention has been paid to attapulgite, perlite, sepiolite, vermiculite, diatomite, zeolite and montmorillonite. This choice of aggregates is justified by their high availability in metropolitan France and Brazil but also by their promising hygrothermal performance in terms of the comfort they provide the occupants when they are incorporated to a very common building material: fired clay. In addition, based on a bibliographic research and the mechanical limit of the sample, three absorbent proportions were tested: 5, 10 and 20%. Beyond 20% samples were extremely brittle. Finally, aiming to ally good mechanical behavior with hygic performance, three sintering temperatures were selected: 800, 900 and 1000°C.

II. Once the best conditions and formulation were selected, deeper microstructural and hygrothermal characterizations were performed. The entire range of pore size distribution was obtained using two different techniques: BET (at a nanoscale) and MIP (at a meso and macroscale). A general panorama of sample microstructure was attained with also at different scales: using optical and scanning electronic microscopy. Complementary, a

quantification of geometric parameters of sample microstructure was performed with the help of a software. Compositions had additionally their phases identified x-ray diffraction. Concerning hygrothermal behavior, sorption isotherms, water vapor diffusion, thermal conductivity and liquid absorption were evaluated.

Concerning the influence of aggregates nature and proportion on physical properties of fired clay, it was found that the bulk density of fired clay decreased with increasing proportion of additives. On the other hand, their porosity and water absorption values increased. Bending strength values diminished with increasing vermiculite/perlite additive proportion on clay.

Regarding sintering temperature effect on physical properties, the temperature of 800°C presented the higher values of porosity as well as 20% wt of absorbents on clay. Firing temperature of 1000°C exhibited the best values of mechanical properties. Therefore, both temperatures (800°C and 1000°C) and absorbent proportion (20%) were chosen to be deeply investigated respecting microstructure and hygrothermal characterization.

Microstructural characterization showed that: the addition of attapulgite generated secondary porosity in the form of coronas around the particles. Comparing materials sintered at 800 and at 1000°C, there is an increase in area and quantity of these coronas. In the sample with perlite addition, a secondary porosity was generated in the form of channels, which increased in size and width with the increase of firing temperature, forming a network with high connectivity.

The generation of the secondary porosity can be compared with the mercury porosimetry data. The increased interconnectivity of secondary porosity in the samples with perlite at 1000°C may explain the increase in pore size showed by the porosimetry test. In the sample with attapulgite, although the increase in secondary porosity at 1000°C is clearly observed in the pore group of greater size, the measured porosity is lower compared to one obtained by the addition of perlite at the same temperature. This behavior is due to the fact that this porosity remains isolated.

Indeed, these microstructural characteristics can be related to hygrothermal performance. Water sorption isotherms revealed that CPER has a better water adsorption behavior at high relative humidity levels than CATT due to pores with wider diameter. Also water absorption coefficient results confirmed this statement since the A_c-value of CPER is higher than CATT's. This fact proves that the isolated coronas and less connected microstructure of CATT do not favor water absorption as much as CPER channels. This microstructural characteristic is the same reason that the water vapor permeability value of CATT is lower than CPER. Also,

increasing sintering temperature, improved water vapor diffusion since channels and coronas increased as well. Same behavior is found for thermal conductivity: CPER and CATT values increased with sintering temperature. CPER conductivity is also higher than CATT's.

Phase composition through XRD can be related to sintering conditions and thus to moisture buffer values. It showed that there was variation of phases with the firing of the material. Attapulgite granules, initially formed by palygorskite, lizardite, muscovite and quartz are partially amorphized and the remaining minerals re-equilibrate. Paligorskite and lizardite disappear. Paligorskite is a mineral with high natural porosity and sorption capacity, hence, its disappearance or rebalancing for other mineral phases leads to a decrease in the primary porosity of the material affecting the moisture buffer performance. The amorphization observed in the diffraction occurs due the partial melting of the material, as observed in optical and electronic microscopy. Perlite granules showed evidence of partial melting and decreased internal porosity when sintered at $1000°\mathrm{C}$.

Pore size distribution and the generation of the secondary porosity can also be compared with mechanical results. The pores of greater size of the composition with perlite significantly weakened the material as well as the interconnectivity of secondary porosity in the samples. On the other hand, a higher sintering temperature increased the bending strength.

Finally, the evaluation of the effect of the Moisture Buffer Value (MBV) on the variation of the internal humidity of a room was taken into account through a numerical simulation. This coefficient makes possible not only to compare the potentialities of the materials with respect to their buffering capacity, but also to identify a classification of the materials with respect to vapor storage. This final part, reveals the capacity of the innovative clay-based materials in attenuating relative humidity of indoor spaces thus improving hygrothermal comfort.

Thus, the work carried out during this thesis opens up numerous perspectives for a more in-depth investigation of clay-based materials, such as:

I. Use a more in-depth microstructural study to better understand the impact of internal arrangements on these performances;

II. Complement experimental characterizations, in particular, determine the permeability to water vapor under several humidity conditions;

III. Complete the study on a larger scale with a real prototype;

IV. Extend the numerical study of the hygrothermal behavior of a monozone room to the scale of a building with various exterior and interior conditions.

Synthèse

L'excès d'humidité affecte considérablement les performances des bâtiments, causant de nombreux problèmes, tels que la faible durabilité des matériaux, la croissance des moisissures, l'inconfort, les allergies et les maladies respiratoires. Pour contrer ces effets et stabiliser le niveau d'humidité dans l'environnement, les systèmes de chauffage, de ventilation et de climatisation (CVC) sont souvent utilisés.

Selon le Bulletin énergétique brésilien [1], 46% de la consommation d'électricité au Brésil est attribuée aux bâtiments résidentiels, commerciaux et publics. Compte tenu des bâtiments commerciaux, 30% de l'énergie consommée est principalement due aux systèmes CVC qui ont un impact direct sur les coûts du fonctionnement d'un bâtiment et un impact indirect sur l'environnement, ce qui révèle le besoin urgent d'une amélioration rapide des produits éconergétiques et l'importance des projets associés à la matière énergétique dans le contexte brésilien. En France, un programme important de "construction à faible impact environnemental" a été mis en place pour la rénovation d'environ 25 millions d'habitations et l'amélioration de la performance de 3 millions d'habitations supplémentaires d'ici 2020 [2].

En réponse à ces préoccupations, une recherche sur le développement de matériaux pour l'amélioration de la performance hygrothermique et énergétique des bâtiments est réalisée. Ce nouveau matériau profiterait de la capacité des matériaux naturels poreux à adsorber/désorber l'humidité et pourrait être utilisé pour réduire les températures de la surface du toit et atténuer la variation de l'humidité relative dans des environnements comme les musées et les bibliothèques réduisant ainsi l'utilisation des systèmes de clima-

1. https://ben.epe.gov.br
2. https://www.ecologique-solidaire.gouv.fr

tisation.

Sachant que les matériaux de construction en terre cuite sont parmi les matériaux les plus anciens dans le monde en plus d'être polyvalents, l'objectif de ce travail est d'améliorer leur capacité à adsorber/désorber l'humidité en modifiant la structure poreuse de ces matériaux. Cet objetive est atteint en rajoutant des absorbants à la structure de l'argile.

Les matériaux avec une meilleure performance à l'adsorption/desorption d'humidité, ont été sélectionnés dans le cadre d'une simulation hygrothermique (avec le logiciel de transfert de masse et d'humidité Spark) pour vérifier l'effet tampon dans l'atténuation de l'humidité dans les bâtiments.

Production des matériaux et caractérisation physique

Dans la préparation d'un matériau hautement absorbant par processus de frittage, l'argile est mélangée avec différents matériaux absorbants (attapulgite, diatomite, sépiolite, vermiculite, perlite, montmorillonite et zéolite). Ceux ci sont principalement vendus comme absorbants industriels pour les liquides. La sépiolite est utilisée dans trois différentes tailles de particules. L'attapulgite provient d'Eurosorb en France, la diatomite, la sépiolite et la montmorillonite sont commercialisés par Textiles Essuyages en France et la perlite et la vermiculite par le jardinage Boutin au Brésil. La zéolite provient de la société Tosoh. L'argile a été fourni par une société de carreaux et de briques située à Curitiba, au Brésil.

L'élaboration du corps céramique a été effectuée en mélangeant différentes proportions d'additifs à l'argile (5, 10 et 20% en poids) et de l'eau a été ajoutée pour conférer une bonne plasticité en fonction de la quantité utilisée d'additifs. Les échantillons ont été placés dans un moule en silicone de 60 mm X 20 mm X 10 mm et y sont restés pendant 48 heures à température ambiante pour sécher naturellement. Ils ont été ensuite séchés à 105 °C pendant 24h et puis frités dans un four à trois températures différentes (800°C, 900°C et 1000°C) pendant 1h après une montée en témperature à 10°C/min.

Ensuite, l'influence du pourcentage (% d'absorbants dans l'argile) sur les propriétés mécaniques et physiques a été testée pour la vermiculite et de perlite. Leur température de frittage, leurs propriétés physiques et mécaniques ont été étudiées.

Les résultats obtenus montrent que la densité apparente de l'argile cuite a diminué

avec l'augmentation de la quantité de vermiculite/perlite, tandis que la porosité et l'absorption d'eau ont augmenté. L'addition de sepiolite, de diatomite, de montmorillonite et de zéolite a également montré le même comportement. La de résistance à la flexion a diminué avec l'augmentation de la proportion d'additif de vermiculite/perlite sur l'argile. L'augmentation de la température de cuisson a affecté les propriétés des matériaux à base d'argile, en augmentant leur résistance mécanique, en plus de diminuer leurs porosités. La température de 800°C et un taux de 20% en poids d'absorbant conduisent à des valeurs de porosité supérieures. La température de cuisson de 1000°C a montré les meilleures valeurs de propriétés mécaniques. Par conséquent, les températures et la nature des absorbants sont les paramètres qui ont été choisis pour être étudiés dans les chapitres suivants portant sur la microstructure et la caractérisation hygrothermique.

Caractérisation microstructurale des composites à base d'argile cuite

Afin de comprendre l'influence de la microstructure sur les propriétés hygrothermiques des matériaux produits, trois compositions ont été sélectionnés : la composition avec de l'attapulgite qui présentait de très bonnes propriétés hygrothermiques et physiques, l'échantillon avec de la perlite qui n'a pas été excellent dans les tests hygriques et le matériau de base : l'argile pure.

Les matériaux ont été caractérisés par microscopie optique et microscopie électronique à balayage, et diffraction des rayons-X. Ensuite, une quantification des paramètres géométriques de la microstructure des échantillons est effectuée à l'aide d'un logiciel d'analyses d'image.

L'observation des textures de l'argile pure par microscopie optique et électronique a montré qu'il n'y avait pas de génération de porosité secondaire avec la température de cuisson. L'ajout d'attapulgite a généré une porosité secondaire sous forme de coronas autour des particules. En comparant les matériaux frittés à 800 et à 1000°C, il y a une augmentation de la superficie et de la quantité de ces coronas. La forme corona, circulaire mais isolée, agira comme une porosité fermée. Dans l'échantillon avec addition de perlite, une porosité secondaire a été générée sous la forme de canaux, qui ont augmenté en taille et en largeur avec l'augmentation de la température de cuisson, formant un réseau à haute connectivité.

L'étude minéralogique par XRD a montré qu'il y avait une variation de phases avec

la température de cuisson du matériau. Les grains d'attapulgite, initialement formés de palygorskite, lizardite, muscovite et quartz sont partiellement amorphisés et les minéraux restants se rééquilibrent. Paligorskite et lizardite disparaissent. À 800°C il y a encore des pics de muscovite, de quartz et d'enstatite. À 1000°C, les pics de quartz et d'enstatite prédominent. La paligorskite est un minéral à forte porosité naturelle et capacité de sorption, par conséquent, sa disparition ou son rééquilibrage pour d'autres phases minérales entraîne une diminution de la porosité primaire du matériau. L'amorphisation observée en diffraction se produit en raison de la fusion partielle du matériau, observée en microscopie optique et électronique. Les grains de perlite ont montré une fusion partielle et une diminution de la porosité interne lorsqu'ils étaient frittés à 1000°C.

La génération de la porosité secondaire peut être comparée aux données de porosimétrie au mercure. L'interconnectivité accrue de la porosité secondaire dans les échantillons avec de la perlite à 1000°C peut expliquer l'augmentation de la taille des pores montrée par le test de porosimétrie. Dans l'échantillon avec attapulgite, bien que l'augmentation de la porosité secondaire à 1000°C soit clairement observée dans le groupe des pores de plus grande taille, la porosité mesurée est inférieure à celle obtenue par addition de perlite à la même température. Ce comportement est dû au fait que cette porosité reste isolée.

La distribution de la taille des pores et la génération de la porosité secondaire peuvent être comparées aux résultats mécaniques. Les pores de plus grande taille de la composition avec la perlite ont considérablement affaibli le matériau ainsi que l'interconnectivité de la porosité secondaire dans les échantillons. D'autre part, une température de frittage plus élevée a augmenté la résistance à la flexion.

Propriétés hygrothermiques des composites céramiques à base d'argile cuite

Le comportement hygrique est analysé en fonction des isothermes de sorption, de la perméabilité à la vapeur d'eau, de la valeur tampon d'humidité et du coefficient d'absorption d'eau. Le comportement thermique n'a été étudié par une mesure directe de la conductivité thermique.

Les résultats thermiques ont montré que l'incorporation d'additifs sur l'argile cuite et une température de frittage de 800°C produisent des matériaux avec une faible conductivité thermique qui pourraient être utilisé comme matériau de construction pour les applications d'isolation.

Les caractéristiques hygrothermiques mesurées sur les échantillons ont confirmé leur capacité à absorber rapidement une quantité importante de vapeur d'eau et donc leur capacité à réguler l'humidité relative de l'air intérieur, en particulier parce que le matériau absorbant a une importante perméabilité à la vapeur d'eau. Les résultats des expériences de sorption utilisant la méthode de la solution de sels saturés mettent aussi en évidence leur très bonne régulation de l'humidité. Le comportement dynamique de la sorption/désorption de la vapeur d'eau exprimé par le protocole NORDTEST a été utilisé et le MBV obtenu comparé à celui des autres matériaux de construction considérés comme conventionnels prouvent que certains des nouveaux matériaux argileux cuits ont une bonne voire excellente réponse aux variations quotidiennes de humidité relative. Le coefficient d'absorption d'eau a également révelé une bonne capacité d'absorption d'eau liquide par les échantillons produits.

Simulation de la performance hygrique du matériau innovant

L'influence de l'inertie hygroscopique des matériaux produits sur le niveau d'humidité relative intérieure a été faite à l'aide d'un modèle numérique utilisé par le logiciel qui effectue la simulation hygrothermique.

Les résultats de la méthode de simulation montre que les matériaux hygroscopiques peuvent atténuer efficacement la variation d'humidité relative intérieure, améliorant ainsi le confort hygrothermique dans une pièce.

Pour conclure, le travail effectué au cours de cette thèse contribue au développement de nouveaux matériaux hygroscopiques et à une nouvelle utilisation de l'argile cuite comme matériau absorbant d'humidité. De plus, les caractérisations effectuées apportent une meilleure compréhension de l'influence de la microstructure dans les propriétés hygrothermiques permettant l'amélioration de ces dernières. Ainsi, cette recherche ouvre de nombreuses perspectives pour une étude plus approfondie de ces matériaux à base d'argile en collaborant avec la performance hygrothermique et énergétique de l'habitat.

Bibliography

[**Abadie *et al.* 2009**] Abadie, M. O. and Mendonça, K. C. (2009). "Moisture performance of building materials: From material characterization to building simulation using the Moisture Buffer Value concept". *Building and Environment,* 44 (2), pp. 388–401 (cit. on p. 11).

[**ADEME 2011**] ADEME (2011). "Agence de l'environnement et de la maîtrise de l'énergie and Ministère de l'Écologie, du Développement durable, des Transports et du Logement - Réeglementation thermique 2012: un saut énergétique pour les bâtiments neufs". Accessed: 2017-08-17. URL: `http://www.cohesion-territoires.gouv.fr/IMG/pdf/rt2012__saut_energetique_batiments_neufs__avril11.pdf` (cit. on pp. 8, 9).

[**ADEME 2017**] ADEME (2017). "Bâtiment". Accessed: 2017-08-17. URL: `http://www.ademe.fr/expertises/batiment` (cit. on p. 1).

[**Allinson *et al.* 2010**] Allinson, D. and Hall, M. (2010). "Hygrothermal analysis of a stabilised rammed earth test building in the UK". *Energy and Buildings,* 42 (6), pp. 845–852 (cit. on p. 12).

[**Alver *et al.* 2012**] Alver, E. and Metin, A. Ü. (2012). "Anionic dye removal from aqueous solutions using modified zeolite: Adsorption kinetics and isotherm studies". *Chemical Engineering Journal,* 200, pp. 59–67 (cit. on p. 53).

[**Alves *et al.* 2016**] Alves, H. P., Silva, J. B., Campos, L. F., Torres, S. M., Dutra, R. P., and Macedo, D. A. (2016). "Preparation of mullite based ceramics from clay–kaolin waste mixtures". *Ceramics International,* 42 (16), pp. 19086–19090 (cit. on p. 34).

[**Aouba *et al.* 2016**] Aouba, L., Bories, C., Coutand, M., Perrin, B., and Lemercier, H. (2016). "Properties of fired clay bricks with incorporated biomasses: cases of olive stone flour and wheat straw residues". *Construction and Building Materials,* 102, pp. 7–13 (cit. on p. 99).

[**Aras 2004**] Aras, A. (2004). "The change of phase composition in kaolinite-and illite-rich clay-based ceramic bodies". *Applied Clay Science,* 24 (3), pp. 257–269 (cit. on p. 50).

[**Arens *et al.* 1996**] Arens, E. A. and Baughman, A (1996). "Indoor humidity and human health: part II–buildings and their systems". *ASHRAE Transactions,* 102 (cit. on p. 9).

[**Arrigoni *et al.* 2017**] Arrigoni, A., Grillet, A.-C., Pelosato, R., Dotelli, G., Beckett, C. T., Woloszyn, M., and Ciancio, D. (2017). "Reduction of rammed earth's hygroscopic performance under stabilisation: an experimental investigation". *Building and Environment,* 115, pp. 358–367 (cit. on p. 32).

[**Ashour *et al.* 2011**] Ashour, T., Georg, H., and Wu, W. (2011). "An experimental investigation on equilibrium moisture content of earth plaster with natural reinforcement fibres for straw bale buildings". *Applied thermal engineering,* 31 (2), pp. 293–303 (cit. on p. 12).

[**Baccour *et al.* 2009**] Baccour, H, Medhioub, M, Jamoussi, F, and Mhiri, T (2009). "Influence of firing temperature on the ceramic properties of Triassic clays from Tunisia". *Journal of materials processing technology,* 209 (6), pp. 2812–2817 (cit. on p. 34).

[**Baraldi**] Baraldi, L. *World production and consumption of ceramic tiles.* `http://www.tiledizioni.it/documenti`. Accessed: 2017-06-16 (cit. on p. 13).

[**Baughman *et al.* 1996**] Baughman, A and Arens, E. A. (1996). "Indoor humidity and human health–Part I: Literature review of health effects of humidity-influenced indoor pollutants". *ASHRAE Transactions,* 102 (cit. on p. 9).

[**Berre 1989**] Berre, P. L. (1989). *Les attapulgites (palygorskites) et sépiolites* (cit. on pp. 48, 49).

[**Bomberg *et al.* 2005**] Bomberg, M., Pazera, M., and Plagge, R. (2005). "Analysis of selected water absorption coefficient measurements". *Journal of Thermal Envelope and Building Science,* 28 (3), pp. 227–243 (cit. on p. 118).

[**Bories *et al.* 2014**] Bories, C., Borredon, M.-E., Vedrenne, E., and Vilarem, G. (2014). "Development of eco-friendly porous fired clay bricks using pore-forming agents: A review". *Journal of environmental management,* 143, pp. 186–196 (cit. on pp. 33, 59).

[**Bruijn *et al.* 2013**] Bruijn, P. de and Johansson, P. (2013). "Moisture fixation and thermal properties of lime–hemp concrete". *Construction and Building Materials,* 47, pp. 1235–1242 (cit. on p. 12).

[**Brunauer *et al.* 1938**] Brunauer, S., Emmett, P. H., and Teller, E. (1938). "Adsorption of gases in multimolecular layers". *Journal of the American Chemical Society,* 60 (2), pp. 309–319 (cit. on pp. 18, 71, 72).

[**BS5250 1989**] BS5250 (1989). "British Standard Code of practice for Control of condensation in buildings". *British Standards Institution,* (cit. on p. 110).

[**Calle *et al.* 1988**] Calle, C. de la and Suquet, H. (1988). "Vermiculite". *Reviews in Mineralogy and Geochemistry,* 19 (1), pp. 455–496 (cit. on p. 47).

[**CBIE 2014**] CBIE (2014). "Selo PROCEL edificações". *Centro brasileiro de informação energética,* Accessed: 2017-07-21. URL: `http://www.procelinfo.com.br/data/documents/storedDocuments/%7BEB3DAE90-58CB-48BF-86E9-1CA876F683B0%7D/%7BA5253934-4245-465E-8112-B9DF90649647%7D/R5.jpg` (cit. on p. 9).

[**Ceramics**] Ceramics, B. T. *Breviary Technical Ceramics.* `http://www.keramverband.de/brevier_engl/4/1/4_1_4.htm`. Accessed: 2017-03-17 (cit. on p. 43).

[**Cerolini *et al.* 2009**] Cerolini, S, D'Orazio, M, Di Perna, C, and Stazi, A (2009). "Moisture buffering capacity of highly absorbing materials". *Energy and Buildings,* 41 (2), pp. 164–168 (cit. on pp. 13, 30).

[**Chemkhi *et al.* 2004**] Chemkhi, S., Zagrouba, F., and Bellagi, A. (2004). "Thermodynamics of water sorption in clay". *Desalination,* 166, pp. 393–399 (cit. on p. 114).

[**Chen *et al.* 2004**] Chen, H, Deng, S, Bruner, H, and Garcia, J (2004). "Roots of mold problems and humidity control measures in institutional buildings with pre-existing mold condition" (cit. on p. 9).

[**Collet *et al.* 2008**] Collet, F., Bart, M., Serres, L., and Miriel, J. (2008). "Porous structure and water vapour sorption of hemp-based materials". *Construction and building materials,* 22 (6), pp. 1271–1280 (cit. on p. 12).

[**Collet *et al.* 2011**] Collet, F., Achchaq, F., Djellab, K., Marmoret, L., and Beji, H. (2011). "Water vapor properties of two hemp wools manufactured with different treatments". *Construction and Building Materials,* 25 (2), pp. 1079–1085 (cit. on p. 12).

[**Cultrone *et al.* 2004**] Cultrone, G., Sebastián, E., Elert, K., Torre, M. J. la, Cazalla, O., and Rodriguez-Navarro, C. (2004). "Influence of mineralogy and firing temperature on the porosity of bricks". *Journal of the European Ceramic Society,* 24 (3), pp. 547–564 (cit. on p. 34).

[**Cultrone *et al.* 2005**] Cultrone, G., Sebastian, E., and De La Torre, M. (2005). "Mineralogical and physical behaviour of solid bricks with additives". *Construction and Building Materials,* 19 (1), pp. 39–48 (cit. on p. 61).

[**Daly *et al.* 2012**] Daly, P., Ronchetti, P., and Woolley, T. (2012). "Hemp Lime Bio-composite as a Building Material in Irish Construction" (cit. on p. 12).

[**Deer *et al.* 1992**] Deer, W. A., Howie, R. A., Zussman, J., *et al.* (1992). *An introduction to the rock-forming minerals.* Vol. 2. Longman Scientific & Technical Hong Kong (cit. on p. 50).

[**Delgado *et al.* 2006**] Delgado, J., Ramos, N., and De Freitas, V. (2006). "Can moisture buffer performance be estimated from sorption kinetics?" *Journal of building physics,* 29 (4), pp. 281–299 (cit. on pp. 27, 29).

[**Demirboğa *et al.* 2003**] Demirboğa, R. and Gül, R. (2003). "The effects of expanded perlite aggregate, silica fume and fly ash on the thermal conductivity of lightweight concrete". *Cement and Concrete Research,* 33 (5), pp. 723–727 (cit. on p. 121).

[**Diamond 1970**] Diamond, S. (1970). "Pore size distribution in clays". *Clays and clay minerals,* 18 (1), pp. 7–23 (cit. on p. 71).

[**Dondi *et al.* 1999**] Dondi, M., Marsigli, M., and Venturi, I. (1999). "Microstructure and mechanical properties of clay bricks: comparison between fast firing and traditional firing". *British Ceramic Transactions,* 98 (1), pp. 12–18 (cit. on p. 34).

[**Dondi *et al.* 2003**] Dondi, M., Principi, P., Raimondo, M., and Zanarini, G. (2003). "Water vapour permeability of clay bricks". *Construction and Building Materials,* 17 (4), pp. 253–258 (cit. on p. 117).

[**DURABLE 2010**] DURABLE, C. G.A. D. (2010). *Les filières industrielles stratégiques de l'économie verte* (cit. on p. 1).

[**Dutra *et al.* 2017**] Dutra, L., Mendes, N, and Philippi, P. (2017). "On the characterization of pore size distribution of building materials". *Journal of Building Physics,* (cit. on p. 191).

[**Eletrobras 2007**] Eletrobras (2007). "ELETROBRAS-Centrais Elétricas Brasileiras - Pesquisa de Posse de Equipamentos e Hábitos de Uso: ano-base 2005, classe residencial". *Relatório Brasil: ELETROBRAS/PROCEL, Rio de Janeiro,* (cit. on p. 8).

[**Eliche-Quesada *et al.* 2017**] Eliche-Quesada, D, Felipe-Sesé, M., López-Pérez, J., and Infantes-Molina, A (2017). "Characterization and evaluation of rice husk ash and wood ash in sustainable clay matrix bricks". *Ceramics International,* 43 (1), pp. 463–475 (cit. on p. 71).

[**Fick 1855**] Fick, A. (1855). "Ueber diffusion". *Annalen der Physik,* 170 (1), pp. 59–86 (cit. on p. 21).

[**Frini-Srasra *et al.* 2010**] Frini-Srasra, N and Srasra, E (2010). "Acid treatment of south Tunisian palygorskite: removal of Cd (II) from aqueous and phosphoric acid solutions". *Desalination,* 250 (1), pp. 26–34 (cit. on p. 75).

[**Frost *et al.* 2010**] Frost, R. L., Xi, Y., and He, H. (2010). "Synthesis, characterization of palygorskite supported zero-valent iron and its application for methylene blue adsorption". *Journal of colloid and interface science,* 341 (1), pp. 153–161 (cit. on p. 75).

[**Galan 1996**] Galan, E (1996). "Properties and applications of palygorskite-sepiolite clays". *Clay Minerals,* 31 (4), pp. 443–453 (cit. on pp. 36, 49).

[**Ge *et al.* 2014**] Ge, H., Yang, X., Fazio, P., and Rao, J. (2014). "Influence of moisture load profiles on moisture buffering potential and moisture residuals of three groups of hygroscopic materials". *Building and Environment,* 81, pp. 162–171 (cit. on p. 28).

[**Gencel *et al.* 2014**] Gencel, O., Coz Diaz, J. J. del, Sutcu, M., Koksal, F., Rabanal, F. A., Martinez-Barrera, G., and Brostow, W. (2014). "Properties of gypsum composites containing vermiculite and polypropylene fibers: Numerical and experimental results". *Energy and Buildings,* 70, pp. 135–144 (cit. on pp. 12, 48).

[**Giese 1988**] Giese, R. (1988). "Kaolin minerals; structures and stabilities". *Reviews in Mineralogy and Geochemistry,* 19 (1), pp. 29–66 (cit. on p. 50).

[**Goktas *et al.* 1997**] Goktas, A., Misirli, Z, and Baykara, T (1997). "Sintering behaviour of sepiolite". *Ceramics international,* 23 (4), pp. 305–311 (cit. on p. 71).

[**Gomez *et al.* 2007**] Gomez, I, Sala, J., and Millan, J. (2007). "Characterization of moisture transport properties for lightened clay brick—comparison between two manufacturers". *Journal of Building Physics,* 31 (2), pp. 179–194 (cit. on p. 117).

[**Goodhew *et al.* 2005**] Goodhew, S. and Griffiths, R. (2005). "Sustainable earth walls to meet the building regulations". *Energy and Buildings,* 37 (5), pp. 451–459 (cit. on p. 12).

[**Haden Jr 1963**] Haden Jr, W. (1963). "Attapulgite: properties and uses". *Clays Clay Miner,* 10, pp. 284–290 (cit. on p. 49).

[**Hagemann 1981**] Hagemann, E. (1981). *Byggematerialer.* Tech. rep. Polyteknisk Forlag (cit. on p. 25).

[**Hagentoft *et al.* 2004**] Hagentoft, C.-E., Kalagasidis, A. S., Adl-Zarrabi, B., Roels, S., Carmeliet, J., Hens, H., Grunewald, J., Funk, M., Becker, R., Shamir, D., *et al.* (2004). "Assessment method of numerical prediction models for combined heat, air and moisture transfer in building components: benchmarks for one-dimensional cases". *Journal of thermal envelope and building science,* 27 (4), pp. 327–352 (cit. on pp. 130, 134).

[**Hall *et al.* 2009**] Hall, M. and Allinson, D. (2009). "Analysis of the hygrothermal functional properties of stabilised rammed earth materials". *Building and Environment,* 44 (9), pp. 1935–1942 (cit. on p. 12).

[**Hall *et al.* 2012**] Hall, M., Tsang, S., Casey, S., Khan, M., and Yang, H (2012). "Synthesis, characterization and hygrothermal behaviour of mesoporous silica high-performance desiccants for relative humidity buffering in closed environments". *Acta Materialia,* 60 (1), pp. 89–101 (cit. on pp. 13, 35, 96).

[**Hansen 1986**] Hansen, K. K. (1986). "Sorption isotherms: a catalogue". PhD thesis. Technical University of DenmarkDanmarks Tekniske Universitet, Department of Structural Engineering and MaterialsInstitut for Bærende Konstruktioner og Materialer (cit. on p. 18).

[**He *et al.* 2010**] He, J. and Hoyano, A. (2010). "Experimental study of cooling effects of a passive evaporative cooling wall constructed of porous ceramics with high water soaking-up ability". *Building and environment,* 45 (2), pp. 461–472 (cit. on pp. 30, 35).

[**Herskovitch *et al.* 1996**] Herskovitch, D and Lin, I. (1996). "Upgrading of raw perlite by a dry magnetic technique". *Physical Separation in Science and Engineering,* 7 (3), pp. 145–161 (cit. on p. 44).

[**Huang *et al.* 1994**] Huang, W.-L., Bassett, W. A., and Wu, T (1994). "Dehydration and hydration of montmorillonite at elevated temperatures and pressures monitored using synchrotron radiation". *American Mineralogist,* (79), pp. 683–691 (cit. on p. 47).

[**IARC 1997**] IARC (1997). "Monographs on the Evaluation of Carcinogenic Risks to Humans". 68. Accessed: 2016-06-20. URL: `https://monographs.iarc.fr/ENG/Monographs/vol68/mono68-8.pdf` (cit. on p. 48).

[**Ibrahim *et al.* 2012**] Ibrahim, S. S. and Selim, A. Q. (2012). "Heat treatment of natural diatomite". *Physicochem. Probl. Miner. Process,* 48 (2), pp. 413–424 (cit. on pp. 52, 53).

[**INMETRO 2012**] INMETRO (2012). "Technical Regulation of Quality-RTQ for Energy Efficiency Level in Residential Buildings". *National Institute of Metrology, Quality and Technology,* Accessed: 2017-03-17. URL: `http://www.inmetro.gov.br/legislacao/rtac/pdf/RTAC001788.pdf` (cit. on p. 8).

[**ISO12572 2001**] ISO12572 (2001). "Hygrothermal performance of building materials and products- Determination of water vapour transmission properties". *International Organization for Standardization, Geneva,* (cit. on p. 109).

[**Jiang *et al.* 1999**] Jiang, L. and Guan, Y. (1999). "Pore structure and its effect on strength of high-volume fly ash paste". *Cement and Concrete Research,* 29 (4), pp. 631–633 (cit. on p. 99).

[**JIs 2002**] JIs, A (2002). "1470-1 (2002)". *Test method of adsorption/desorption efficiency for building materials to regulate an indoor humidity-Part,* 1 (cit. on p. 26).

[**Johari *et al.* 2010**] Johari, I., Said, S., Hisham, B, Bakar, A, and Ahmad, Z. (2010). "Effect of the change of firing temperature on microstructure and physical properties of clay bricks from Beruas (Malaysia)". *Science of Sintering,* 42 (2), pp. 245–254 (cit. on pp. 34, 42).

[**Jordan *et al.* 2008**] Jordan, M., Montero, M., Meseguer, S, and Sanfeliu, T (2008). "Influence of firing temperature and mineralogical composition on bending strength and porosity of ceramic tile bodies". *Applied Clay Science,* 42 (1), pp. 266–271 (cit. on p. 99).

[**Jougnot *et al.* 2010**] Jougnot, D and Revil, A (2010). "Thermal conductivity of unsaturated clay-rocks". *Hydrology and Earth System Sciences,* 14 (1), pp. 91–98 (cit. on p. 123).

[**Karagiannis *et al.* 2016**] Karagiannis, N., Karoglou, M., Bakolas, A., and Moropoulou, A. (2016). "Building Materials Capillary Rise Coefficient: Concepts, Determination and Parameters Involved". *New Approaches to Building Pathology and Durability.* Springer, pp. 27–44 (cit. on p. 118).

[**Karaman *et al.* 2006**] Karaman, S., Ersahin, S., and Gunal, H. (2006). "Firing temperature and firing time influence on mechanical and physical properties of clay bricks". *Journal of Scientific and Industrial Research,* (cit. on pp. 34, 41).

[**Kawagoe *et al.* 2014**] Kawagoe, H., Imo-oka, N., Shinohara, H., and Yamanaka, S. (2014). "Ship-in-bottle synthesis of the mixed-layered compounds of clay silicate/zirconium phosphate". *Dalton Transactions,* 43 (27), pp. 10642–10650 (cit. on p. 46).

[**Kornmann 2009**] Kornmann, M. (2009). "Matériaux de terre cuite: Propriétés et produits". *Techniques de l'ingénieur. Construction,* (C906) (cit. on p. 57).

[**Koronthalyova 2016**] Koronthalyova, O. (2016). "Water vapor sorption hysteresis of ceramic bricks". *AIP Conference Proceedings.* Vol. 1752. 1. AIP Publishing, p. 040015 (cit. on p. 114).

[**Krischer *et al.* 1963**] Krischer, O and Kast, W (1963). *Scientific Fundamentals of Drying Technology* (cit. on p. 21).

[**Kshama *et al.* 1992**] Kshama, V. D., Mohan, B., Lalithambika, M, and Nair, C. (1992). "Sintering studies on plastic clays". *Ceramics international,* 18 (6), pp. 359–364 (cit. on p. 99).

[**Kuila *et al.* 2013**] Kuila, U. and Prasad, M. (2013). "Specific surface area and pore-size distribution in clays and shales". *Geophysical Prospecting,* 61 (2), pp. 341–362 (cit. on p. 71).

[**Künzel 1995**] Künzel, H. M. (1995). "Simultaneous heat and moisture transport in building components". *One-and two-dimensional calculation using simple parameters. IRB-Verlag Stuttgart,* (cit. on p. 17).

[**Langmuir 1918**] Langmuir, I. (1918). "The adsorption of gases on plane surfaces of glass, mica and platinum." *Journal of the American Chemical society,* 40 (9), pp. 1361–1403 (cit. on p. 18).

[**Larsen 1995**] Larsen, P. K. (1995). *Moisture physical properties of bricks.* Tech. rep. Technical University of Denmark (cit. on p. 23).

[**Lee *et al.* 2008**] Lee, V.-G. and Yeh, T.-H. (2008). "Sintering effects on the development of mechanical properties of fired clay ceramics". *Materials Science and Engineering: A,* 485 (1), pp. 5–13 (cit. on p. 34).

[**Lemons 1997**] Lemons, J. (1997). "Diatomite". *American Ceramic Society Bulletin,* 76 (6), pp. 92–95 (cit. on p. 51).

[**Lenntech 2017**] Lenntech (2017). "Zeolites structure and types". Accessed: 2017-08-29. URL: `https://www.lenntech.pl/zeolites-structure-types.htm` (cit. on p. 53).

[**Li 2005**] Li, G (2005). "Microstructure and self-humidity-control performance of mineral material sepiolite". MA thesis. Tianjin: Hebei University of Technology (cit. on p. 34).

[**Li 2011**] Li, Y. (2011). "An Experimental and Numerical Study of the Influence of Room Factors and Hygroscopic Material of Wood Paneling on the Indoor Environment". PhD thesis. Concordia University (cit. on pp. 26, 31).

[**Lin 2007**] Lin, K.-L. (2007). "The effect of heating temperature of thin film transistor-liquid crystal display (TFT-LCD) optical waste glass as a partial substitute partial for clay in eco-brick". *Journal of Cleaner Production,* 15 (18), pp. 1755–1759 (cit. on p. 59).

[**Liuzzi *et al.* 2013**] Liuzzi, S, Hall, M., Stefanizzi, P, and Casey, S. (2013). "Hygrothermal behaviour and relative humidity buffering of unfired and hydrated lime-stabilised clay composites in a Mediterranean climate". *Building and Environment,* 61, pp. 82–92 (cit. on p. 12).

[**Luz *et al.* 2005**] Luz, A. and Almeida, S. (2005). "Atapulgita e sepiolita". *Rio de Janeiro: CETEM-MCT,* (cit. on p. 49).

[**Maage 1984**] Maage, M. (1984). "Frost resistance and pore size distribution in bricks". *Matériaux et Construction,* 17 (5), pp. 345–350 (cit. on p. 71).

[**Martínez *et al.* 2012**] Martínez, M., Eliche, D, Cruz, N, and Corpas, F. (2012). "Utilización de bagazo de la industria cervecera para la producción de ladrillos para construcción". *Materiales de construcción,* 62 (306), pp. 199–212 (cit. on p. 57).

[**McGregor *et al.* 2014a**] McGregor, F., Heath, A., Fodde, E., and Shea, A. (2014a). "Conditions affecting the moisture buffering measurement performed on compressed earth blocks". *Building and Environment,* 75, pp. 11–18 (cit. on pp. 27, 28).

[**McGregor *et al.* 2014b**] McGregor, F., Heath, A., Shea, A., and Lawrence, M. (2014b). "The moisture buffering capacity of unfired clay masonry". *Building and Environment,* 82, pp. 599–607 (cit. on pp. 13, 31, 133).

[**Meissner 2008**] Meissner, J. (2008). "Desenvolvimento de um aparato experimental para avaliação da inercia higroscopica de elementos porosos de edificacoes". MA thesis. Curitiba (cit. on p. 30).

[**Meissner *et al.* 2010**] Meissner, J., Mendes, N, Mendonça, K., and Moura, L. (2010). "A full-scale experimental set up for evaluating the moisture buffer effects of porous material". *International Communications in Heat and Mass Transfer,* 37 (9), pp. 1197–1202 (cit. on p. 25).

[**Mekki *et al.* 2008**] Mekki, H., Anderson, M., Benzina, M., and Ammar, E. (2008). "Valorization of olive mill wastewater by its incorporation in building bricks". *Journal of hazardous materials,* 158 (2), pp. 308–315 (cit. on p. 57).

[**Mendes 1997**] Mendes, N. (1997). "Modelos para previsão da transferência de calor e de umidade em elementos porosos de edificações". PhD thesis. Universidade Federal de Santa Catarina (cit. on pp. 108, 191).

[**Monteiro *et al.* 2004**] Monteiro, S. and Vieira, C. (2004). "Influence of firing temperature on the ceramic properties of clays from Campos dos Goytacazes, Brazil". *Applied Clay Science,* 27 (3), pp. 229–234 (cit. on p. 34).

[**Mortensen *et al.* 2005**] Mortensen, L. H., Rode, C., and Peuhkuri, R. H. (2005). "Full scale tests of moisture buffer capacity of wall materials". *7th Nordic Symposium on Building Physics,* pp. 662–669 (cit. on p. 29).

[**Mukhopadhyaya *et al.* 2002**] Mukhopadhyaya, P., Kumaran, K., Normandin, N., and Goudreau, P. (2002). "Effect of surface temperature on water absorption coefficient of building materials". *Journal of Building Physics,* 26 (2), pp. 179–195 (cit. on p. 118).

[**Munoz *et al.* 2017**] Munoz, P, Morales, M., Letelier, V, and Mendivil, M. (2017). "Fired clay bricks made by adding wastes: assessment of the impact on physical, mechanical and thermal properties" (cit. on p. 33).

[**Murray 1988**] Murray, H. H. (1988). "Kaolin minerals; their genesis and occurrences". *Reviews in Mineralogy and Geochemistry,* 19 (1), pp. 67–89 (cit. on p. 50).

[**NBR15220 2005**] NBR15220 (2005). "Desempenho térmico de edificações, parte 3: zoneamento bioclimático brasileiro e diretrizes construtivas para habitações unifamiliares de interesse social". *Associação Brasileira de Normas Técnicas, Rio de Janeiro,* (cit. on p. 8).

[**NBR15575 2013**] NBR15575 (2013). "Edificações habitacionais - Desempenho Térmico". *Associação Brasileira de Normas Técnicas, Rio de Janeiro,* (cit. on p. 8).

[**Ngun *et al.* 2011**] Ngun, B. K., Mohamad, H., Sulaiman, S. K., Okada, K., and Ahmad, Z. A. (2011). "Some ceramic properties of clays from central Cambodia". *Applied Clay Science,* 53 (1), pp. 33–41 (cit. on p. 34).

[**Nigay *et al.* 2017**] Nigay, P., Cutard, T, and Nzihou, A (2017). "The impact of heat treatment on the microstructure of a clay ceramic and its thermal and mechanical properties". *Ceramics International,* 43 (2), pp. 1747–1754 (cit. on pp. 34, 36).

[**Novais *et al.* 2015**] Novais, R. M., Seabra, M., and Labrincha, J. (2015). "Lightweight dense/porous bi-layered ceramic tiles prepared by double pressing". *Journal of Materials Processing Technology,* 216, pp. 169–177 (cit. on pp. 34, 99).

[**O'Farrell *et al.* 2001**] O'Farrell, M, Wild, S, and Sabir, B. (2001). "Pore size distribution and compressive strength of waste clay brick mortar". *Cement and Concrete Composites,* 23 (1), pp. 81–91 (cit. on p. 71).

[**Okada *et al.* 2008**] Okada, K., Matsui, S., Isobe, T., Kameshima, Y., and Nakajima, A. (2008). "Water-retention properties of porous ceramics prepared from mixtures of allophane and vermiculite for materials to counteract heat island effects". *Ceramics international,* 34 (2), pp. 345–350 (cit. on pp. 12, 48).

[**Oladunjoye *et al.* 2012**] Oladunjoye, M. A. and Sanuade, O. A. (2012). "Thermal Diffusivity, Thermal Effusivity and Specific Heat of Soils in Olorunsogo Powerplant, Southwestern Nigeria". *International Journal of Research and Reviews in Applied Sciences,* 13 (2), pp. 502–521 (cit. on p. 122).

[**Osanyintola *et al.* 2006**] Osanyintola, O. F. and Simonson, C. J. (2006). "Moisture buffering capacity of hygroscopic building materials: experimental facilities and energy impact". *Energy and Buildings,* 38 (10), pp. 1270–1282 (cit. on p. 26).

[**Oumeziane *et al.* 2014**] Oumeziane, Y. A., Bart, M., Moissette, S., and Lanos, C. (2014). "Hysteretic behaviour and moisture buffering of hemp concrete". *Transport in porous media,* 103 (3), pp. 515–533 (cit. on p. 32).

[**Padfield 1998**] Padfield, T. (1998). "The role of absorbent building materials in moderating changes of relative humidity". PhD thesis. Technical University of Denmark, p. 165 (cit. on pp. 12, 25, 45).

[**Padfield *et al.* 2011**] Padfield, T. and Jensen, L. A. (2011). "Humidity buffering by absorbent materials". *Proceedings of the Nordic Symposium on Building Physics, Tampere, Finland.* Vol. 29, pp. 475–482 (cit. on p. 31).

[**Pérez-Villarejo *et al.* 2012**] Pérez-Villarejo, L, Eliche-Quesada, D, Iglesias-Godino, F. J., Martínez-García, C, and Corpas-Iglesias, F. A. (2012). "Recycling of ash from biomass incinerator in clay matrix to produce ceramic bricks". *Journal of Environmental Management,* 95, S349–S354 (cit. on p. 63).

[**Peuhkuri *et al.* 2004**] Peuhkuri, R. H., Rode, C., and Hansen, K. K. (2004). "Moisture buffer capacity of different insulation materials". *Thermal Performance of Exterior Envelopes of Whole Buildings Ix,* (cit. on pp. 26, 29).

[**Pichór *et al.* 2009**] Pichór, W. and Janiec, A. (2009). "Thermal stability of expanded perlite modified by mullite". *Ceramics International,* 35 (1), pp. 527–530 (cit. on pp. 45, 92).

[**Pinto 1996**] Pinto, L. C. M. (1996). "Quantikov: um analisador microestrutural para o ambiente Windows". PhD thesis. IPEN-USP: São Paulo, p. 167 (cit. on pp. 72, 73, 85).

[**Pires *et al.* 2011**] Pires, L, Silva, P. D., and Gomes, J. C. (2011). "Performance of textile and building materials for a particular evaporative cooling purpose". *Experimental Thermal and Fluid Science,* 35 (4), pp. 670–675 (cit. on pp. 13, 31).

[**Plathner *et al.* 2002**] Plathner, P. and Woloszyn, M. (2002). "Interzonal air and moisture transport in a test house: experiment and modelling". *Building and Environment,* 37 (2), pp. 189–199 (cit. on pp. 11, 12).

[**PROCEL 2017**] PROCEL (2017). "Plano Nacional de Eficiência Energética. Premissas e diretrizes básicas." *Ministério de Minas e Energia,* Accessed: 2017-07-19. URL: `http://www.mme.gov.br/documents/10584/1432134/Plano+Nacional+EficiÃłncia+EnergÃ©tica+(PDF)/74cc9843-cda5-4427-b623-b8d094ebf863?version=1.1` (cit. on p. 8).

[**Rahaman 2007**] Rahaman, M. N. (2007). *Sintering of ceramics.* CRC press (cit. on p. 42).

[**Rahim *et al.* 2015**] Rahim, M, Douzane, O, Le, A. T., Promis, G, Laidoudi, B, Crigny, A, Dupre, B, and Langlet, T (2015). "Characterization of flax lime and hemp lime concretes: Hygric properties and moisture buffer capacity". *Energy and Buildings,* 88, pp. 91–99 (cit. on pp. 27, 32).

[**Rahim *et al.* 2016**] Rahim, M, Le, A. T., Douzane, O, Promis, G, and Langlet, T (2016). "Numerical investigation of the effect of non-isotherme sorption characteristics on hygrothermal behavior of two bio-based building walls". *Journal of Building Engineering,* 7, pp. 263–272 (cit. on pp. 11, 12).

[**Rahim 2015**] Rahim, M. (2015). "Analyse et caractérisation du comportement hygrothermique de parois agro-sourcées à l'échelle 1 : expérimentation et modélisation". PhD thesis. Université de Picardie Jules Verne, p. 214 (cit. on pp. 128, 136).

[**Raimondo *et al.* 2007**] Raimondo, M, Dondi, M, Mazzanti, F, Stefanizzi, P, and Bondi, P (2007). "Equilibrium moisture content of clay bricks: The influence of the porous structure". *Building and Environment,* 42 (2), pp. 926–932 (cit. on p. 13).

[**Raimondo *et al.* 2009**] Raimondo, M., Dondi, M., Gardini, D., Guarini, G., and Mazzanti, F. (2009). "Predicting the initial rate of water absorption in clay bricks". *Construction and Building Materials,* 23 (7), pp. 2623–2630 (cit. on pp. 118, 119).

[**Ransom 2002**] Ransom, W. H. (2002). *Building failures: Diagnosis and avoidance.* Routledge (cit. on p. 10).

[**Rao *et al.* 2012**] Rao, Z., Wang, S., and Zhang, Z. (2012). "Energy saving latent heat storage and environmental friendly humidity-controlled materials for indoor climate". *Renewable and Sustainable Energy Reviews,* 16 (5), pp. 3136–3145 (cit. on pp. 2, 34).

[**Rashad 2016**] Rashad, A. M. (2016). "Vermiculite as a construction material–A short guide for Civil Engineer". *Construction and Building Materials,* 125, pp. 53–62 (cit. on p. 48).

[**Rathossi *et al.* 2010**] Rathossi, C and Pontikes, Y. (2010). "Effect of firing temperature and atmosphere on ceramics made of NW Peloponnese clay sediments. Part I: Reaction paths, crystalline phases, microstructure and colour". *Journal of the European Ceramic Society,* 30 (9), pp. 1841–1851 (cit. on p. 34).

[**Reznik 1971**] Reznik, A. (1971). *Permeability and Porosity Predictions from a Cutting-and-rejoining Model and Pore-size Distribution.* University of Pittsburgh (cit. on p. 191).

[**Riccardi *et al.* 1999**] Riccardi, M. P., Messiga, B., and Duminuco, P (1999). "An approach to the dynamics of clay firing". *Applied Clay Science,* 15 (3), pp. 393–409 (cit. on p. 34).

[**Rode 2005**] Rode, C. (2005). *Moisture Buffering of Building Materials.* Tech. rep. Lyngby: Technical University of Denmark, p. 78 (cit. on pp. 2, 26–28, 30, 127, 133).

[**Rodts 2001**] Rodts, S. (2001). "Étude du passage micro-macro pour le transport par diffusion en milieu poreux. Application aux expériences de RMN-GCP". PhD thesis. École des Ponts ParisTech (cit. on p. 71).

[**Roels *et al.* 2006**] Roels, S. and Janssen, H. (2006). "A comparison of the Nordtest and Japanese test methods for the moisture buffering performance of building materials". *Journal of Building Physics,* 30 (2), pp. 137–161 (cit. on p. 27).

[**Rouquerol *et al.* 1994**] Rouquerol, J, Avnir, D, Fairbridge, C., Everett, D., Haynes, J., Pernicone, N, Ramsay, J., Sing, K., and Unger, K. (1994). "Recommendations for the characterization of porous solids (Technical Report)". *Pure and Applied Chemistry,* 66 (8), pp. 1739–1758 (cit. on p. 16).

[**Rudy *et al.* 2017**] Rudy, B., Matthieu, L., and Jean-Emmanuel, A. (2017). "Comparison of the Saturated Salt Solution and the Dynamic Vapor Sorption techniques based on the measured sorption isotherm of barley straw". *Construction and Building Materials,* 141, pp. 140–151 (cit. on p. 114).

[**Ruiz *et al.* 1996**] Ruiz, R, Del Moral, J., Pesquera, C, Benito, I, and González, F (1996). "Reversible folding in sepiolite: study by thermal and textural analysis". *Thermochimica Acta,* 279, pp. 103–110 (cit. on p. 75).

[**Saiah *et al.* 2010**] Saiah, R, Perrin, B, and Rigal, L (2010). "Improvement of thermal properties of fired clays by introduction of vegetable matter". *Journal of Building Physics,* 34, pp. 124–142 (cit. on p. 63).

[**Salonvaara *et al.* 2004**] Salonvaara, M., Ojanen, T., Holm, A., Künzel, H. M., and Karagiozis, A. N. (2004). "Moisture buffering effects on indoor air quality-experimental and simulation results". *Proceedings of Buildings IX, Clearwater, Florida.* Citeseer (cit. on p. 8).

[**Samar *et al.* 2016**] Samar, M. and Saxena, S. (2016). "Study of chemical and physical properties of perlite and its application in India". *International Journal of Science Technology and Management,* 5 (4), pp. 70–80 (cit. on pp. 44, 45).

[**Serna *et al.* 1977**] Serna, C, VanScoyoc, G., and Ahlrichs, J. (1977). "Hydroxyl groups and water in palygorskitel". *Am. Miner,* 62, pp. 784–792 (cit. on p. 75).

[**Serra *et al.* 2015**] Serra, M., Conconi, M., Suarez, G, Aglietti, E., and Rendtorff, N. (2015). "Volcanic ash as flux in clay based triaxial ceramic materials, effect of the

firing temperature in phases and mechanical properties". *Ceramics International,* 41 (5), pp. 6169–6177 (cit. on p. 34).

[**Shang *et al.* 2017**] Shang, J.-l., Zong, Z.-f., and Zhang, H. (2017). "Synthesis and analysis of new humidity-controlling composite materials". *International Journal of Minerals, Metallurgy, and Materials,* 24 (5), pp. 594–602 (cit. on p. 35).

[**Shea *et al.* 2012**] Shea, A., Lawrence, M., and Walker, P. (2012). "Hygrothermal performance of an experimental hemp–lime building". *Construction and Building Materials,* 36, pp. 270–275 (cit. on pp. 12, 31).

[**Simonson *et al.* 2002**] Simonson, C., Salonvaara, M, and Ojanen, T (2002). "The effect of structures on indoor humidity–possibility to improve comfort and perceived air quality". *Indoor Air,* 12 (4), pp. 243–251 (cit. on pp. 11, 12).

[**Singh *et al.* 1991**] Singh, M. and Garg, M. (1991). "Perlite-based building materials—a review of current applications". *Construction and Building Materials,* 5 (2), pp. 75–81 (cit. on p. 45).

[**Sutcu 2015**] Sutcu, M. (2015). "Influence of expanded vermiculite on physical properties and thermal conductivity of clay bricks". *Ceramics International,* 41 (2), pp. 2819–2827 (cit. on pp. 64, 121).

[**Svennberg 2006**] Svennberg, K. (2006). *Moisture buffering in the indoor environment.* Vol. 1016. Byggnadsfysik LTH, Lunds Tekniska Högskola (cit. on pp. 13, 26).

[**Svennberg *et al.* 2004**] Svennberg, K., Hedegaard, L. G., and Rode, C. (2004). "Moisture buffer performance of a fully furnished room". *Performance of the Exterior Envelopes of Whole Buildings Ix,* (cit. on p. 29).

[**Taoukil *et al.* 2013**] Taoukil, D., Sick, F., Mimet, A., Ezbakhe, H., Ajzoul, T., *et al.* (2013). "Moisture content influence on the thermal conductivity and diffusivity of wood–concrete composite". *Construction and Building Materials,* 48, pp. 104–115 (cit. on p. 13).

[**Thommes *et al.* 2015**] Thommes, M., Kaneko, K., Neimark, A. V., Olivier, J. P., Rodriguez-Reinoso, F., Rouquerol, J., and Sing, K. S. (2015). "Physisorption of gases, with special reference to the evaluation of surface area and pore size distribution (IUPAC Technical Report)". *Pure and Applied Chemistry,* (cit. on p. 20).

[**Togkalidou *et al.* 2013**] Togkalidou, T., Karoglou, M., Bakolas, A., Giakoumaki, A., and Moropoulou, A. (2013). "Correlation of water vapor permeability with microstructure characteristics of building materials using robust chemometrics". *Transport in porous media,* 99 (2), pp. 273–295 (cit. on p. 117).

[**Topçu *et al.* 2007**] Topçu, I. B. and Işıkdağ, B. (2007). "Manufacture of high heat conductivity resistant clay bricks containing perlite". *Building and Environment,* 42 (10), pp. 3540–3546 (cit. on p. 45).

[**Tosoh 2017**] Tosoh (2017). "Zeolites for Molecular Sieves". Accessed: 2017-08-29. URL: `http://www.tosoh.com/our-products/advanced-materials/zeolites-for-molecular-sieves` (cit. on p. 53).

[**Trindade *et al.* 2009**] Trindade, M., Dias, M., Coroado, J, and Rocha, F (2009). "Mineralogical transformations of calcareous rich clays with firing: a comparative study between calcite and dolomite rich clays from Algarve, Portugal". *Applied Clay Science,* 42 (3), pp. 345–355 (cit. on p. 34).

[**Tveit 1966**] Tveit, A. (1966). *Measurements of moisture sorption and moisture permeability of porous materials.* Norwegian Building Research Inst. (cit. on pp. 22, 117).

[**Umurigirwa *et al.* 2014**] Umurigirwa, B. S., Maalouf, C., Halouani, A., and Mai, T. H. (2014). "Etude numérique et expérimentale du comportement hygrothermique d'un agro-composite à base de fibres de chanvre et d'amidon de blé." *IBPSA,* (cit. on pp. 27, 32).

[**Valette 2015**] Valette, S. (2015). "Techniques de caractérisation des céramiques". *Techniques de l'ingénieur,* 33 (0) (cit. on p. 72).

[**Van Genuchten 1980**] Van Genuchten, M. T. (1980). "A closed-form equation for predicting the hydraulic conductivity of unsaturated soils". *Soil science society of America journal,* 44 (5), pp. 892–898 (cit. on p. 191).

[**VanScoyoc *et al.* 1979**] VanScoyoc, G., Serna, C., and Ahlrichs, J. (1979). "Structural changes in palygorskite during dehydration and dehydroxylation". *American Mineralogist,* 64 (1-2), pp. 215–223 (cit. on p. 75).

[**Vardoulakis *et al.* 2011a**] Vardoulakis, E, Karamanis, D, Assimakopoulos, M. N., Boemi, S. N., and Mihalakakou, G (2011a). "Moisture Sorption Properties of Modified Porous Clays for Roof Evaporative Cooling Applications". *International Journal of Ventilation,* 10 (2), pp. 185–194 (cit. on p. 14).

[**Vardoulakis *et al.* 2011b**] Vardoulakis, E, Karamanis, D, Assimakopoulos, M. N., and Mihalakakou, G (2011b). "Solar cooling with aluminium pillared clays". *Solar Energy Materials and Solar Cells,* 95 (8), pp. 2363–2370 (cit. on pp. 14, 15).

[**Velasco *et al.* 2014**] Velasco, P. M., Ortíz, M. M., Giró, M. M., and Velasco, L. M. (2014). "Fired clay bricks manufactured by adding wastes as sustainable construction material–A review". *Construction and Building materials,* 63, pp. 97–107 (cit. on p. 33).

[**Vereecken *et al.* 2011**] Vereecken, E., Roels, S., and Janssen, H. (2011). "In situ determination of the moisture buffer potential of room enclosures". *Journal of building physics,* 34 (3), pp. 223–246 (cit. on p. 129).

[**Vieira *et al.* 2008**] Vieira, C., Sanchez, R, and Monteiro, S. (2008). "Characteristics of clays and properties of building ceramics in the state of Rio de Janeiro, Brazil". *Construction and Building Materials,* 22 (5), pp. 781–787 (cit. on p. 13).

[**Vu *et al.* 2013**] Vu, D.-H., Wang, K.-S., Bac, B. H., and Nam, B. X. (2013). "Humidity control materials prepared from diatomite and volcanic ash". *Construction and Building Materials,* 38, pp. 1066–1072 (cit. on pp. 13, 35).

[**Wanphen *et al.* 2009**] Wanphen, S. and Nagano, K. (2009). "Experimental study of the performance of porous materials to moderate the roof surface temperature by its

evaporative cooling effect". *Building and Environment,* 44, pp. 338–351 (cit. on pp. 14, 15).

[**Weng *et al.* 2003**] Weng, C.-H., Lin, D.-F., and Chiang, P.-C. (2003). "Utilization of sludge as brick materials". *Advances in environmental research,* 7 (3), pp. 679–685 (cit. on pp. 57, 59).

[**White 1987**] White, R. E. *et al.* (1987). *Introduction to the principles and practice of soil science.* Second Edition. Blackwell Scientific Publications (cit. on p. 46).

[**Wienerberger 2017**] Wienerberger (2017). "House constructed of clay building materials". Accessed: 2017-03-25. URL: `http://clay-wienerberger.com` (cit. on p. 14).

[**Woloszyn *et al.* 2008**] Woloszyn, M. and Rode, C. (2008). "Tools for performance simulation of heat, air and moisture conditions of whole buildings". *Building Simulation.* Vol. 1. 1. Springer, pp. 5–24 (cit. on pp. 128, 129).

[**Wu *et al.* 2014**] Wu, Y., Gong, G., Yu, C. W., and Fang, P. (2014). "The hygroscopic properties of wood fibre, sepiolite and expanded perlite-based breathable wall for moderating the humidity environment". *Indoor and Built Environment,* 23 (2), pp. 299–312 (cit. on pp. 35, 45).

[**Yakub *et al.* 2012**] Yakub, I, Du, J, and Soboyejo, W. (2012). "Mechanical properties, modeling and design of porous clay ceramics". *Materials Science and Engineering: A,* 558, pp. 21–29 (cit. on p. 99).

[**Yang *et al.* 2014**] Yang, X., Ge, H., Fazio, P., and Rao, J. (2014). "Evaluation of parameters influencing the moisture buffering potential of hygroscopic materials with BSim Simulations". *Buildings,* 4 (3), pp. 375–393 (cit. on pp. 27, 32).

[**Yanniotis *et al.* 2009**] Yanniotis, S. and Blahovec, J. (2009). "Model analysis of sorption isotherms". *LWT-Food Science and Technology,* 42 (10), pp. 1688–1695 (cit. on p. 18).

[**Yilmazer *et al.* 2005**] Yilmazer, S. and Ozdeniz, M. B. (2005). "The effect of moisture content on sound absorption of expanded perlite plates". *Building and Environment,* 40 (3), pp. 311–318 (cit. on p. 45).

[**Yuan *et al.* 2004**] Yuan, P., Wu, D., He, H., and Lin, Z. (2004). "The hydroxyl species and acid sites on diatomite surface: a combined IR and Raman study". *Applied Surface Science,* 227 (1), pp. 30–39 (cit. on p. 52).

[**Zhang *et al.* 2012**] Zhang, H., Yoshino, H., and Hasegawa, K. (2012). "Assessing the moisture buffering performance of hygroscopic material by using experimental method". *Building and Environment,* 48, pp. 27–34 (cit. on pp. 11, 27, 28, 31).

[**Zhang *et al.* 2017a**] Zhang, H., Yoshino, H., Hasegawa, K., Liu, J., Zhang, W., and Xuan, H. (2017a). "Practical Moisture Buffering Effect of Three Hygroscopic Materials in Real-World Conditions." *Energy and Buildings,* (cit. on p. 27).

[**Zhang *et al.* 2017b**] Zhang, M., Qin, M., Rode, C., and Chen, Z. (2017b). "Moisture Buffering Phenomenon and its Impact on Building Energy Consumption". *Applied Thermal Engineering,* (cit. on pp. 26, 27).

Appendices

Appendix A

EDS map of elements

The scanning electron microscope (Vega3, Tescan) from Materials Technology and Manufacturing Processes Laboratory at PUCPR is equipped with an energy dispersive X-ray spectroscope (EDS). This equipment allows elemental identification of materials and provides a map of elements in the sample. Table A.1 summarizes the characteristics of the EDS setup and Figs. A.1, A.2, A.7, A.8, A.9 and A.10 show the elemental map of samples. Gold (Au) should be excluded from analyses since it does not make part of the original composition of the material. Gold was identified because samples were gold coated.

Table A.1: EDS operation system characteristics.

Label	Spectrum 3
Source	Acquired
Accelerating voltage	10kV
Working distance	15 mm
Elevation degrees	35
Number of channels	1024
Energy range	10 keV
Energy per channel	10 eV
Detector type	X-act
Window type	SATW
Primary dectector	EDS1

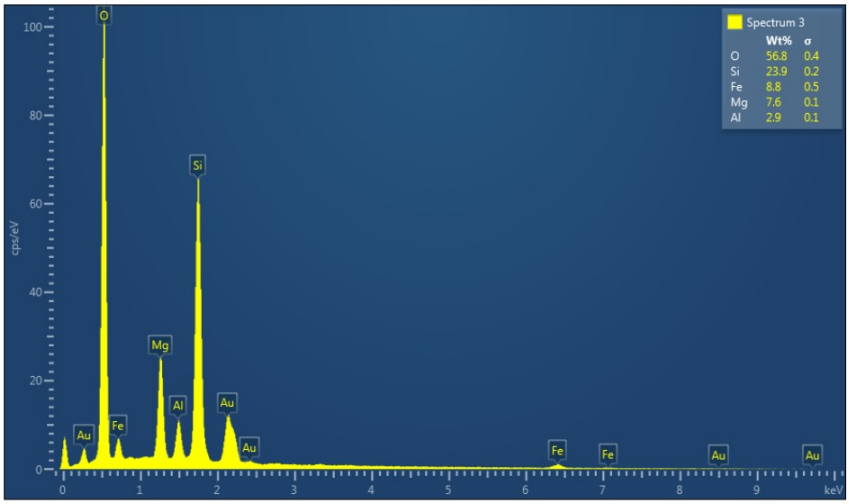

Figure A.1: EDS pattern for raw attapulgite.

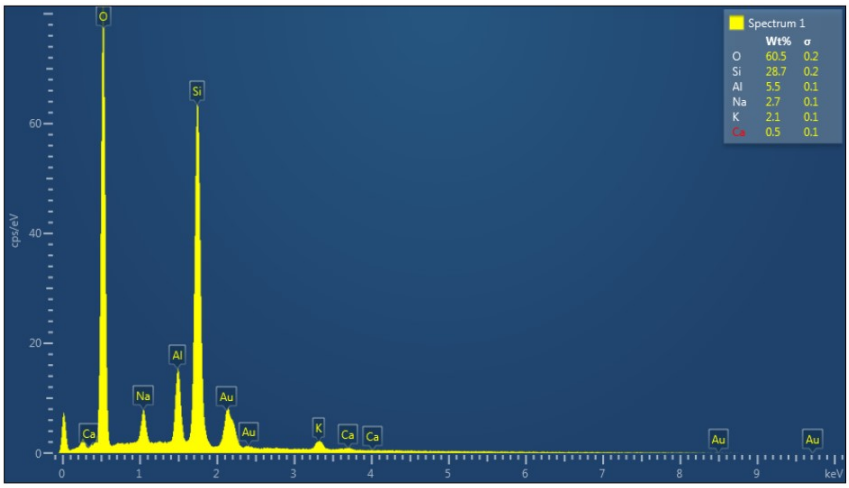

Figure A.2: EDS pattern for raw perlite

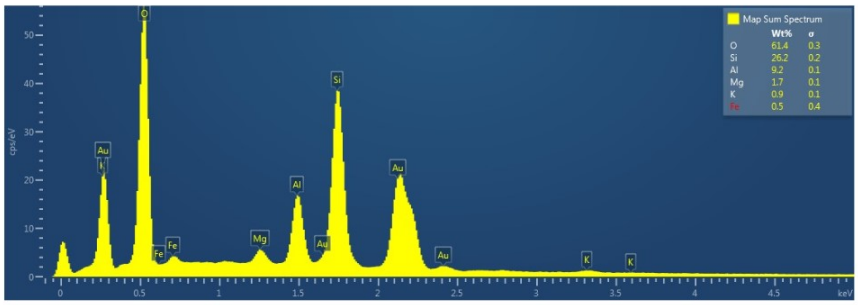

Figure A.3: EDS pattern for CATT800

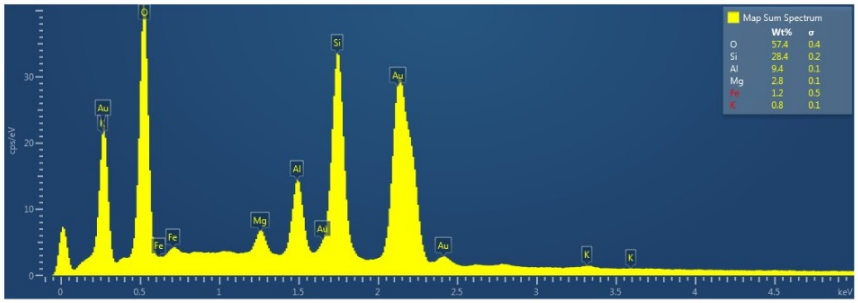

Figure A.4: EDS pattern for CATT1000

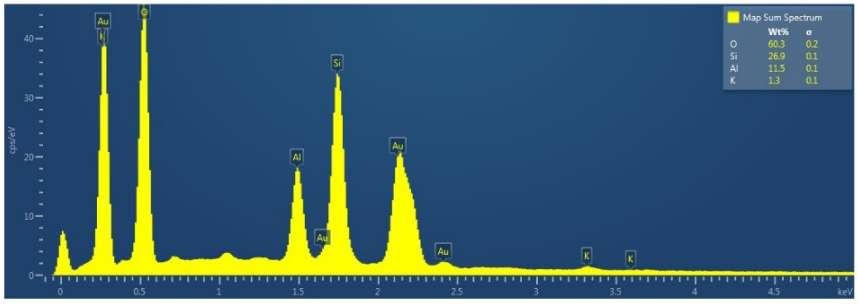

Figure A.5: EDS pattern for CPER800

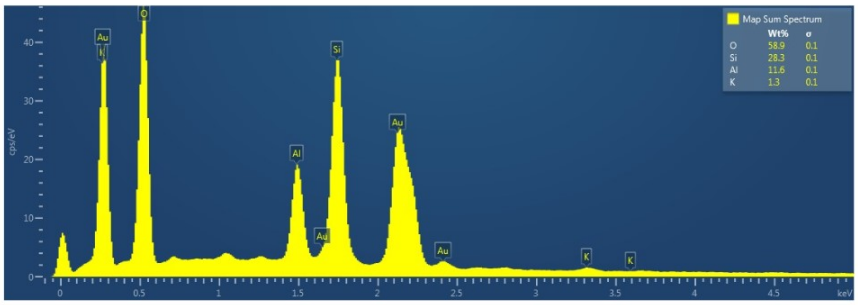

Figure A.6: EDS pattern for CPER1000

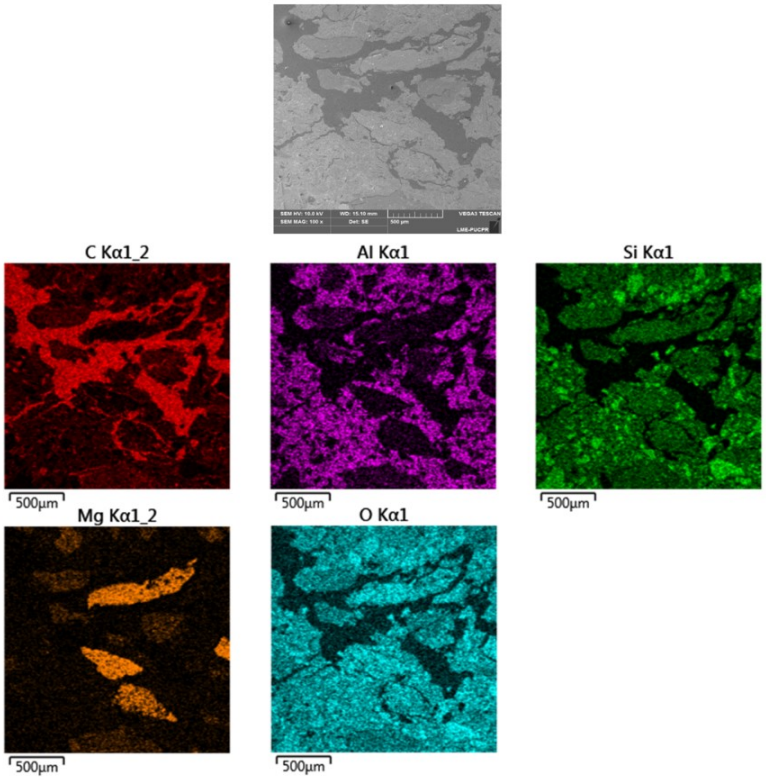

Figure A.7: EDS map of elements for CATT sintered at 800°C.

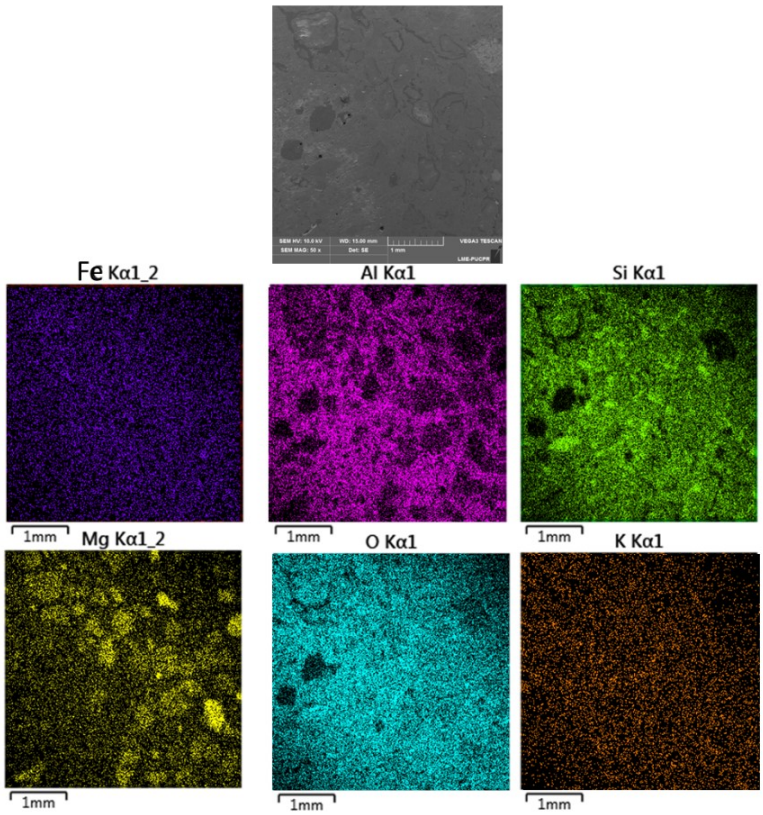

Figure A.8: EDS map of elements for CATT sintered at 1000°C.

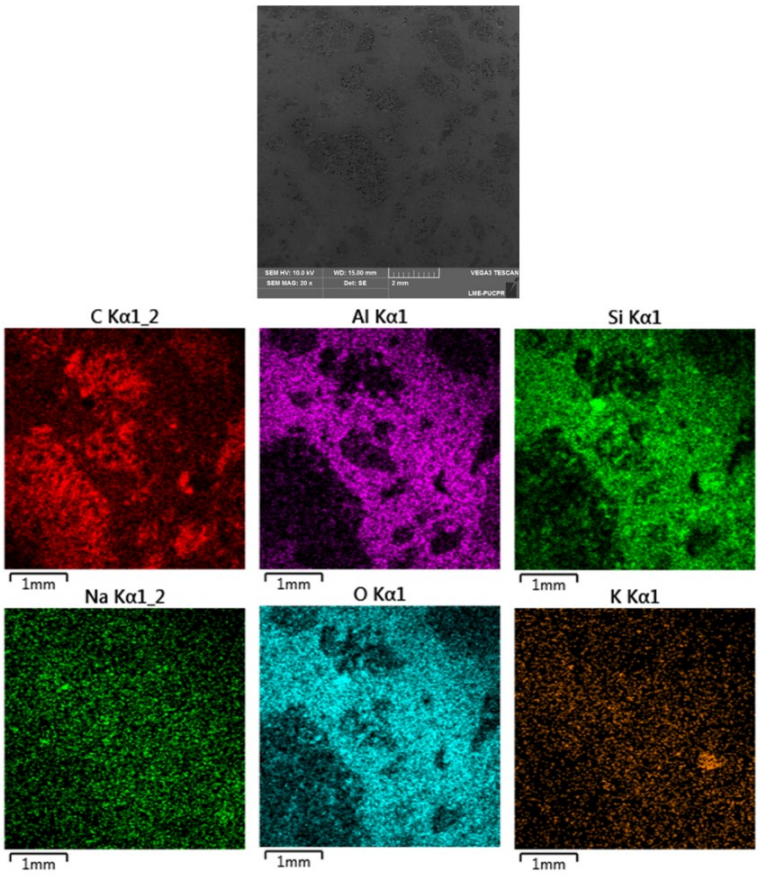

Figure A.9: EDS map of elements for CPER sintered at 800°C.

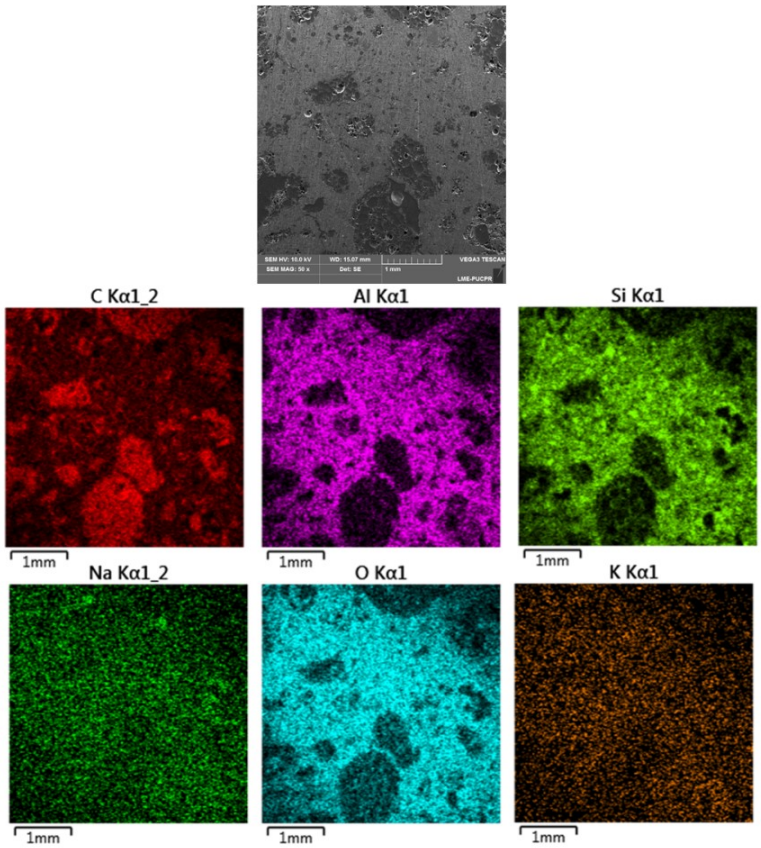

Figure A.10: EDS map of elements for CPER sintered at 1000°C.

Appendix B

Nitrogen adsorption data and BET calculations

Sorption isotherms measurements (Fig.B.1) made by the NOVA 2000e, Quantachrome (Ecomateriales Laboratory at UANL) provide data to BET calculations. P and P_o are the equilibrium and saturation pressure respectively of nitrogen at the temperature of 77.3K. The volume of adsorbed nitrogen by the solid material surface, in cm^3/g, is represented by V_{ads} and the monolayer adsorbed gas quantity by M. Considering the relative pressure and its relation with W and M expressed by Eq.43, is possible to plot a graph with $1/\mathrm{M}[(p_o/\mathrm{p})\text{-}1]$ and RH=p/p_o (Fig.B.2). The slope (A) and the y-intercept (B) are useful to calculate the M value (Eq.45) and the constant k (Eq.44). Values obtained by linear regression are summarized in Tab.B.1. Finally, the specific surface area (S_o) is determined by Eq.46.

$$\frac{1}{V_{ads}[(p/p_o)]-1} = \frac{k-1}{Mk}\left(\frac{p}{p_o}\right) + \frac{1}{Mk} \tag{43}$$

where:

$$k = 1 + \frac{A}{B} \tag{44}$$

and

$$M = \frac{1}{A+B} \tag{45}$$

$$S_o = \frac{MNC_s}{V_m m} \tag{46}$$

where: N is the Avogadro's constant, C_s is the cross section of the adsorbing species, V_m is the molar volume of the gas and m is the mass of the solid.

Table B.1: Parameters obtained by linear regression for all composition.

Sample	S	B	Standard error (S)	Standard error (B)	R^2
CLAY800	189.1464	2.93759	1.12602	0.21578	0.99982
CLAY1000	480.00887	16.1624	7.65299	1.48504	0.99873
CATT800	116.29867	1.62957	0.51792	0.09982	0.9999
CATT1000	284.76991	6.92191	2.8837	0.55295	0.99949
CPER800	179.57022	3.57685	1.85409	0.36189	0.99947
CPER1000	365.44975	11.41166	7.71191	1.5006	0.99778

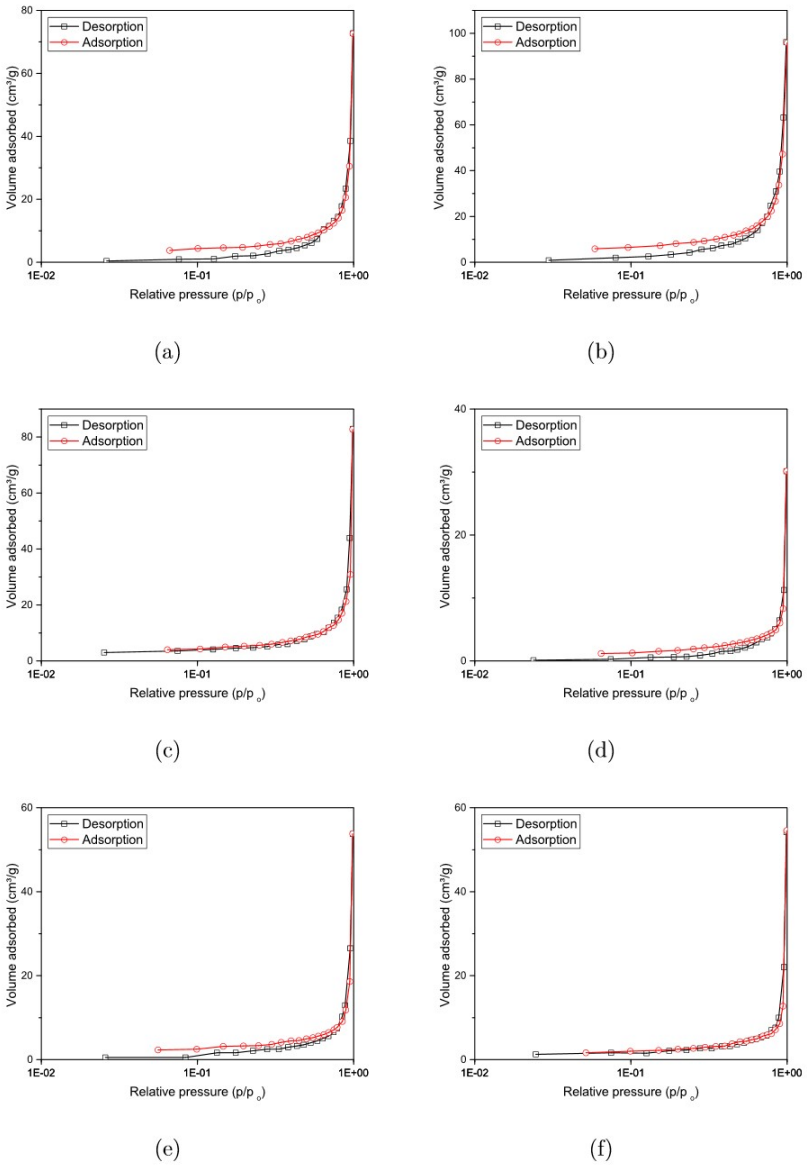

Figure B.1: Nitrogen sorption isotherms for samples sintered at 800°C:(a) fired clay (b) clay with attapulgite and (c) clay with perlite. For samples sintered at 1000°C: (d) fired clay, (e) clay with attapulgite and (f) clay with perlite.

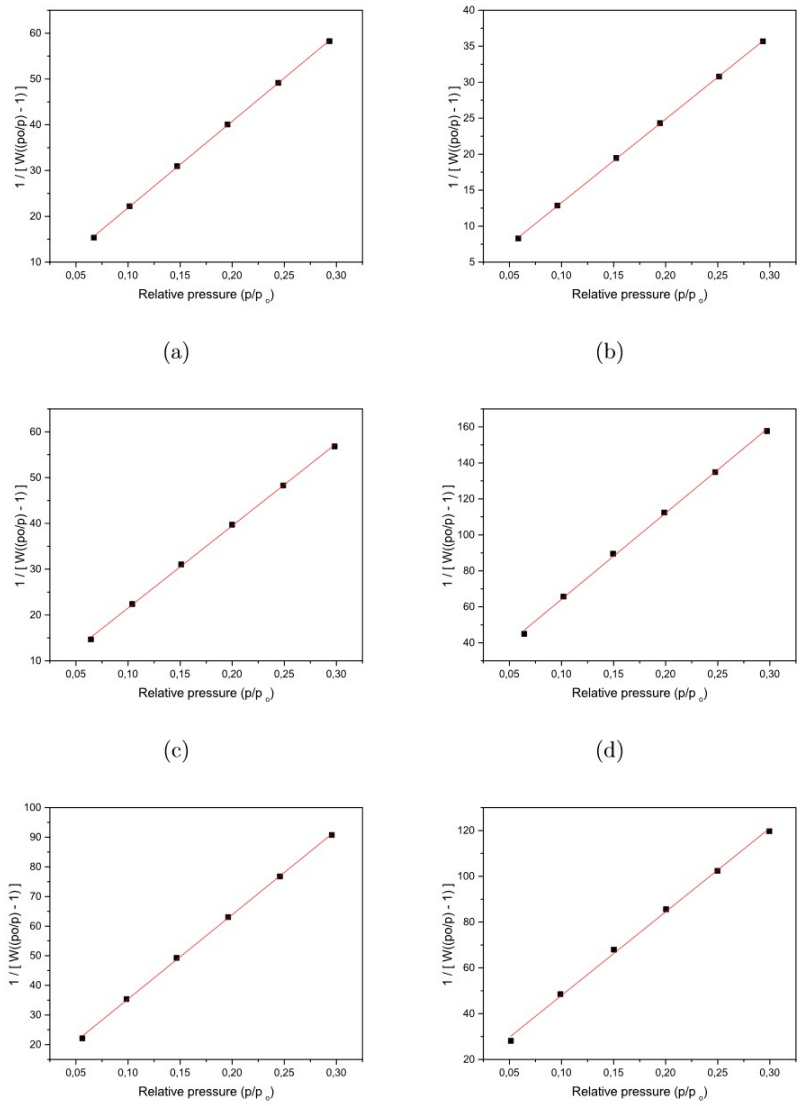

Figure B.2: Linear regression aiming to obtain the parameters S and B. This linear correlation is only valid in the range of $0.05 < p/p_o < 0.35$. Samples sintered at 800°C are: (a) fired clay (b) clay with attapulgite and (c) clay with perlite. Samples sintered at 1000°C: (d) fired clay, (e) clay with attapulgite and (f) clay with perlite.

Appendix C

Water adsorption isotherm data and GAB calculations

Table C.1 shows the GAB constants obtained by Eq. 9. Nomenclature 'ads' corresponds to the curve of adsorption and 'des' to desorption curve.

Table C.1: Parameters obtained by GAB adjustment.

Coefficients	α	β	γ	R^2
CMMT800 ads	-0.010	0.247	72.459	0.99947
CMMT800 des	-0.009	0.652	25.863	0.99968
CMMT1000 ads	-0.016	0.245	136.470	0.99916
CMMT1000 des	-0.011	0.265	87.612	0.99862
CATT800 ads	-0.011	0.761	38.047	0.99989
CATT800 des	0.003	-1.143	94.112	0.99548
CATT1000 ads	-0.027	-0.007	262.550	0.99975
CATT1000 des	-0.020	0.345	164.307	0.99972
CDIA800 ads	-0.012	0.256	94.936	0.99746
CDIA800 des	-0.010	0.848	23.464	0.99597
CDIA1000 ads	-0.032	0.359	285.536	0.99676
CDIA1000 des	-0.017	0.278	149.711	0.99469
CSGR800 ads	-0.01298	0.33513	96.11614	0.99435
CSGR800 des	-0.00845	0.67022	20.96866	0.99997

Table C.1: Parameters obtained by GAB adjustment.

Coefficients	α	β	γ	R^2
CSGR1000 ads	0.06348	-12.16728	591.05085	0.96868
CSGR1000 des	0.04811	-9.2351	451.36395	0.9659
CSSA800 ads	-0.01283	0.697	58.511	0.998
CSSA800 des	-0.011	1.005	9.514	0.99794
CSSA1000 ads	-0.022	0.828	129.576	0.99688
CSSA1000 des	-0.015	0.632	88.107	0.99488
CVER800 ads	-0.021	2.107	0.297	0.98365
CVER800 des	-0.011	0.909	23.142	0.99733
CVER1000 ads	-0.012	0.245	98.723	0.96401
CVER1000 des	-0.011	0.272	92.610	0.96275
CPER800 ads	-0.03507	-0.96964	434.79524	0.99558
CPER800 des	-0.02257	2.16031	13.51624	0.99885
CPER1000 ads	-0.02752	0.0053	265.09303	0.99888
CPER1000 des	-0.02295	0.02738	219.98716	0.99847
CLAY800 ads	-0.01677	1.46156	26.26536	0.99896
CLAY800 des	-0.01187	1.14671	10.74762	0.99118
CLAY1000 ads	-0.01419	0.25534	119.29634	0.97805
CLAY1000 des	-0.01222	0.40656	86.01024	0.96726
CSUF800 ads	-0.01088	0.15665	96.197	0.99949
CSUF800 des	-8.37E-04	-0.59035	74.15993	0.99897
CSUF1000 ads	-0.01228	0.2985	95.07167	0.97708
CSUF1000 des	-0.00963	0.2156	78.15885	0.9722
CZEO800 ads	-0.02458	2.32133	14.94039	0.99532
CZEO800 des	-0.01258	1.04383	25.89342	0.99477
CZEO1000 ads	-0.01861	0.32017	152.74885	0.98484
CZEO1000 des	-0.01382	0.2396	115.50472	0.97831

Appendix D

Water absorption coefficient correlations

Table D.1 regroups some microstructural characteristics of clay-based materials studied in this work. The water absorption coefficient, initial rate of absorption and total amount of water absorbed were calculated based on partial immersion test (section 4.3.4). Open porosity was obtained by gravity test (section 2.5). Specific surface area and pore mean size were given by nitrogen adsorption technique (Appendix B).

Some correlations between water absorption coefficient and the microstructural characteristics were performed (Fig. D.1). The statistical agreement (R^2) is calculated for each graph. It can be seen that initial rate of absorption and total amount of water absorbed presented the highest statistical correlation with 0.78593 and 0.50991 respectively. On the other hand, pore mean diameter, specific surface area and open porosity have a poor statistical correlation with 0.0597, 0.1217 and 0.0059 respectively.

Table D.1: Water absorption coefficients ($A_c[Kg/m^2s^{0.5}]$), initial rate of absorption (IR $[Kg/m^2.2min]$), the total amount of water absorbed (AW $[Kg/m^2]$), specific surface area (S_o $[m^2/g]$), open porosity (OP [%]) and pore mean diameter (PM [nm]) for samples sintered at T = 800°C and at 1000°C.

	T	A_c	**IR**	**AW**	S_o	**OP**	**PM**
CLAY	800	0.050	0.619	2.602	18.3	32.81	5.46
CATT	800	0.061	0.876	2.767	29.53	42.96	2.36
CVER	800	0.070	1.498	3.645	-	45.78	-
CDIA	800	0.078	1.048	3.297	-	46.91	-
CPER	800	0.092	1.463	3.217	19.1	34.40	3.66
CZEO	800	0.094	1.642	2.695	-	34.96	-
CSUF	800	0.112	1.804	3.283	-	39.61	-
CSGR	800	0.132	2.762	3.685	-	42.66	-
CMMT	800	0.150	1.722	3.919	-	43.25	-
CS_o	800	0.276	3.815	5.017	-	41.47	-
CLAY	1000	0.051	0.591	2.478	7.02	28.04	1.84
CATT	1000	0.087	1.609	3.612	11.94	37.78	1.61
CVER	1000	0.087	2.255	4.419	-	45.94	-
CDIA	1000	0.088	1.322	3.558	-	42.96	-
CPER	1000	0.161	1.828	3.416	9.24	34.47	2.42
CZEO	1000	0.077	1.857	2.729	-	26.16	-
CSUF	1000	0.119	1.875	3.328	-	35.99	-
CSGR	1000	0.183	2.386	3.552	-	37.79	-
CMMT	1000	0.175	2.192	4.001	-	38.96	-
CS_o	1000	0.378	3.977	4.534	-	37.32	-

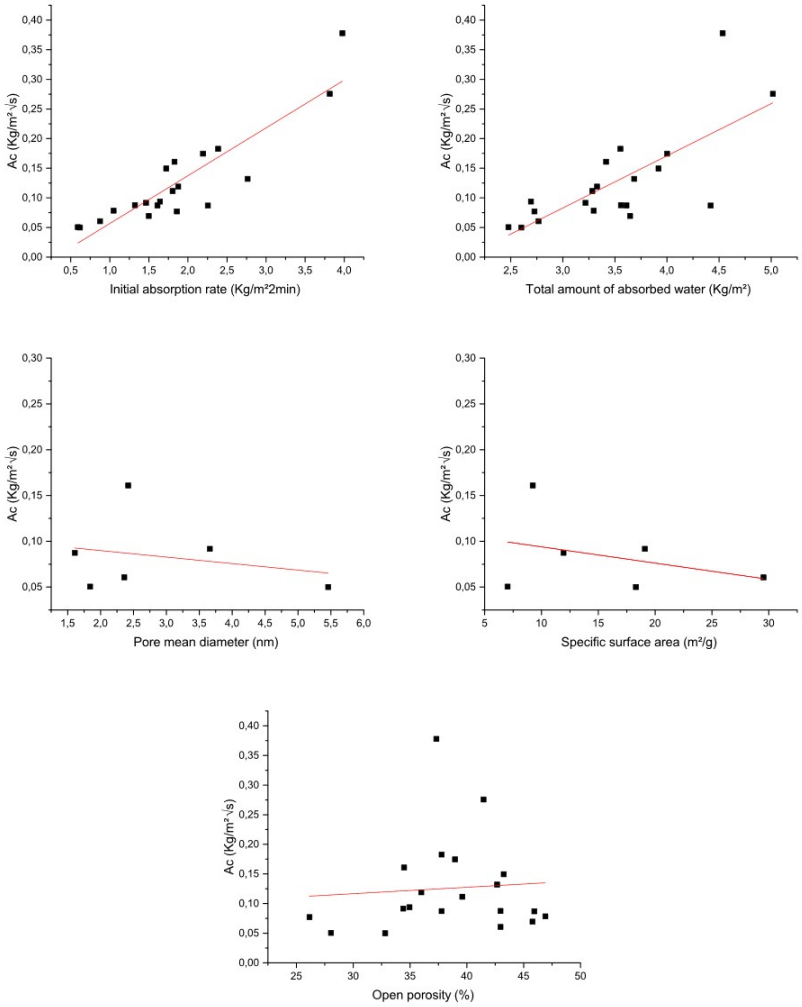

Figure D.1: Statistical correlations for all samples: sintered at 800°C and 1000°C.

Appendix E

Modelling water sorption curves

The experimental results can be used to obtain other important information about microstructure of materials and as an input data to hygrothermal simulation softwares. This obtainment can be achieved by using the following models and theories. The coefficients A, B, C, a_1, m_1, a_2, m_2, can complement characterization by enabling calculation of moisture transport coefficients and more complex simulations taking into account moisture accumulation and transport in the funicular regime.

A, B, C, a_1, m_1, a_2, m_2, are obtained by fitting graphs Van Genuchten [Van Genuchten 1980] and Reznik [Reznik 1971] models.

The complete obtainment procedure is described in Dutra *et al.* [2017] and Mendes [1997].

Reznik adjustments (Eqs. 47 and 48) to obtain a_1, a_2, m_1 and m_2 were performed from fitting the graph of pore radius en function of saturation of non wetting phase (S_{nw}).

$$r \begin{cases} = a_1 exp(m_1 * S_{nw}); S_b < S_{nw} < 1 & (47) \\ = a_2 exp(m_2 * S_{nw}); 0 < S_{nw} < S_b & (48) \end{cases}$$

S_b is the intersection of curves 47 and 48;

$$S_{nw} = \frac{I * \rho_s}{\eta} \quad (49)$$

where:

η is the porosity [-];

I is Hg cumulative intrusion [mL/g].

ρ_s is the density of the material [kg/m^3].

Van Genuchten adjustment is made fitting the graph of capillary pressure en function of saturation. A, B, C coefficients are obtained according Eq. 50:

$$\Psi_{H_2O} = exp\left\{\frac{1}{A}\left[s^{\frac{1}{C}} - 1\right]^{\frac{1}{B}}\right\} \tag{50}$$

where:

$$\Psi_{H_2O} = p_c \frac{\sigma_{H_2O}\ cos\theta_{H_2O}}{\sigma_{Hg}\ cos\theta_{Hg}} \tag{51}$$

$$s = \frac{\theta}{\eta} \tag{52}$$

Figures E.1 and E.2 illustrate all graphs used for coefficients obtainment. Coefficients A, B, C provided by Van Genuchten adjustment and a_1, a_2, m_1 and m_2 from Reznik model are given in tab. E.1.

Table E.1: Calculated coefficients using GAB, Van Genuchten and Reznik models for samples sintered at 800°C.

Coefficients	CLAY	CATT	CPER
A	0.065	0.037	0.217
B	30.556	12.992	17.954
C	-2.352	-364.122	-23377.536
α	-44.417	-55.049	-75.181
β	29.890	23.177	-64.663
γ	17.575	34.696	142.302
m_1	-8.525	-3.860	-4.284
m_2	-1.643	-38.251	-18.526
a_1	2.730E-05	2.58E-07	9.07E-07
a_2	8.820E-08	6.09E-04	1.43E-04

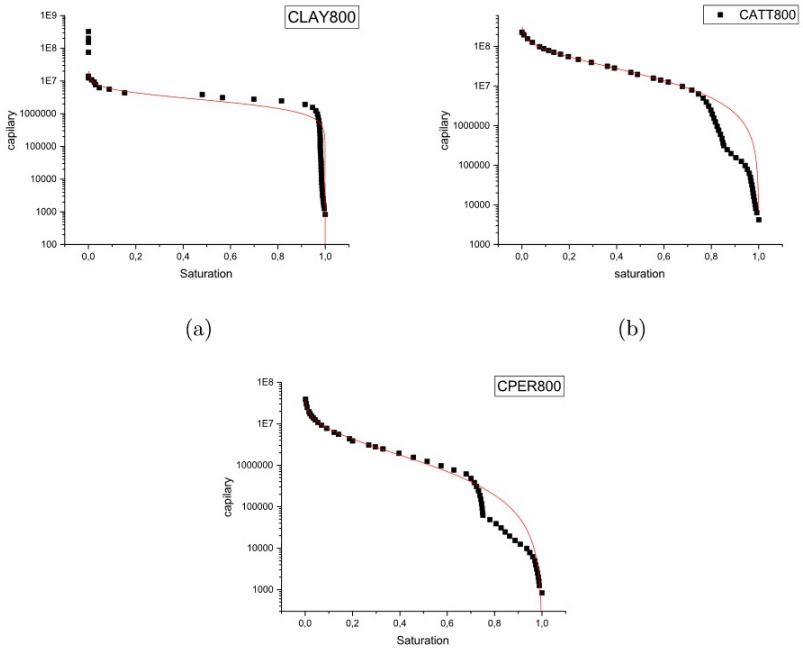

(a)

(b)

(c)

Figure E.1: Coefficients adjustment using the Van Genuchten model.

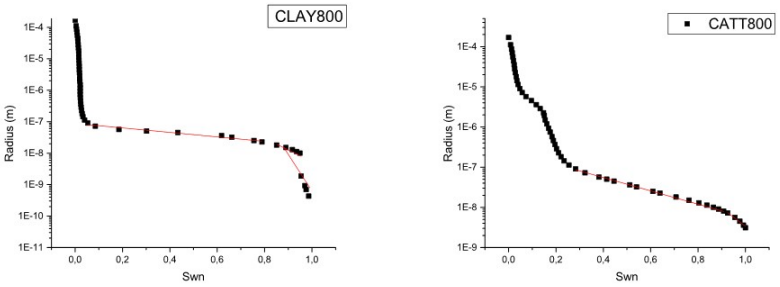

(a)

(b)

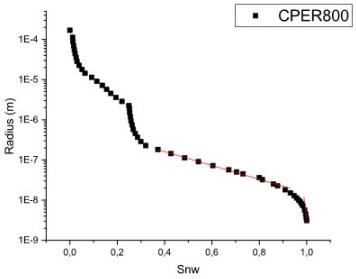

(c)

Figure E.2: Coefficients adjustment using the Reznik model.